CONSTITUTIVE MODELING AND DYNAMIC IMPACT ANALYSIS OF BIGHORN SHEEP HORN

by

Zheng Li

A dissertation submitted to the faculty of
The University of North Carolina at Charlotte
in partial fulfillment of the requirements
for the degree of Doctor of Philosophy in
Mechanical Engineering

Charlotte

2022

Approved by:

_____
Dr. Howie Fang

_____
Dr. Alireza Tabarraei

_____
Dr. David Weggel

_____
Dr. Nigel Zheng

_____
Dr. Matthew Whelan

ABSTRACT

ZHENG LI. Constitutive Modeling and Dynamic Impact Analysis of Bighorn Sheep Horn. (Under the direction of DR. HOWIE FANG)

Bighorn sheep (*Ovis canadensis*) is known for its giant spiral horns that can sustain impact loading at a speed up to 5.5 m/s during ramming without causing severe damage or head concussion. The bighorn sheep horn is composed of a keratin-based biological material with a tubule-lamella structure. This special structure produces the anisotropic hardening characteristics of the horn material under impact loading. Investigating the mechanisms of energy dissipation of bighorn sheep horn can inspire the design and development of artificial materials with high capacity of energy dissipation and/or impact mitigation.

In this study, a transversely isotropic constitutive model with anisotropic hardening and strain-rate effects was developed for predicting the mechanical responses of the horn under impact loading. The characterization of material properties was conducted using test data from uniaxial compression tests of the horns under both quasi-static and dynamic loadings. The constitutive model was later implemented into the commercial finite element code, LS-Dyna, as user-defined material subroutine and was successfully validated against test results. Finite element simulations were conducted on the dynamic impact against the bighorn sheep horn, and the user-defined constitutive model was used to study the

mechanical responses of the horn material subjected to large impact loads without causing severe damage. The mechanism of energy dissipation was also investigated from energy absorption and conversion, stress distributions, and propagation of displacement waves.

ACKNOWLEDGEMENTS

I am grateful for my advisor Dr. Howie Fang for his support and guidance in my research work. He gave me extensive advice and help along the whole journey of my doctoral study, and trained me with critical thinking to help me acquire good habits to conduct research. He also guided me on learning how to become a good person with humble personalities.

I would like to show my gratitude for all my committee members, Dr. Alireza Tabarraei, Dr. David Weggel, Dr. Naiquan Zheng, Dr. Matthew Whelan, for their valuable advice and comments to my research topic. I would also thank Lukasz Pachocki from Gdańsk University of Technology in Poland for providing help generously on LS-Dyna subroutine compiling in Linux.

I would like to thank my parents for providing endless emotional support during my doctoral study. They gave me strong encouragement for the challenges I meet in my doctoral study and personal life during global pandemic. I also want to thank the person who provides love and companion over the course of my dissertation research.

TABLE OF CONTENTS

LIST OF TABLES

LIST OF FIGURES

LIST OF SYMBOLS

$E^{(q)}$	Young's modulus under quasi-static loading
$E^{(d)}$	Young's modulus under dynamic loading
K	Bulk modulus
ν	Poisson's ratio
$Y^{0(q)}$	Initial yield strength under quasi-static loading
$Y^{0(d)}$	Initial yield strength under dynamic loading
$\boldsymbol{C}$	Stiffness matrix
$\boldsymbol{S}$	Compliance matrix
$\boldsymbol{A}$	Anisotropic factor matrix
$\boldsymbol{B}$	The inverse of anisotropic factor matrix
$\boldsymbol{H}$	Hardening factor matrix
$h^{(q)}$	Hardening function under quasi-static loading
$h^{(d)}$	Hardening function under dynamic loading
f	Conventional yield function
$\hat{f}$	Modified yield function
$\boldsymbol{\sigma}$	Cauchy stress
$\hat{\boldsymbol{\sigma}}$	Modified stress tensor
$\bar{\sigma}$	Conventional effective stress
$\hat{\sigma}$	Modified effective stress
$\boldsymbol{\varepsilon}_e$	Elastic strain

$\boldsymbol{\varepsilon_p}$	Conventional plastic strain
$\hat{\boldsymbol{\varepsilon}}_{\boldsymbol{p}}$	Modified plastic strain
$\dot{\boldsymbol{\varepsilon}}_{\boldsymbol{p}}$	Conventional plastic strain rate
$\dot{\hat{\boldsymbol{\varepsilon}}}_{\boldsymbol{p}}$	Modified plastic strain rate
$\overline{\varepsilon}_p$	Conventional effective plastic strain
$\widehat{\varepsilon}_p$	Modified effective plastic strain
$\dot{\overline{\varepsilon}}_p$	Conventional effective plastic strain rate
$\dot{\widehat{\varepsilon}}_p$	Modified effective plastic strain rate
φ_r	Scaling factor in the radial direction
φ_l	Scaling factor in the longitudinal direction

CHAPTER 1: INTRODUCTION

Energy absorbent biological materials have recently raised much research interest due to their outstanding performance in impact resistance and energy absorption and dissipation. Many natural materials have been shown to be highly efficient in energy absorption and impact wave mitigation. There is a need to study and understand the fundamental mechanism of energy absorbent biological materials under dynamic impact so as to provide ideas and guidance to novel bioinspired material designs and applications.

Common energy absorbent materials can be categorized into two major groups: one based on mineralized biological composites and the other non-mineralized biological composites. Mineralized biological materials such as mollusk shells, cortical bones, and teeth, usually have a high value of stiffness but low toughness, to provide support and mastication (McKittrick et al., 2010). Cortical bones are the strongest skeleton bone of mammals with a Young's modulus of 7 - 21 GPa. A hierarchical structure is found in the composition of the cortical bone, with a basic unit called osteon that is composed of blood vessels surrounded by stacked concentric lamellae with altering orientated collagen fiber and dispersed with calcium phosphate. Mineralized calcium phosphates account for 33 - 43% of the total volume of the cortical bones, leading to their high overall stiffness and capability of supporting functions.

In contrast to the high stiffness of mineralized biological materials, non-mineralized phase materials, such as horns and hooves, tend to have a lower stiffness but higher toughness (Wegst et al., 2004). This feature allows them to exhibit higher resistance

to dynamic impacts with the capability of absorbing impact energy without significant failure. Most non-mineralized biological materials are based on protein, such as keratin. Within keratin-based biological materials, the horns of bighorn sheep have been shown to have outstanding impact resistance and energy absorption.

The horns of a male bighorn sheep (*Ovis canadensis*) are reportedly capable of withstanding an impact force up to 3,400 N at a speed of 5.5 m/s during ramming. This impact force is almost four times the weight of the sheep, but does not cause catastrophic damage to the horns or severe brain concussion (Johnson et al., 2017). Figure 1.1 shows two male bighorn sheep ramming against each other.

Figure 1.1: Two male bighorn sheep ramming (North American Nature).

Extensive research has been conducted on bighorn sheep horns and it has been observed that the key factors of their high impact resistance during ramming are the hierarchical structure, macro-structure, and material compositions. The bighorn sheep horn is composed of trabecular bone surrounded by keratin sheath. A type of protein with right-

handed helicoidal structure called α-keratin is found in the horn sheath (Tombolato et al., 2010). The basic unit of the sheath is the keratin fiber that is composed of three threads of α-keratin protofibril intertwined together. The keratin fiber is called intermediate filament (IF) and has an average diameter of 12 nm. These IFs are embedded in an amorphous keratin matrix called keratinized cell lamellae, which are stacked together by cell boundary made of proteinaceous substance. A hollow tube called tubule is extended along the growing direction of horn wrapped by stacked multi-layered lamellae, forming a tubule-lamella structure. The tubule pointed by the yellow arrow in Figure 1.2(b) is not fully aligned with the lamella; there is an approximate 30° angle between the stacked lamella and the tubule direction. It is also noticed that the tubules had increased porosity from the inner center (virtually 0%) to the exterior edge (ranges from 8-12%) on the horn's cross-section. Figure 1.3 shows the hierarchical structure of a bighorn sheep's horn sheath from macro-level to nano-level.

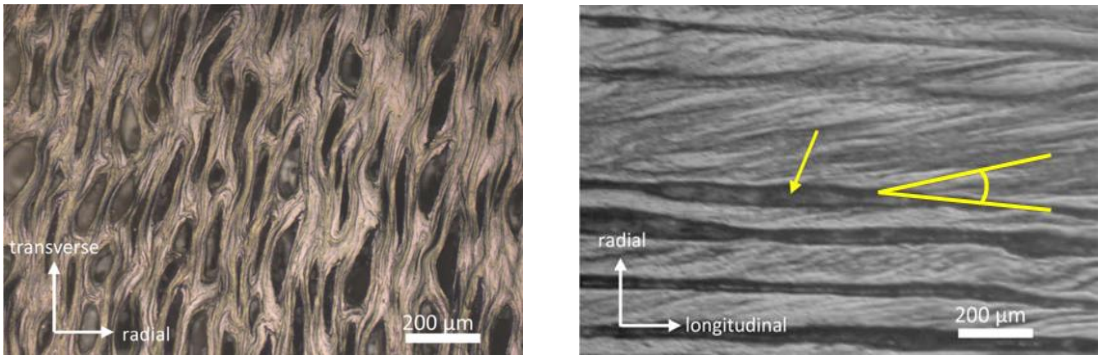

(a) (b)

Figure 1.2: Microstructure of tubule-lamellae for the cross section of (a) longitudinal view; and (b) transverse view (Tombolato et al., 2010).

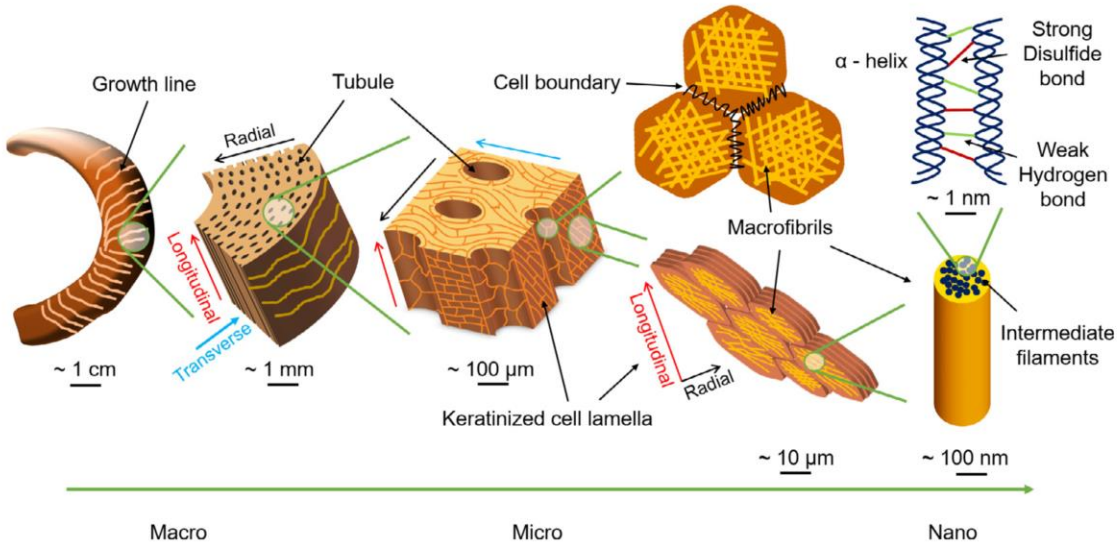

Figure 1.3: The hierarchical structure of a bighorn sheep's horn from macro-level to nano-level (Huang et al. 2019).

These compositional and structural features indicate that the horn sheath has a special tubular laminated composite structure with anisotropic material properties.

1.1 Mechanical Testing of Horns

Since 2010, mechanical testing has been conducted on horn sheath to characterize the material properties and study the stress-strain behaviors under various loading conditions.

Tombolato et al. conducted quasi-static three-point bending and compressive tests, in both longitudinal and transverse directions, on horn samples at two moisture levels: air-dried at ambient temperature and fully rehydrated (Tombolato et al. 2010). The air-dried samples had a 10.6±0.6% moisture content while the rehydrated horn samples had a

34.5±2.1% moisture content. It was shown that the maximum bending strength and elastic modulus were similar in both directions on fully rehydrated samples. For air-dried samples, the test results clearly showed the anisotropic material properties in terms of elastic moduli and bending strengths in the longitudinal and transverse directions. The researchers found extensive collapses of the tubules in the samples used in the radial-direction compression tests, indicating a source of energy absorption by collapsing of those tubules.

In 2011, Trim et al. studied the mechanical properties of horns of the bighorn sheep based on the effect of water content level and microstructures (Trim et al. 2011). The stress-strain responses were obtained by a series of compressive and tensile tests performed with a constant strain rate of 3.0×10^{-3}/s using dog-bone shaped samples cut from different locations from proximal to distal ends. It was shown that the density, tensile response and compressive response, did not vary significantly along the length of the horn, indicating a more homogenized distribution. However, the test results clearly showed the anisotropy of the keratin horn material between the longitudinal and radial directions. The longitudinal direction of the horn was found to be stiffer, stronger, and more ductile than the transverse direction, as indicated by higher Young's modulus, yield strength, and failure elongation ratio in the longitudinal direction. It was also observed that failures in the tension and compression tests were primarily triggered by matrix separation, tubule fracture, and shear. Investigation of the effect of water contents showed that the horn material transitioned from anisotropic to isotropic with increased hydration level, called "matrix-dominated" phase for samples with high hydration levels.

Zhu et al. investigated the mechanical properties of the horns of Small Tailed Han Sheep (*Ovis aries*), inspired by its promising applications to vehicle bumper designs (Zhu

et al. 2016). They conducted compressive and tensile tests to study the strength of horns in different directions and at different locations. In both compression and tension test, they found that the horn material yielded quickly after undergoing a small linear elastic deformation, and entered a plateau plastic region of material densification followed by dramatically increased material strength before ultimate failure. Anisotropic behaviors were observed on the horn sheath, with test data showing different impact resistances in the longitudinal and transverse directions under the same impact loading. The largest Young's modulus was found at the center part of the horn along the growing direction, which was the area mainly used for ram fighting to absorb impact energy.

Huang et al. studied the deformation mechanisms of the horns of bighorn sheep under compressive loading (Huang et al. 2017). The transmission electron microscopy imaging was used to observe the hierarchical structure of the horn, which was shown to have an in-plane arrangement of microfibrils for laminated structures. This finding suggested that the horn sheath material should be considered transversely isotropic in which the material properties along radial and transverse directions were similar, but they were different from those in the longitudinal direction. Huang et al. also conducted comprehensive compressive tests using $4\times4\times4$ mm^3 samples that were loaded in radial, transverse, and longitudinal directions under quasi-static loading and dynamic loading with strain rates ranging from 10^{-3}/s to 10^{3}/s. In these tests, two types of samples were considered based on water contents, one was air-dried with approximately 10% water content and the other wet with approximately 30% water content. Strain-rate effect was found under high-speed dynamic impact loading, and the authors suggested that it could be due to insufficient time for the keratin-based structure to adapt into the configurations

found in lower energy mode. At low level strain rates from 10^{-3}/s to 1/s, the strain-rate effect was not significant. The experiment results also showed significant differences in the material properties of the horn sheath in the three loading directions, confirming the anisotropic properties of the horn with higher toughness and strength in the radial and transverse directions than those in the longitudinal direction. Hopkinson bar impact recovery tests were also conducted to investigate damage modes. Tubule collapse in the radial direction, lamella buckling in the longitudinal direction, and microcracking and coalescence were found during dynamic impacts. The study showed that the radial direction provided the largest impact resistance with the highest energy absorption and compressive strength at both hydration levels. Water-assisted recoverability of keratin under high strain rate was found in this study from wet samples, which provided ideas for recoverable energy-absorbent designs.

In the study of Johnson et al., the compressive and tensile tests were performed on horn sheaths of the bighorn sheep with an average strain rate of 10^{3}/s in both longitudinal and radial directions (Johnson et al. 2017). At the high strain-rate level, the flow stresses in both directions were found to be increased, which led to an increased capability of energy absorption. It was observed that more substantial strain-rate dependency occurred in the longitudinal direction than in the radial direction. Johnson et al. also found that the horn sheath behaved more brittle at lower moisture level (10%) than at higher moisture level (35%). The increased moisture level would significantly reduce the compressive strength, improve ductility, and decrease the anisotropic effect. The hydration level of horn sheath in nature is approximately 20% during ramming, which achieves a proper balance between

the strength and ductility. It was also found that the hydration level could induce asymmetry on yield stresses between compression and tension.

Zhang et al. compared the mechanical properties of the horns from bighorn sheep with other keratin-based horns such as those from domestic sheep (*Ovis aries*), mountain goat (*Oreamnos americanus*), and pronghorn (*Antilocapra americana*) (Zhang et al. 2018). They found that the horn properties were adapted in nature to fit the species' fighting behaviors. From the drop tower impact tests, the failure strength of the horns from bighorn sheep, which was defined when 50% of the samples failed by puncture damage on the bottom surface, was measured as 75 kJ/m^2. That was 36% higher than the impact strength of domestic sheep (55 kJ/m^2), which had a lower ramming speed than the bighorn sheep during fighting. The study of the horn's microstructure showed that its outstanding impact resistance was due to the large amount of energy absorption of the internal tubular structure under plastic deformation. The horns from bighorn sheep were found to have higher tubular density and thus higher capacity of energy absorption than those from the domestic sheep. From compression and tensile tests, they found that the highest Young's modulus and yield strength were in the longitudinal direction of dried horns of the bighorn sheep and the highest toughness was in the radial direction. The radial direction was considered as the ideal direction for the horn to withstand high-speed impact loading.

Previous studies showed that increased hydration level of the horn would decrease the anisotropic effect and increase the ductility of horn keratin. Furthermore, the hydration level was also found to be critical to the recoverability of horn tissues after severe impact loading. Huang et al. investigated the water-assisted recovery mechanism in the horns of bighorn sheep (Huang et al. 2019) and found that the water content affected the keratin

structure and tensile and creep properties to achieve recovery. In their study, the amorphous keratin matrix was diffused into water modules that interacted with intermediate filaments for breaking and reforming hydrogen bonds, leading to the recovery of horn keratin even after 50% of compressive strain. It should be noted that only the mechanical properties in the radial direction could be fully recovered by hydration due to the high damage resistance in this direction. Samples with the lowest hydration level were shown to have the highest strength; however, the failure tended to be very brittle with a low tensile strain at fracture. In fully hydrated samples, the failures appeared to be ductile as indicated by fiber pull-out due to the plasticized matrix from full hydration. The protein molecules inside the horn were more active and thus have higher mobility with higher water content than those with lower water content. This high mobility of the protein molecules led to higher creep strains and higher values of compliance of the horn material than those with low mobility, as validated by the nanoindentation test.

1.2 Finite Element Modeling of Horns

Most of the studies in literature on the impact resistance mechanism of horns are based on physical experiments. Numerical investigations, such as using the finite element (FE) methods, were rarely conducted to study the impact responses of bighorn sheep horns. Only a limited number of studies can be found in literature related to FE modeling and simulations of bighorn sheep horns.

Maity et al. conducted FE analysis on the horn sheath of bighorn sheep attached to the internal bone core and under quasi-static loading conditions (Maity et al. 2011). The

horn geometry was obtained from computed tomography (CT) scan images and a three-dimensional FE model of single horn sheath was created using tetrahedral solid elements. The horn sheath component was combined with compact bone, trabecular bone, and frontal sinus, respectively for a total of three different configurations. The keratin and bone used in the study of Maity et al. were assumed to be isotropic linear elastic materials. The keratin had a Young's modulus of 2 GPa and a Poisson's ratio of 0.3. A loading force with peak value of 3.4 kN was assigned to the horn that was considered to be equivalent to that from a 100-kg bighorn sheep when ramming at a speed of 5.5 m/s. The complex horn model was rotated by 43° so that the horn was impacted with the same clashing angle as that happened in real ramming. Due to limited experimental data of loads on the internal bone of the bighorn sheep, Maity et al. conducted a sensitivity analysis using varying Young's modulus of the bone ranging from 0.8 to 20 GPa. It was shown that the strain energy of the horn was increased with the decrease of Young's modulus of the bone. This indicated that a high modulus was critical for the bone to dissipate impact energy by elastic deformation. The study generated preliminary results on the sensitivity of internal bones to Young's modulus, but did not consider the anisotropic property of horn materials and the strain-rate effects from dynamic impacts.

In 2014, Johnson et al. investigated stress wave propagation considering geometry effects, inspired by the bighorn sheep horn (Johnson et al. 2014). Four different bars, a cylindrical bar, a tapered bar, a spiral bar, and a tapered spiral bar, were studied under impulse loading initiated at the same location. The first stress invariant (associated with hydraulic pressure) and the second stress invariant (associated with shearing) were evaluated in the four bars. It was observed that the tapered bar had higher hydraulic stresses,

uniaxial stresses, and shear stresses than the cylindrical bar due to its converging geometry. For the two spiral bars, a significant transverse displacement was observed, caused by the shear waves and reflection of longitudinal stress waves. The tapered spiral bar had larger shear stresses and transverse displacements than the non-tapered spiral bar. It was concluded that a tapered spiral geometry such as that of the bighorn sheep horn would induce large shear stresses and transverse displacements, resulting in reduced normal impulses and pressures. It should be noted that the study only focused on the effect of geometry on wave mitigation during impacts and did not use the material properties of a real horn in the FE model.

In the work of Drake et al. (2016), a dynamic FE analysis on energy absorption and wave mitigation of the bighorn sheep horn was performed. They used CT scan technology to obtain the geometries of the exterior horn sheath and the interior cancellous bone. The horn material was assumed isotropic linear elastic, and a simplified point mass was attached to the horn complex through a spring element to represent the body mass of the bighorn sheep. An initial velocity of 4.7 m/s was assigned to the horn complex that impacted a rigid plate. A vibration analysis was also conducted on the horn both experimentally and numerically to study its natural frequency as well as to validate the FE model. The principal stresses were evaluated after the impact, and it was found that the lateral oscillation at the distal end (i.e., horn tip) was incited by a torque generated from the distal stress wave. For a pair of horns, such lateral oscillations could cancel the forces generated by the two opposite sides and prevent from impact damage to the head. The horn and internal bone were shown to absorb a significant portion of the initial kinetic energy. The horn played a critical role in dissipating energy and mitigating translational and

rotational accelerations, which were the main cause of head concussion. The internal trabecular bone was found to provide sufficient bending stiffness when the horn sheath was subjected to localized compressive load. Drake et al. did an excellent investigation on energy absorption and impact pulse dissipation of horn sheath and internal trabecular bone; however, there were limitations of the study such as the use of isotropic, linear elastic and homogeneous materials in the FE model of the horn and internal bone. In addition, the material properties used for dynamic impact simulations were taken from quasi-static tests that did not consider strain-rate effects that were shown by previous studies.

Lee et al. investigated the effect of horn ridges on stress wave propagation under impact pulses (Lee et al. 2019). They developed a simplified FE model of the horn with isotropic material properties to study normal and shear stresses and strains in four selected regions of the horn under different impact pulses. It was found that the horn ridges could increase the shear stress during impact and reduce the subsequent shear vibrations. They concluded that horn ridges were critical to transferring longitudinal waves to shear waves, further filtering shear waves, and finally reducing the strains to stabilize the whole structure. The special tapered spiral structure could decrease the impulse in longitudinal direction by triggering shear stresses and the subsequent transverse displacements would further dissipate the impact waves.

In 2021, Johnson et al. (2021) studied the responses of the brain of the bighorn sheep using FE modeling and simulation. In their study, a comprehensive FE model was developed based on CT scans of a horn complex that included horn sheath, internal bone, germinative epithelium, skull, and brain. The effects of hydration and strain rate were incorporated into the constitutive model of the horn keratin. Two levels of hydration were

considered, dry (10% water content) and wet (35% water content), to represent the lower and upper bonds of hydration levels in an actual horn at fresh state. For the wet hydration level, both low and high strain rates were considered in the numerical simulations. The shock mitigation capability of the bighorn sheep horn was confirmed in the study with an acceleration of 607g in the extreme case. It was shown that the horn with high hydration level was more effective in dissipating impact pulses than that with low hydration level. Similar to other prior studies, material anisotropy was not considered for both the wet and dry horn keratins. In addition, validation of the horn's constitutive model using coupon testing was not reported.

Among the limited studies related to FE simulation of bighorn sheep horns under dynamic impacts, there is no study that has considered an anisotropic non-linear plastic and viscoelastic material for the horn sheath. The trabecular structures of the bony core were ignored in most of studies and the interface between core and sheath has not been investigated. The angle of incidents in the impact locations has also not been investigated to included side impact or oblique impact.

1.3 Dissertation Research

Research results from existing studies confirmed through electron optical examination and mechanical testing that the keratin sheath of the bighorn sheep horn is an anisotropic material. Based on compression and tensile tests in the radial direction (i.e., the impact direction when ramming), longitudinal direction (i.e., the horn's growing direction), and transverse direction (i.e., the circumferential direction of the horn), the keratin sheath

was shown to have clearly different stress-strain responses in different directions. In the longitudinal direction, the keratin sheath has the highest stiffness to withstand uniaxial stresses and in the radial direction, it has the highest toughness for energy absorption and dissipation. This anisotropy can also be explained by the macrostructure of the tubule-lamellae that is similar to fiber reinforced laminated composites. The horn keratin also exhibits strong strain-rate dependency as revealed through the comparison of quasi-static test data and dynamic impact test data. Although many existing studies investigated the energy dissipation mechanism of the bighorn sheep horn using FE modeling and simulation, no study incorporated strain-rate dependence as well as anisotropic material properties in the FE models of horn sheaths. Research is needed to bridge these gaps so as to improve the model fidelity for the analysis of horn sheaths.

In this dissertation research, a constitutive model was developed for the horn material with anisotropic material properties coupled with strain-rate effect from 10^{-3}/s to 10^{3}/s. The anisotropic feature of the horn material was mainly focused on the large discrepancy between material properties in the longitudinal and radial direction, and the horn material was considered as transversely isotropic (in radial and circumferential directions) for simplification. Compression test data in the longitudinal and radial directions at different strain rates were used to derive the constitutive responses of the horn material. An anisotropic material model with anisotropic hardening was developed in this study and integrated with commercial FE code as a user subroutine. This constitutive model was then validated against test data and finally incorporated into the horn model for dynamic impact analysis.

The remaining portion of this dissertation is organized as follows: Chapter Two gives the fundamental theory of FE modeling of contact problems including contact handling methods and algorithms. In Chapter Three, detailed characterization of test data of the horn material is provided. A user-defined constitutive model of the horn material is developed and thoroughly discussed, including the formulations and stress update method. Chapter Three also includes validation of the constitutive model using quasi-static test data. Strain-rate effect is coupled into the validated quasi-static constitutive model and a new, strain-rate dependent model is developed and presented in Chapter Four. In Chapter Five, the FE model of a full horn is developed to incorporate the strain-rate dependent constitutive model for dynamic impact simulations in which the stress distributions, displacement wave propagations, and energy conversions are studied and discussed. Finally, some major findings and key contributions of this research are summarized in Chapter Six along with a few concluding remarks.

CHAPTER 2: FINITE ELEMENT MODELING FOR CONTACT PROBLEMS

Contact handling is an essential part of FE modeling of impact problems that involve interactions among different bodies or components. Common examples of contact problems are seen in cases such as vehicular crashes, stamping processes, and metal forming. It is necessary to carefully select the proper contact setting (i.e., contact definitions and algorithms) to improve the fidelity of FE simulations, especially in those with large deformations.

Since the contact theory behind the different commercial FE codes, such as LS-Dyna, Abaqus, and Ansys, is essentially the same, the contact definitions, methods, and algorithms implemented in LS-Dyna, are presented in this chapter and used in the simulations of this research.

2.1 Contact Theory

In contact analysis, methods and algorithms are needed to handle the interactions between two contacting bodies that initially are not in contact. The contact interfaces on the two bodies are typically defined as a master and a slave surface. In contact modeling, the contact surface with stiffer material or coarser mesh is usually chosen as the master surface to provide stable contact analysis. There are three methods for contact handling in LS-Dyna: the kinematic constraint method, distributed parameter method, and penalty method (LSTC, 2019). Both the kinematic constraint method and distributed parameter

method deal with contact problems by confining one contact interface along the other interface and do not allow for penetration. In the kinematic constraint method, the constraints are imposed on nodes along the contact interfaces for their degrees of freedom normal to the contact surfaces. A potential issue of this method is that some nodes may be determined as inactive when the mesh of the master surface is finer than that of the slave surface: some nodes on the master surface may not be fully captured by the boundary of the slave surface, leading to undesired penetration. In the distributed parameter method, the mass and internal pressure of the elements from the slave surface are distributed to the covered area on the master surface. Constraints are then imposed on slave nodes for accelerations and velocities to insure their movements along the master surface and without penetration.

While both the kinematic constraint method and distributed parameter method do not allow penetrations from slave nodes to the master surface, the penalty method artificially introduces a small penetration before intervention. Once the contact algorithm detects that certain nodes have penetrated the other surface, the interface springs are placed between all penetrating nodes and the contact surface to provide contact forces that push back the penetrated nodes from the contact surface. Based on the formulations to determine the stiffness of the interface spring, the penalty method can be categorized into three different methods: standard penalty formulation, soft constraint penalty formulation, and segment-based penalty formulation.

2.1.1 Standard Penalty Formulation

The standard penalty formulation is the most basic penalty-based contact algorithm if one slave node is detected to have penetrated the master surface, a normal interface force will be imposed between the slave node and the corresponding contact point in the segment on the master surface. A segment is the basic unit for contact handling in contact algorithms. For surfaces composed of shell elements, a segment is the surface formed by the nodes of a shell element, either triangular or quadrilateral depending on the type of the element. For contact surfaces formed by solid elements, a segment is defined as the exterior face of the solid element. Figure 2.1 shows two examples of the segments on the surfaces of a shell and solid element (marked with a cross).

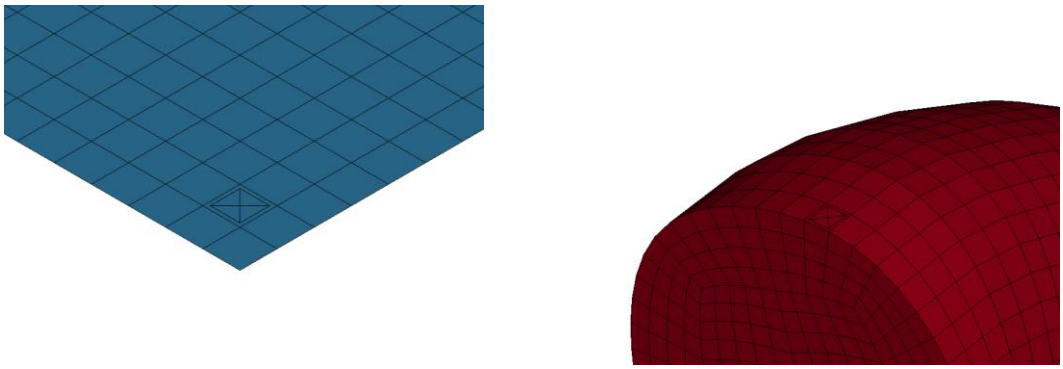

(a) (b)

Figure 2.1: Examples of segments on contact surfaces (marked by a cross).

(a) Surface formed by shell elements; and (b) Surface formed by solid elements.

Figure 2.2 illustrates penetration checking between a slave node and a segment on the master surface in a contact algorithm.

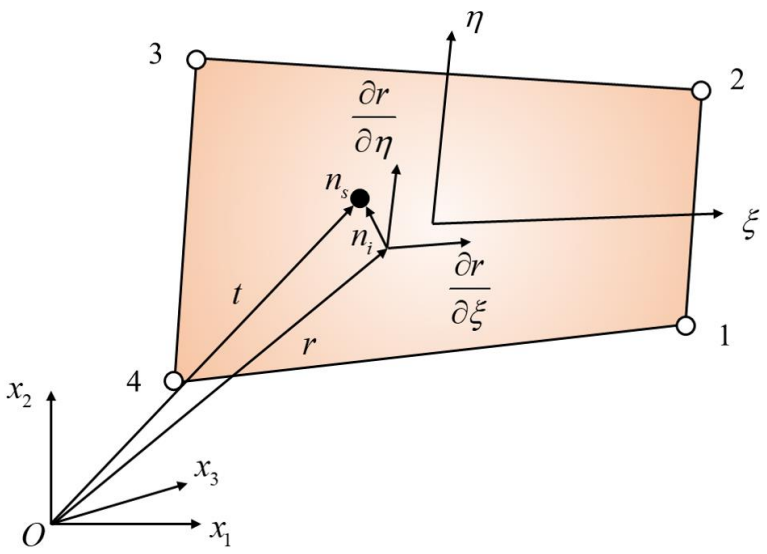

Figure 2.2: Standard penalty formulation (LS-Dyna manual).

The slave node, denoted by n_s, is checked by contact algorithm for penetration, which occurs if the condition in Eq. (2.1) is met:

$$l = \boldsymbol{n}_i \cdot [\boldsymbol{t} - \boldsymbol{r}(\xi_c, \eta_c)] < 0 \tag{2.1}$$

where ***t*** and ***r*** are the vectors from the origin of the global coordinate system to the slave node and contact point, respectively. The normal unit vector from contact point to the master segment is denoted as

$$\boldsymbol{n}_i = \boldsymbol{n}_i(\xi_c, \eta_c) \tag{2.2}$$

The penetration of a slave node n_s to a master segment can be determined by checking Eq. (2.1). When l is greater than zero ($l > 0$), the slave node has no contact with the master segment and thus no penetration occurs. When l is less than zero ($l < 0$), the slave node has penetration into the master segment and the penetration distance is given by $| l |$. If a penetration is detected, a contact force will be calculated and applied to the slave node and the master segment as

$$\boldsymbol{f}_s = -lk_i\boldsymbol{n}_i \tag{2.3}$$

where k_i is the contact stiffness. For shell element, the contact stiffness of the master segment, k_i, is determined by the geometry of the shell element containing s_i as well as the bulk modulus of material, given by

$$k_i = \frac{f_{si}K_iA_i^2}{\max(\text{shell diagonal})} \tag{2.4}$$

where K_i is the bulk modulus, A_i is the area of the shell element on the master segment, and f_{si} is a scale factor that has a default value of 0.1 and is used to adjust the contact stiffness to maintain numerical stability when handling contact problems.

For solid elements, the contact stiffness is given by

$$k_i = \frac{f_{si}K_iA_i^2}{V_i} \tag{2.5}$$

where A_i is the face area of the solid element on the master segment and V_i is the volume of the solid element.

Since the bodies in contact may have significantly different material properties and thus stiffness, several options are available for users to set the proper value of penalty contact stiffness to prevent numerical instability of contact modeling. In the standard penalty formulation, the commonly used method is to use the smaller one of the master segment stiffness and slave node stiffness as the penalty stiffness. Other options such as only using master segment stiffness, using slave node stiffness with or without mass weighted can be found in the LS-Dyna user manual.

2.1.2 Soft Constraint Penalty Formulation

The soft constraint penalty formulation is developed for soft materials that may cause excessive penetrations and consequently numerical instability when using the standard penalty formulation in contact analysis. In addition to contact stiffness, another stability contact stiffness $k_{cs}(t)$ is introduced based on the Courant criteria and calculated by

$$k_{cs}(t) = 0.5 \cdot \text{SOFSCL} \cdot m^* \cdot \left(\frac{1}{\Delta t_c(t)} \right)^2 \tag{2.6}$$

where SOFSCL is a scale factor for the constraint force of soft constraint option, $\Delta t_c(t)$ is the solution timestep at time instant t, and m^* is a function of the masses of the slave and master nodes given by

$$m^* = \frac{m_1 m_2}{m_1 + m_2} \tag{2.7}$$

In Eq. (2.7), m_1 and m_2 are masses of the slave node and the master node, respectively. The mass of master node is the interpolated value from four nodes of the master segment.

The stability contact stiffness is adjusted dynamically based on the varying timestep and to achieve stable contact handling. In a contact analysis using the soft constraint penalty formulation, the standard penalty contact stiffness k_{cs} and the stability contact stiffness $k_{cs}(t)$ are compared and the larger one is chosen as the contact stiffness, $k_{SOFT=1}$, which is used to calculate the contact forces.

$$k_{SOFT=1} = \max(k_{cs}, k_{cs}(t)) \tag{2.8}$$

2.1.3 Segment-based Penalty Formulation

In segment-based penalty formulation, the stability contact stiffness is determined similarly to that in the soft constraint penalty formulation but with different methods of calculating the mass and updating the timestep. Segment mass, which is defined as the element mass for shell elements and half of the element mass for solid elements, is used instead of the nodal masses used in the soft constraint penalty formulation. The timestep $\Delta t_c(t)$ is updated only when the current solution timestep is 5% more than the initial timestep. The contact stiffness in the segment-based penalty formulation, $k_{\text{SOFT=2}}$, is given by

$$k_{\text{SOFT=2}} = \max(k_{cs}, k_{cs}^{*}(t)) \tag{2.9}$$

where $k_{cs}^{*}(t)$ is the stability contact stiffness for segment-based penalty formulation and is determined by

$$k_{cs}^{*}(t) = 0.5 \cdot \text{SLSFAC} \cdot \left\{ \begin{matrix} \text{SFS} \\ \text{or} \\ \text{SFM} \end{matrix} \right\} \cdot \left(\frac{m_1 m_2}{m_1 + m_2} \right) \cdot \left(\frac{1}{\Delta t_c\,(t)} \right)^2 \tag{2.10}$$

In Eq. (2.10), SLSFAC is a scale factor for sliding interface penalties, SFS and SFM are scale factors for default slave and master penalty stiffnesses, respectively, and m_1 and m_2 are the masses of the slave and master segments. As defined in LS-Dyna, the mass of a shell segment is its element mass, and the mass of a solid segment is half of the solid element mass.

2.1.4 Contact Friction

Contact sliding energy is generated through friction between two contact surfaces. The friction defined in LS-Dyna is based on the Coulomb formulation. The coefficient of friction μ is interpolated using the coefficient of static friction μ_s and the coefficient of dynamic friction μ_d with an exponential decay given by a coefficient c and the relative velocity $\boldsymbol{v}_{vel}$ of the two surfaces in contact:

$$\mu = \mu_d + (\mu_s - \mu_d)e^{-c|\boldsymbol{v}_{rel}|} \tag{2.11}$$

The friction force between the contacting surfaces, F_y, is given by

$$F_y = \mu|\boldsymbol{f}_n| \tag{2.12}$$

where $\boldsymbol{f}_n$ is the normal contact force.

The displacement of the slave node after one timestep can be denoted by

$$\Delta\boldsymbol{e} = \boldsymbol{r}^{n+1}\left(\xi_c^{n+1}, \eta_c^{n+1}\right) - \boldsymbol{r}^{n}\left(\xi_c^{n}, \eta_c^{n}\right) \tag{2.13}$$

where $\boldsymbol{r}^{n}\left(\xi_c^{n}, \eta_c^{n}\right)$ and $\boldsymbol{r}^{n+1}\left(\xi_c^{n+1}, \eta_c^{n+1}\right)$ are the vectors from the origin of the global coordinate system to the slave node at two subsequent states, n and n+1, respectively.

The relative velocity $\boldsymbol{v}_{vel}$ between the slave node and the master segment is given by

$$\boldsymbol{v}_{rel} = \frac{\Delta\boldsymbol{e}}{\Delta t} \tag{2.14}$$

where Δt is the time step size.

Let $\boldsymbol{f}^n$ be the frictional force at the current state, an internal trial force is introduced as

$$\boldsymbol{f}^{*} = \boldsymbol{f}^{n} - k\Delta\boldsymbol{e} \tag{2.15}$$

where k is the interface stiffness. Then the updated Coulomb frictional force is defined as

$$\boldsymbol{f}_{\text{Coulomb}}^{n+1} = \begin{cases} \boldsymbol{f}^{*} & \text{if } \left|\boldsymbol{f}^{*}\right| \le F_y \\ \dfrac{F_y \boldsymbol{f}^{*}}{\left|\boldsymbol{f}^{*}\right|} & \text{if } \left|\boldsymbol{f}^{*}\right| > F_y \end{cases} \tag{2.16}$$

To cap the excessive Coulomb friction force generated by interface shear stress, a limit on the surface tangential force is composed:

$$f^{n+1} = \min(\left|\boldsymbol{f}_{\text{Coulomb}}^{n+1}\right|, \kappa A_{\text{master}}) \tag{2.17}$$

where κ is the viscous coefficient and A_{master} is the area of master segment.

2.1.5 Contact Energy

The contact energy from the current (n^{th}) state to the (n+1)$^{\text{th}}$ state is updated by

$$E_{\text{contact}}^{n+1} = E_{\text{contact}}^{n} + \left[\sum_{i=1}^{nsn} \Delta F_i^{\text{slave}} \cdot \Delta d_i^{\text{slave}} + \sum_{j=1}^{nmn} \Delta F_j^{\text{master}} \cdot \Delta d_j^{\text{master}} \right]^{n+\frac{1}{2}} \tag{2.18}$$

where $\Delta F_i^{\text{slave}}$ is the interface force between the i-th slave node and the contact segment, $\Delta d_i^{\text{slave}}$ is the moving distance increment at the current timestep from i-th slave node, $\Delta F_j^{\text{master}}$ is the interface force between the j-th master node and the contact segment, $\Delta d_j^{\text{master}}$ is the moving distance increment in current timestep from j-th master node, *nsn* is the numbers of slave nodes, and *nmn* is the number of master nodes.

The total net contact energy from the slave and master surfaces should equal to the energy storage in the system. In an ideal situation without friction, the contact energy from

the slave surface should be the same as the contact energy from the master surface without any energy lost. When friction or damping is considered, a portion of the contact energy from the slave and master surfaces is converted to the sliding interface energy or damping energy.

2.2 Contact Algorithms in LS-Dyna

2.2.1 Surface-to-Surface Contact

The surface-to-surface contact in LS-Dyna is based on a kinematic partitioned approach developed by Taylor and Flanagan (1989). In surface-to-surface contact, each master surface accumulates masses and forces from the slave surface for a portion of time partitioned by the factor, β ($-1 < \beta < 1$), then switched over. That means when $\beta = 1$, the contact is a one-way treatment that only the master surface accumulates forces from the slave surface, and vice versa when $\beta = -1$.

A trial state was firstly updated without contact interaction to obtain trial values of acceleration, velocity, and displacement. After the trial state, the acceleration will be corrected by considering contact penetrations. For a slave node, the penetration force can be expressed as

$$\boldsymbol{f}_p = \frac{m_s \Delta L}{\Delta t^2} \boldsymbol{n} \tag{2.19}$$

where m_s is mass of the slave node, ΔL is the penetration distance, $\boldsymbol{n}$ is the normal vector of the master surface, and Δt is the time step size.

It was assumed that the acceleration of a slave node, which resided and constrained by its contacting master surface, is consistent with the master segment. The slave node acceleration $\boldsymbol{a_s}$ can be expressed as

$$\boldsymbol{a}_s = \phi_1 \boldsymbol{a}_{nk}^1 + \phi_2 \boldsymbol{a}_{nk}^2 + \phi_3 \boldsymbol{a}_{nk}^3 + \phi_4 \boldsymbol{a}_{nk}^4 \tag{2.20}$$

where $\boldsymbol{a}_{nk}^1$, $\boldsymbol{a}_{nk}^2$, $\boldsymbol{a}_{nk}^3$, $\boldsymbol{a}_{nk}^4$ are the accelerations of the four nodes of the master segment *k*, and ϕ_1, ϕ_2, ϕ_3, ϕ_4, are the corresponding shape functions. By accumulating all the penetrated slave nodes for its nodal masses and penetration forces to the global master surface, it gives

$$\left(m_k + \sum_s m_{ks} \right) \boldsymbol{a}_{nk} = \sum_s \boldsymbol{f}_{ks} \tag{2.21}$$

where $\boldsymbol{a_{nk}}$ is the acceleration vector of master segment, m_k is the mass of master segment *k*, and m_{ks} is given by

$$m_{ks} = \phi_k m_s, \ \boldsymbol{f_{ks}} = \phi_k \boldsymbol{f_p} \tag{2.22}$$

The corresponding shape function is denoted as ϕ_k. After solving master acceleration vector $\boldsymbol{a_{nk}}$ and substituting it into Eq. (2.21), the acceleration of slave node $\boldsymbol{a_s}$ can be interpolated and the acceleration correction for slave node is

$$\boldsymbol{a_{ns}} = \boldsymbol{a_s} - \frac{\boldsymbol{f_p}}{m_s} \tag{2.23}$$

The acceleration is calculated again by switching the master and slave surfaces and the average acceleration correction is obtained by

$$\boldsymbol{a}_n^{\text{final}} = \frac{1-\beta}{2} \boldsymbol{a}_n^{\text{1st pass}} + \frac{1+\beta}{2} \boldsymbol{a}_n^{\text{2st pass}} \tag{2.24}$$

The acceleration correction is added to the trial acceleration to obtain the final value for acceleration. The surface-to-surface contact has an option of “automatic” that searches for contact and penetration on both master and slave surfaces.

The surface-to-surface contact is normally adopted for solving problems in which a simple contact path is expected such as two parts with simple geometries and without self-warpage during contact. Under such circumstances, the surface-to-surface contact is computationally efficient while maintaining high modeling accuracy. However, due to the lack of self-contact checking, surface-to-surface contact may cause inaccurate modeling issues such as the case shown in Figure 2.3. In Figure 2.3, the block on top is compressing a tube whose top and bottom inner surfaces may be in contact under large compressive forces. For the case as in Figure 2.3, surface-to-surface contact is not capable of handling the contact between the top and bottom inner surfaces of the tube; another algorithm called single-surface contact should be used to maintain modeling accuracy.

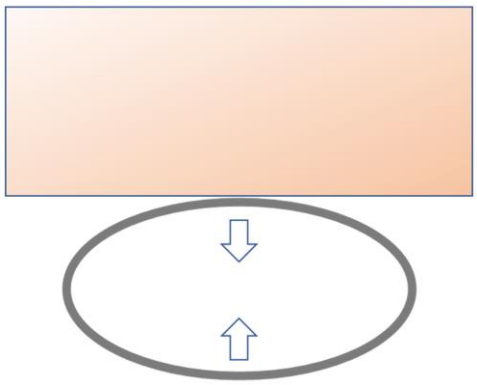

Figure 2.3: Example of self-contact case.

2.2.2 Single-Surface Contact

The single-surface contact is the most commonly used and robust contact algorithm in LS-Dyna. It was evolved from surface-to-surface contact and share similar contact searching and acceleration calculation formulations. However, it has much more

advantages over the surface-to-surface contact algorithm. In single-surface contact, there is no need to explicitly define the slave and master parts, because the algorithm conducts penetration checking among all the parts included in the contact definition: the contact between two parts and the contact between different areas on the same part (self-contact). It is a common practice to include all the components with potential contacts in a single single-surface contact with the "automatic" option for handling complicated problems such as vehicular crashes.

There are two major types of contact for single-surface contact: Type 4 and Type 13. The Type 4 single-surface contact projects the contact interface using the nodal normal vectors from the master surface as shown in Figure 2.4. For shell segment, the offset distance on both sides at each node is defined as the half nodal thickness of the element. The contact interface shown in Figure 2.4 is unsmooth and may cause instability issue when the slave node contacts the projected interface at the sharp corner.

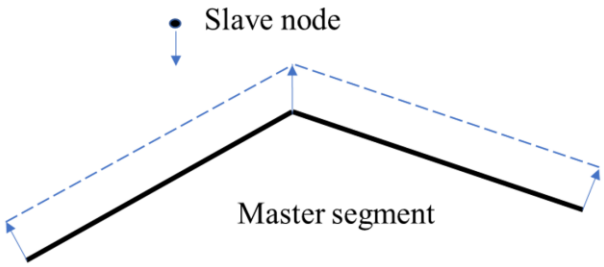

Figure 2.4: Projection of the contact interface in Type 4 single-surface contact.

The projection of the contact interface was refined in Type 13 single-surface contact. Figure 2.5 illustrates the method for penetration detection in the Type 13 single-surface contact. For shell element, the contact interface is projected from the master

segment in the direction of the normal vector for an offset distance, which is defined as half of the element thickness. For solid element, the offset distance is zero; no projection of the contact interface is necessary. The projected interfaces are used for checking if a slave node has any penetration into the master segment. For adjacent segments that do not have a 180° angle, special handling at the intersection of the two segments is needed to prevent unsmooth contact interfaces such as the one shown in Figure 2.4.

To bridge the discontinuity between the projected contact interfaces of two adjacent segments, a cylindrical surface is created with the center at the intersection of the mid-planes of the two segments, as shown in Figure 2.5. The entire surface created by the two projected contact interfaces and the cylindrical surface is used for checking penetrations from the slave nodes.

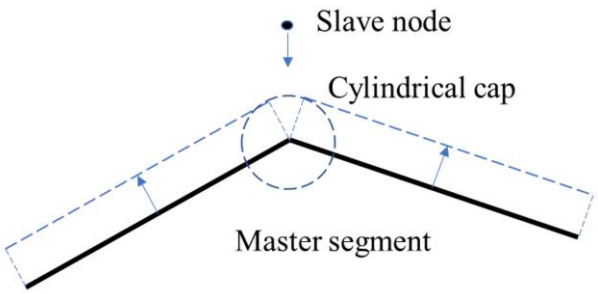

Figure 2.5: Projection of the contact interface in Type 13 single-surface contact.

The general idea of the automatic-single-surface contact algorithm can be summarized as follows.

(1) Conduct segment-based bucket sorting and identify the closest segment for each of the slave nodes;

(2) For each slave node, check whether the node is in contact with the master segment. Update the closest segment and flag the contact side of the surface;

(3) Apply contact forces at nodes where penetrations are detected; and

(4) Switch the slave and master parts and perform contact checking again.

2.2.3 Automatic-General Contact

The automatic-general contact is another commonly used contact algorithm in LS-Dyna that is mainly for dealing with edge contact. Figure 2.6 gives an example of edge contact in which two surfaces composed of shell elements are in contact at edges. In this situation, single-surface and surface-to-surface contacts may not handle the contacts well because both contact algorithms detect penetrations by offsetting the contact interface using vectors normal to the origin surfaces. With automatic-general contact, a beam element with null material (i.e., with no stiffness but only the cross-section geometry) is artificially created along the exterior edge of the original surface. The contact between two edges of the shell surfaces is then converted to the contact between two beam elements on their contact edges. There is also an “interior” option for the automatic-general contact in which null beam elements are also created along the interior edges of the contact surfaces. This option is widely used for cases involving potential interior edge contacts to prevent penetrations caused by undetected interior contacts.

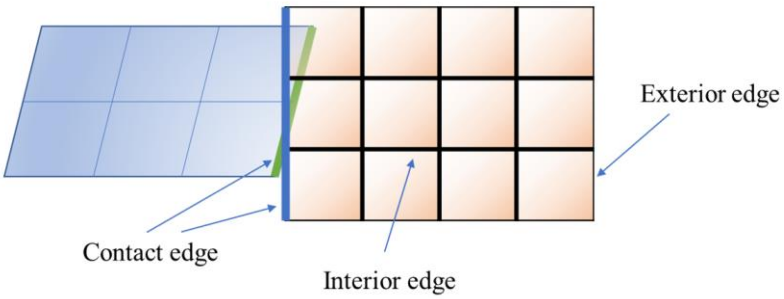

Figure 2.6: Example of edge contact case.

2.3 Hourglass Control

In finite element simulation, under-integrated elements, such as the constant-stress solid element with one integration point, are commonly chosen for its reduced computational cost. However, using under-integrated elements may often cause a non-physical deformation state called hourglass mode that has a negative volume of the element and thus produces no meaningful stress values. The existence of hourglass modes can cause contact penetrations and/or abnormal interface reaction forces.

To avoid hourglass modes, hourglass control is adopted in finite element analysis to apply an artificial internal force to resist hourglass deformation of the element. Based on the way to generate the internal force, two types of hourglass controls were developed: the viscous form (Type 1, Type 2, and Type 3 in LS-Dyna) and the stiffness form (Type 4, Type 5, and Type 6). The viscous form hourglass control generates hourglass force that is proportional to the nodal velocity while the stiffness form hourglass control generates hourglass force that is proportional to the nodal displacement.

The energy associated with the hourglass internal force is called hourglass energy. The following requirement should be met to maintain modeling accuracy if introducing hourglass energy into the system. The hourglass energy of the part that is assigned with hourglass control should below 10% of its peak internal energy. Under this condition, the range of hourglass energy is considered as acceptable.

In this study, to accurately handle contacts in both quasi-static and dynamic loading conditions, the automatic-single-surface contact with segment-based is chosen as the major contact modeling method. The frictional and sliding behaviors between contact interfaces are also considered. Under-integrated elements with Type 4 (stiffness form) hourglass control were used in the models of this study. In the next chapter, a constitutive material model will be developed using finite element theory, cooperating with contact setting to solve for the deformation of horn under typical mechanical loadings.

CHAPTER 3: CONSTITUTIVE MODELING OF HORN MATERIAL

The horn sheath of bighorn sheep is made of keratin-based material with tubule-lamella structure. Similar to fiber-reinforced laminated composites, horn sheath is considered as anisotropic material, i.e., with different mechanical properties in the principal directions that are defined as longitudinal, radial, and circumferential directions based on the exterior geometry of a horn (see Figure 3.1). The longitudinal direction is the growing direction of the horn starting from the proximal base (the location where the horn is connected to the head) to the distal end (i.e., horn tip). The extending direction of tubules in the horn sheath is aligned with the longitudinal direction. The radial direction, which extends from the inner core of the horn to the exterior skin and is perpendicular to the longitudinal direction, is the principal direction to sustain impact loading during bighorn sheep ramming. As discussed in Chapter 1, the macrostructure of the horn sheath is composed of tubules in the longitudinal direction and surrounded by layers of lamellas stacked in the radial direction. The last principal direction, circumferential direction, is in the tangent direction on a cross-section of the horn and perpendicular to the radial direction.

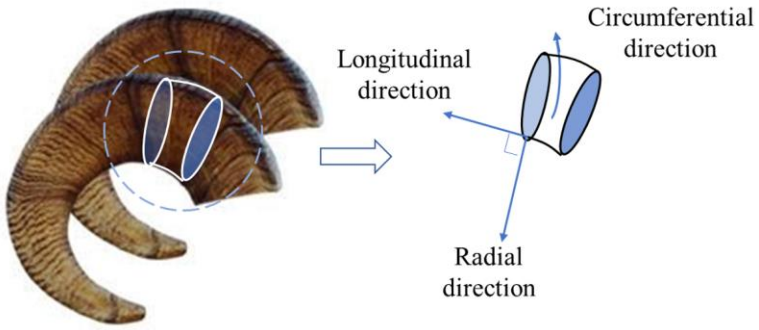

Figure 3.1: The principal directions of the horn.

Over the years, extensive mechanical tests have been performed and the results have showed that there are differences in the material characteristics in the three principal directions, especially between the longitudinal and radial directions. These differences include material properties such as Young's modulus, yield strength, and hardening behaviors under plastic deformations. A simplified approach to model the anisotropic materials of the horn sheath is to treat it as transversely isotropic materials that are isotropic in the radial and circumferential directions.

In this chapter, an anisotropic constitutive model is developed for the horn material to represent the elastic and plastic behaviors under quasi-static loading conditions. A user-defined material subroutine was implemented and integrated with LS-Dyna and validated against test data that were taken from typical loading scenarios such as uniaxial compression tests in the radial and longitudinal directions. The test data were used for material characterization, model parameterization and validation.

3.1 Preliminary

In this section, the preliminary knowledge of constitutive modeling is presented on the constitutive relationship of stresses and strains, yield criteria involving anisotropy, and the anisotropic hardening rules.

3.1.1 Orthogonal Material

In the 1-2-3 coordinate system, the Cauchy stress tensor $\boldsymbol{\sigma}$ and elastic strain tensor $\boldsymbol{\varepsilon}$ are defined as

$$\boldsymbol{\sigma} = \left[\sigma_{11}, \sigma_{22}, \sigma_{33}, \sigma_{12}, \sigma_{23}, \sigma_{31}\right]^T \tag{3.1}$$

$$\boldsymbol{\varepsilon} = \left[\varepsilon_{11}, \varepsilon_{22}, \varepsilon_{33}, 2\varepsilon_{12}, 2\varepsilon_{23}, 2\varepsilon_{31}\right]^T \tag{3.2}$$

and the relationship between them is given by

$$\boldsymbol{\sigma} = \boldsymbol{C} \cdot \boldsymbol{\varepsilon} \tag{3.3}$$

where $\boldsymbol{C}$ is the stiffness matrix.

The compliance form of orthogonal material is given by

$$\boldsymbol{\varepsilon} = \boldsymbol{S} \cdot \boldsymbol{\sigma} \tag{3.4}$$

The compliance matrix $\boldsymbol{S}$ is defined as

$$\boldsymbol{S} = \begin{bmatrix} \frac{1}{E_{11}} & -\frac{\nu_{21}}{E_{22}} & -\frac{\nu_{31}}{E_{33}} & 0 & 0 & 0 \\ -\frac{\nu_{12}}{E_{11}} & \frac{1}{E_{22}} & -\frac{\nu_{32}}{E_{33}} & 0 & 0 & 0 \\ -\frac{\nu_{13}}{E_{11}} & -\frac{\nu_{23}}{E_{22}} & \frac{1}{E_{33}} & 0 & 0 & 0 \\ 0 & 0 & 0 & \frac{1}{E_{12}} & 0 & 0 \\ 0 & 0 & 0 & 0 & \frac{1}{E_{23}} & 0 \\ 0 & 0 & 0 & 0 & 0 & \frac{1}{E_{31}} \end{bmatrix} \tag{3.5}$$

where $\boldsymbol{E}_{11}$, $\boldsymbol{E}_{22}$, $\boldsymbol{E}_{33}$ are the Young's moduli of the orthogonal material in the 1, 2, and 3 directions, $\boldsymbol{E}_{12}$, $\boldsymbol{E}_{23}$, $\boldsymbol{E}_{31}$ are the shear moduli in 1-2, 2-3, and 3-1 planes, and v is the Poisson's ratio defined as the ratio of transverse and axial strains given by

$$\nu_{at} = -\frac{\varepsilon_t}{\varepsilon_a} \tag{3.6}$$

where ε_a is the strain in the axial direction, ε_t is the strain in transverse direction induced by the axial stress, and ν_{at} represents the Poisson's effect in the t-direction induced by the stress in a-direction.

The upper limit of Poisson's ratio for common materials can be determined based on non-negativity of its bulk modulus using a simplified isotropic model with a Young's modulus of E and Poisson's ratio v. Let a, b, and c be the dimensions of a cubic sample along the three orthogonal axes 1, 2, and 3, and Δa, Δb, and Δc be the corresponding dimensional increments during time interval Δt. The volumes in the deformed and initial states can be described as

$$V_t = (a + \Delta a) \cdot (b + \Delta b) \cdot (c + \Delta c) \tag{3.7}$$

$$V_0 = abc \tag{3.8}$$

Equation (3.7) can be simplified to

$$V_t = V_0 + bc\Delta a + ca\Delta b + ab\Delta c + o(\Delta^2) \tag{3.9}$$

and the volume change is

$$\Delta V = bc\Delta a + ca\Delta b + ab\Delta c \tag{3.10}$$

The volumetric strain is given as

$$\begin{aligned} \varepsilon_V &= \frac{\Delta V}{V_0} \\ &= \frac{bc\Delta a + ca\Delta b + ab\Delta c}{abc} \\ &= \frac{\Delta a}{a} + \frac{\Delta b}{b} + \frac{\Delta c}{c} \\ &= \varepsilon_{11} + \varepsilon_{22} + \varepsilon_{33} \end{aligned} \tag{3.11}$$

and with Hooke's law, Eq. (3.11) can be expressed in terms of σ_{11}, $\sigma_{22,}$ σ_{33} as

$$\varepsilon_V = \frac{3(1-2\nu)}{E} \cdot \sigma_m \tag{3.12}$$

where σ_m is the hydraulic pressure given by

$$\sigma_m = \frac{\sigma_{11} + \sigma_{22} + \sigma_{33}}{3} \tag{3.13}$$

With Eqs. (3.12) and (3.13), the bulk modulus can be determined as

$$K = \frac{\sigma_m}{\varepsilon_V} = \frac{E}{3(1-2\nu)} \tag{3.14}$$

The bulk modulus is defined as a positive material characteristic that requires the Poisson's ratio to be smaller than 0.5. For incompressible material such as rubber, the Poisson's ratio is found to reach this limit. The reported values of Poisson's ratio for keratin horn sheath range from 0.25 to 0.35.

From the symmetry of the compliance matrix

$$\frac{\nu_{12}}{E_{11}} = \frac{\nu_{21}}{E_{22}},\ \frac{\nu_{13}}{E_{11}} = \frac{\nu_{31}}{E_{33}},\ \frac{\nu_{23}}{E_{22}} = \frac{\nu_{32}}{E_{33}} \tag{3.15}$$

The compliance matrix in Eq. (3.5) can be expressed in terms of nine independent variables as

$$\boldsymbol{S} = \begin{bmatrix} S_{11} & S_{12} & S_{13} & 0 & 0 & 0 \\ S_{12} & S_{22} & S_{23} & 0 & 0 & 0 \\ S_{13} & S_{23} & S_{33} & 0 & 0 & 0 \\ 0 & 0 & 0 & S_{44} & 0 & 0 \\ 0 & 0 & 0 & 0 & S_{55} & 0 \\ 0 & 0 & 0 & 0 & 0 & S_{66} \end{bmatrix} \tag{3.16}$$

Similarly, the stiffness matrix can be expressed as

$$\boldsymbol{C} = \begin{bmatrix} C_{11} & C_{12} & C_{13} & 0 & 0 & 0 \\ C_{12} & C_{22} & C_{23} & 0 & 0 & 0 \\ C_{13} & C_{23} & C_{33} & 0 & 0 & 0 \\ 0 & 0 & 0 & C_{44} & 0 & 0 \\ 0 & 0 & 0 & 0 & C_{55} & 0 \\ 0 & 0 & 0 & 0 & 0 & C_{66} \end{bmatrix} \tag{3.17}$$

It can be seen from Eqs. (3.3) and (3.4) that the stiffness matrix is the inverse of the compliance matrix and vice versa; therefore, the stiffness matrix can be calculated by

$$\boldsymbol{C} = \boldsymbol{S}^{-1} \tag{3.18}$$

with entry representations given as

$$\begin{gathered} C_{11} = \frac{S_{22}S_{33} - S_{23}^2}{\Theta},\ C_{22} = \frac{S_{11}S_{33} - S_{13}^2}{\Theta},\ C_{33} = \frac{S_{11}S_{22} - S_{12}^2}{\Theta} \\ C_{12} = \frac{S_{12}S_{33} - S_{13}S_{23}}{\Theta},\ C_{13} = \frac{S_{13}S_{22} - S_{12}S_{23}}{\Theta},\ C_{23} = \frac{S_{23}S_{11} - S_{12}S_{13}}{\Theta} \\ C_{44} = \frac{1}{S_{44}},\ C_{55} = \frac{1}{S_{55}},\ C_{66} = \frac{1}{S_{66}} \\ \text{where } \Theta = S_{11}S_{23}^2 + S_{22}S_{13}^2 + S_{33}S_{12}^2 - S_{11}S_{22}S_{33} - 2S_{12}S_{13}S_{23} \end{gathered} \tag{3.19}$$

Since the entries in the compliance matrix are given in Eq. (3.5), the stiffness matrix in Eq. (3.18) can be determined using the given material properties.

3.1.2 Yield Criterion

In multi-dimensional stress states, the yield criterion can be described using a yield function given as

$$f = \bar{\sigma} - Y \tag{3.20}$$

where $\bar{\sigma}$ is the effective stress and Y is the yield stress. When the effective stress is smaller than the yield stress ($f < 0$), the material undergoes elastic deformation. The material starts to yield when the effective stress reaches the yield limit and the yield surface, $f = 0$, defines all possible stress states that have the same effective stress. Figure 3.2 gives an example of a yield surface in a two-dimensional space of principal stresses.

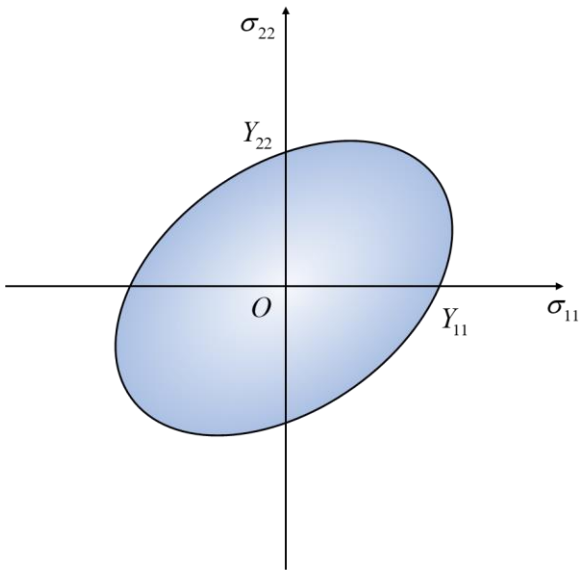

Figure 3.2: A yield surface in a two-dimensional space of principal stresses.

A popular yield criterion is the von Mises criterion that uses von Mises stress as the effective stress that is given by

$$\sigma_e = \sqrt{\frac{1}{2}\left[\left(\sigma_{11}-\sigma_{22}\right)^2+\left(\sigma_{22}-\sigma_{33}\right)^2+\left(\sigma_{33}-\sigma_{11}\right)^2+6\left(\sigma_{12}^2+\sigma_{23}^2+\sigma_{31}^2\right)\right]} \quad (3.21)$$

Hill (1948) proposed a more generalized format of the effective stress for anisotropic materials with three orthogonal planes of symmetry. The three planes of symmetry are mutually orthogonal and meet at three orthogonal directions that are called the principal axes of anisotropy. When choosing the principal axes of anisotropy as the reference axes, a generalized form of the effective stress is given as

$$\bar{\sigma} = \sqrt{\frac{1}{2}\left[F\left(\sigma_{22}-\sigma_{33}\right)^2+G\left(\sigma_{33}-\sigma_{11}\right)^2+H\left(\sigma_{11}-\sigma_{22}\right)^2+2L\sigma_{23}^2+2M\sigma_{31}^2+2N\sigma_{12}^2\right]} \quad (3.22)$$

where F, G, H, L, M, and N are characteristic constants. The effective stress can also be expressed by a tensor representation proposed by Lubliner (2008) as

$$\bar{\sigma} = \sqrt{\boldsymbol{\sigma}^T \boldsymbol{A} \boldsymbol{\sigma}} = \sqrt{A_{ijkl}\sigma_{ij}\sigma_{kl}} \quad (3.23)$$

where $\boldsymbol{A}$ is a 4^{th} order tensor defining the anisotropy of yield. With three principal directions, the anisotropic factor matrix $\boldsymbol{A}$ is given as a 6×6 matrix. Similar to the stiffness matrix, the anisotropic factor matrix is also symmetric and share the same features for off-diagonal entries. The expression of anisotropic factor matrix will be discussed in detail in the following sections.

3.1.3 Hardening Rule

Most real-world materials have plastic hardening behaviors that increase the yield stresses as the materials undergo plastic deformations. A classic example of materials with

plastic hardening is crystalline metal. Based on the dislocation theory, the density of dislocation inside the metal will dynamically change during deformation incited by external loading, affecting the average distance and the repulsive interaction force among dislocations. These changes increase the difficulty for existing dislocations to move, appearing as plastic hardening of the material.

For perfectly plastic material without hardening, the yield surface keeps the original shape after the material reaches the initial yield state and undergoes plastic deformations. With plastic hardening, the yield stress will keep increasing after reaching the initial yield limit and before reaching the ultimate strength. The plastic hardening behavior is indicated by the expansion of the yield surface in the normal directions of the principal-stress space. The expansion of yield surface is associated with the increasing of plastic strain, i.e., plastic flow. The relationship between plastic strain increment and the yield surface expansion can be described by associative plastic flow theory given as

$$d\varepsilon_p = d\lambda \frac{\partial f}{\partial \boldsymbol{\sigma}} \tag{3.24}$$

where ε_p is the current plastic strain, λ is a hardening coefficient, and f is the yield function (also called the plastic potential function) defined in Eq. (3.20). Equation (3.24) shows that the direction of plastic flow is parallel to the tangent direction of the yield surface and is normal to the direction of yield surface expansion.

In terms of the expansion of yield surface, two types of plastic hardening patterns can be identified: isotropic hardening and anisotropic hardening, as illustrated in Figure 3.3.

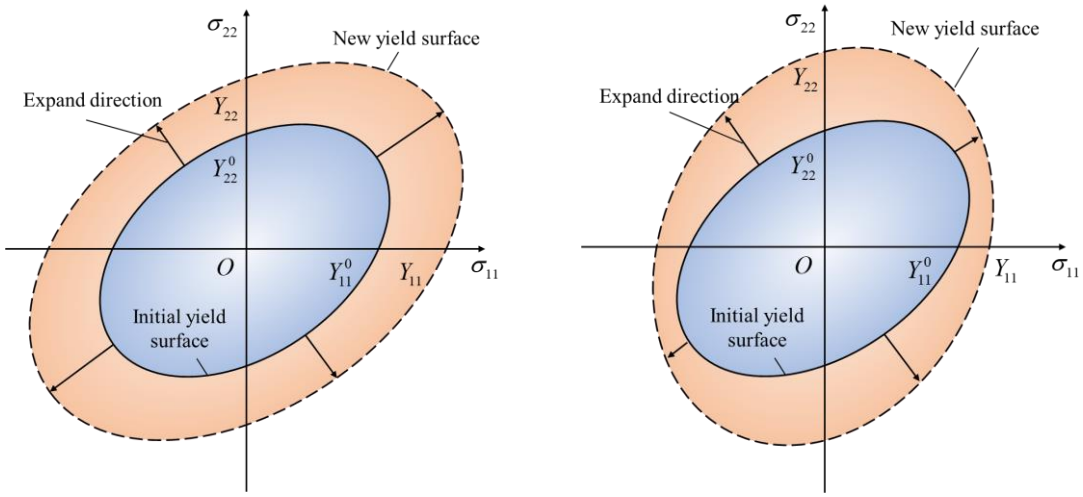

(a) (b)

Figure 3.3: Illustration of plastic hardening patterns in a two-dimensional space of the principal stresses.

(a) Isotropic hardening; and (b) Anisotropic hardening.

In isotropic hardening, the yield surface expands uniformly along its normal directions, as shown in Figure 3.3(a), i.e., the yield surface is enlarged while maintaining the original shape. For anisotropic hardening shown in Figure 3.3(b), the yield surface expands nonuniformly and both its size and shape are changed.

3.2 Constitutive Modeling

The horn material was shown to have anisotropic plastic hardening from uniaxial compression tests in the longitudinal, radial, and circumferential directions. Experimental results showed that the horn material has similar mechanical properties and thus responses

in radial and circumferential directions due to the stacked structure of tubule-lamella. This similarity leads to the simplification of horn material as transversely isotropic.

In this dissertation research, a transversely isotropic constitutive model was first developed for quasi-static loading conditions (i.e., no strain-rate effect) based on the work by Li et al. (2018). The coupling of strain-rate effect in this constitutive model will be presented in the next chapter. In this work, the radial and circumferential directions are denoted as direction-1 and direction-2, respectively, and the longitudinal direction is denoted as direction-3. The 1-2 plane of the horn sheath is therefore the plane of isotropy with the following identical material properties

$$E_{11} = E_{22},\ E_{23} = E_{13},\ \nu_{32} = \nu_{31} \tag{3.25}$$

For a transversely isotropic constitutive model, the compliance matrix in Eq. (3.5) can be simplified to

$$\boldsymbol{S} = \begin{bmatrix} \frac{1}{E_{11}} & -\frac{\nu_{21}}{E_{11}} & -\frac{\nu_{31}}{E_{33}} & 0 & 0 & 0 \\ -\frac{\nu_{21}}{E_{11}} & \frac{1}{E_{22}} & -\frac{\nu_{31}}{E_{33}} & 0 & 0 & 0 \\ -\frac{\nu_{31}}{E_{33}} & -\frac{\nu_{23}}{E_{22}} & \frac{1}{E_{33}} & 0 & 0 & 0 \\ 0 & 0 & 0 & \frac{1}{E_{12}} & 0 & 0 \\ 0 & 0 & 0 & 0 & \frac{1}{E_{13}} & 0 \\ 0 & 0 & 0 & 0 & 0 & \frac{1}{E_{13}} \end{bmatrix} \tag{3.26}$$

3.2.1 Yield Function

Based on the Tagarielli-Deshpande model (Tagarielli et al., 2005), the yield function for an anisotropic material can be expressed by

$$f = \bar{\sigma} - Y = \sqrt{\boldsymbol{\sigma}^T \boldsymbol{A} \boldsymbol{\sigma}} - Y \tag{3.27}$$

where $\bar{\sigma}$ is the effective stress given by $\bar{\sigma} = \sqrt{\boldsymbol{\sigma}^T \boldsymbol{A} \boldsymbol{\sigma}}$, Y is the yield stress, and $\boldsymbol{A}$ is the anisotropic factor matrix. Tagarielli et al. gave an expression of matrix $\boldsymbol{A}$ for an anisotropic material as

$$\boldsymbol{A} = \begin{bmatrix} \left(\frac{Y_{33}}{Y_{11}}\right)^2 & -\nu_{21}\left(\frac{Y_{33}}{Y_{11}}\right)^2 & -\nu_{31}\left(\frac{Y_{33}}{Y_{11}}\right)^2 & 0 & 0 & 0 \\ & \left(\frac{Y_{33}}{Y_{22}}\right)^2 & -\nu_{31}\left(\frac{Y_{33}}{Y_{22}}\right)^2 & 0 & 0 & 0 \\ & & 1 & 0 & 0 & 0 \\ & & & \left(\frac{Y_{33}}{Y_{12}}\right)^2 & 0 & 0 \\ & \text{symmetric} & & & \left(\frac{Y_{33}}{Y_{23}}\right)^2 & 0 \\ & & & & & \left(\frac{Y_{33}}{Y_{31}}\right)^2 \end{bmatrix} \tag{3.28}$$

with the yield criterion given by

$$\sqrt{\boldsymbol{\sigma}^T \boldsymbol{A} \boldsymbol{\sigma}} - Y_{33} = 0 \tag{3.29}$$

In Eq. (3.28), Y_{ij} is the initial yield stress in direction-i (when $i = j$) or the shear flow stress on the i-j plane (when $i \neq j$). For transversely isotropic material, with direction-

1 and direction-2 forming the plane of isotropy and direction-3 as the reference principal axis, the follow stresses are related by

$$\frac{Y_{33}}{Y_{11}} = \frac{Y_{33}}{Y_{22}}, \quad \frac{Y_{33}}{Y_{23}} = \frac{Y_{33}}{Y_{31}} \tag{3.30}$$

At initial yield state, Eq. (3.30) still holds and gives

$$\frac{Y_{33}}{Y_{11}} = \frac{Y_{33}^0}{Y_{11}^0}, \quad \frac{Y_{33}}{Y_{22}} = \frac{Y_{33}^0}{Y_{22}^0}, \quad \frac{Y_{33}}{Y_{12}} = \frac{Y_{33}^0}{Y_{12}^0}, \quad \frac{Y_{33}}{Y_{23}} = \frac{Y_{33}^0}{Y_{23}^0}, \quad \frac{Y_{33}}{Y_{31}} = \frac{Y_{33}^0}{Y_{31}^0} \tag{3.31}$$

where Y_{ij}^0 is the initial flow stress, i.e., yield stress. Combining Eq. (3.30) and Eq. (3.31) gives the hardening rule of the Tagarielli-Deshpande model as

$$\frac{Y_{11}}{Y_{11}^0} = \frac{Y_{22}}{Y_{22}^0} = \frac{Y_{33}}{Y_{33}^0} = \frac{Y_{12}}{Y_{12}^0} = \frac{Y_{23}}{Y_{23}^0} = \frac{Y_{31}}{Y_{31}^0} \tag{3.32}$$

Equation (3.32) represents isotropic hardening behavior in which the yield surface expands uniformly as shown in Figure 3.3(a).

Li et al. (2018) generalized the hardening rule based on the yield function of Tagarielli-Deshpande model by introducing the concept of the hardening function, h_{ij}. The hardening functions are the ratios of the current flow stresses to the corresponding initial yield stresses given by

$$h_{ij} = \frac{Y_{ij}}{Y_{ij}^0} \tag{3.33}$$

The hardening behaviors of orthogonal material thus can be examined by comparing all six hardening functions (h_{11}, h_{22}, h_{33}, h_{12}, h_{23}, h_{13}), with isotropic hardening having the same hardening functions and anisotropic hardening having different hardening functions.

For isotropic hardening, let the hardening factors equal to h in all principal directions and principal planes as shown in Eq. (3.32). The yield function of Tagarielli-Deshpande model with direction-3 as the reference axis can then be rewritten as

$$f = \sqrt{\boldsymbol{\sigma}^T \boldsymbol{A} \boldsymbol{\sigma}} - Y_{33} = \sqrt{\boldsymbol{\sigma}^T \boldsymbol{A} \boldsymbol{\sigma}} - Y_{33}^0 h \tag{3.34}$$

and

$$\hat{f} = \frac{f}{h} = \sqrt{\boldsymbol{\sigma}^T \left(h^{-1}\boldsymbol{I}\right)^T \boldsymbol{A} \left(h^{-1}\boldsymbol{I}\right) \boldsymbol{\sigma}} - Y_{33}^0 \tag{3.35}$$

where $\boldsymbol{I}$ is a 6×6 identity matrix.

Inspired by Eq. (3.35), Li et al. (2018) defined a hardening factor matrix, $\boldsymbol{H}$, with varying hardening factors to model anisotropic hardening behaviors by modifying the stresses in the Tagarielli-Deshpande model as

$$\hat{\boldsymbol{\sigma}} = \boldsymbol{H}^{-1} \boldsymbol{\sigma} \tag{3.36}$$

where $\hat{\boldsymbol{\sigma}}$ is the modified stress and $\boldsymbol{H}$ is a diagonal matrix given as

$$\boldsymbol{H} = \begin{bmatrix} h_{11} & 0 & 0 & 0 & 0 & 0 \\ 0 & h_{22} & 0 & 0 & 0 & 0 \\ 0 & 0 & h_{33} & 0 & 0 & 0 \\ 0 & 0 & 0 & h_{12} & 0 & 0 \\ 0 & 0 & 0 & 0 & h_{23} & 0 \\ 0 & 0 & 0 & 0 & 0 & h_{13} \end{bmatrix} \tag{3.37}$$

The hardening factor matrix $\boldsymbol{H}$ serves as a tensor from the initial yield surface to the current yield surface. Similarly, the current yield surface is scaled back to the initial yield surface by the inverse of the hardening factor matrix, $\boldsymbol{H}^{-1}$, as shown by Eq. (3.36). The yield function with the modified stress, called modified yield function and denoted by $\hat{f}$, can be written as

$$\hat{f} = \hat{\sigma} - Y_{33}^0 = \sqrt{\hat{\boldsymbol{\sigma}}^T \boldsymbol{A} \hat{\boldsymbol{\sigma}}} - Y_{33}^0 = \sqrt{\boldsymbol{\sigma}^T \boldsymbol{H}^{-T} \boldsymbol{A} \boldsymbol{H}^{-1} \boldsymbol{\sigma}} - Y_{33}^0 \tag{3.38}$$

where $\hat{\sigma}$ is the modified effective stress given as

$$\hat{\sigma} = \sqrt{\boldsymbol{\sigma}^T \boldsymbol{H}^{-T} \boldsymbol{A} \boldsymbol{H}^{-1} \boldsymbol{\sigma}} \tag{3.39}$$

For clear notation, the conventional stress tensor is denoted as $\boldsymbol{\sigma}$, the conventional effective stress is denoted as $\bar{\sigma}$, the conventional plastic strain tensor is denoted as $\boldsymbol{\varepsilon_p}$, the conventional plastic strain rate is denoted as $\dot{\boldsymbol{\varepsilon}}_{\boldsymbol{p}}$, the conventional effective plastic strain is denoted as $\bar{\varepsilon}_p$, the conventional effective plastic strain rate is denoted as $\dot{\bar{\varepsilon}}_p$, the modified stress tensor is denoted as $\hat{\boldsymbol{\sigma}}$, the modified effective stress is denoted as $\hat{\sigma}$, the modified plastic strain tensor is denoted as $\hat{\boldsymbol{\varepsilon}}_{\boldsymbol{p}}$, the modified plastic strain rate is denoted as $\dot{\hat{\boldsymbol{\varepsilon}}}_{\boldsymbol{p}}$, the modified effective plastic strain is denoted as $\hat{\varepsilon}_p$, the modified effective plastic strain rate is denoted as $\dot{\hat{\varepsilon}}_p$. The symbols used in the following discussion are summarized in Table 3.1.

Table 3.1: List of symbols used for mathematical expressions of the constitutive model.

Symbol	Explanation
f	Conventional yield function
$\hat{f}$	Modified yield function
$\boldsymbol{\sigma}$	Cauchy stress
$\hat{\boldsymbol{\sigma}}$	Modified stress tensor
$\bar{\sigma}$	Conventional effective stress
$\hat{\sigma}$	Modified effective stress
$\boldsymbol{\varepsilon}_p$	Conventional plastic strain
$\hat{\boldsymbol{\varepsilon}}_p$	Modified plastic strain
$\dot{\boldsymbol{\varepsilon}}_p$	Conventional plastic strain rate
$\dot{\hat{\boldsymbol{\varepsilon}}}_p$	Modified plastic strain rate
$\bar{\varepsilon}_p$	Conventional effective plastic strain
$\hat{\varepsilon}_p$	Modified effective plastic strain
$\dot{\bar{\varepsilon}}_p$	Conventional effective plastic strain rate
$\dot{\hat{\varepsilon}}_p$	Modified effective plastic strain rate

3.2.2 Effective Plastic Strain Rate

The conventional effective plastic strain rate $\dot{\bar{\varepsilon}}_p$ is described as

$$\dot{\bar{\varepsilon}}_p = \sqrt{\dot{\boldsymbol{\varepsilon}}_{\boldsymbol{p}}^T \boldsymbol{A}^{-1} \dot{\boldsymbol{\varepsilon}}_{\boldsymbol{p}}} \tag{3.40}$$

Equation (3.40) can be proven from the conjugacy of plastic work. At time interval *dt*, the plastic work is conserved and expressed as

$$\bar{\sigma} d\bar{\varepsilon}_p = \boldsymbol{\sigma} : \boldsymbol{d\varepsilon_p} \tag{3.41}$$

which can be rewritten in the rate form as

$$\bar{\sigma}\dot{\bar{\varepsilon}}_p = \boldsymbol{\sigma} : \dot{\boldsymbol{\varepsilon}}_{\boldsymbol{p}} = \boldsymbol{\sigma}^T \dot{\boldsymbol{\varepsilon}}_{\boldsymbol{p}} = \boldsymbol{\sigma} \cdot \dot{\boldsymbol{\varepsilon}}_{\boldsymbol{p}}^T \tag{3.42}$$

or

$$\begin{aligned} \bar{\sigma} \cdot \sqrt{\dot{\boldsymbol{\varepsilon}}_{\boldsymbol{p}}^T \boldsymbol{A}^{-1} \dot{\boldsymbol{\varepsilon}}_{\boldsymbol{p}}} &= \sqrt{\boldsymbol{\sigma}^T \boldsymbol{A} \boldsymbol{\sigma} \cdot \dot{\boldsymbol{\varepsilon}}_{\boldsymbol{p}}^T \boldsymbol{A}^{-1} \dot{\boldsymbol{\varepsilon}}_{\boldsymbol{p}}} = \sqrt{\boldsymbol{\sigma}^T \boldsymbol{A} \bar{\sigma}\dot{\bar{\varepsilon}}_p \boldsymbol{A}^{-1} \dot{\boldsymbol{\varepsilon}}_{\boldsymbol{p}}} \\ &= \sqrt{\boldsymbol{\sigma}^T \bar{\sigma}\dot{\bar{\varepsilon}}_p \dot{\boldsymbol{\varepsilon}}_{\boldsymbol{p}}} = \sqrt{(\bar{\sigma}\dot{\bar{\varepsilon}}_p)^2} = \bar{\sigma}\dot{\bar{\varepsilon}}_p \end{aligned} \tag{3.43}$$

The plastic work associated with the modified stress and modified effective plastic strain rate $\dot{\hat{\varepsilon}}_p$ is given as

$$\hat{\bar{\sigma}}\dot{\hat{\bar{\varepsilon}}}_p = \hat{\boldsymbol{\sigma}}^T \dot{\hat{\boldsymbol{\varepsilon}}}_{\boldsymbol{p}} = \hat{\boldsymbol{\sigma}} \cdot \dot{\hat{\boldsymbol{\varepsilon}}}_{\boldsymbol{p}}^T = \bar{\sigma}\dot{\bar{\varepsilon}}_p = \boldsymbol{\sigma}^T \dot{\boldsymbol{\varepsilon}}_{\boldsymbol{p}} \tag{3.44}$$

or

$$\hat{\bar{\sigma}}\dot{\hat{\bar{\varepsilon}}}_p = \hat{\boldsymbol{\sigma}}^T \dot{\hat{\boldsymbol{\varepsilon}}}_{\boldsymbol{p}} = \hat{\boldsymbol{\sigma}}^T \boldsymbol{A}\boldsymbol{A}^{-1} \dot{\hat{\boldsymbol{\varepsilon}}}_{\boldsymbol{p}} = \boldsymbol{A}\hat{\boldsymbol{\sigma}} \cdot \dot{\hat{\boldsymbol{\varepsilon}}}_{\boldsymbol{p}}^T \boldsymbol{A}^{-1} \tag{3.45}$$

The multiplication of Eqs. (3.44) and (3.45) gives

$$\left(\hat{\bar{\sigma}}\dot{\hat{\bar{\varepsilon}}}_p\right)^2 = \hat{\boldsymbol{\sigma}}^T \hat{\bar{\sigma}}\dot{\hat{\bar{\varepsilon}}}_p \dot{\hat{\boldsymbol{\varepsilon}}}_{\boldsymbol{p}} = \hat{\boldsymbol{\sigma}}^T \boldsymbol{A}\hat{\boldsymbol{\sigma}} \cdot \dot{\hat{\boldsymbol{\varepsilon}}}_{\boldsymbol{p}}^T \boldsymbol{A}^{-1} \dot{\hat{\boldsymbol{\varepsilon}}}_{\boldsymbol{p}} = \hat{\bar{\sigma}}^2 \dot{\hat{\boldsymbol{\varepsilon}}}_{\boldsymbol{p}}^T \boldsymbol{A}^{-1} \dot{\hat{\boldsymbol{\varepsilon}}}_{\boldsymbol{p}} \tag{3.46}$$

and the modified plastic strain rate is obtained as

$$\dot{\hat{\bar{\varepsilon}}}_p = \sqrt{\dot{\hat{\boldsymbol{\varepsilon}}}_{\boldsymbol{p}}^T \boldsymbol{A}^{-1} \dot{\hat{\boldsymbol{\varepsilon}}}_{\boldsymbol{p}}} \tag{3.47}$$

Substitute $\hat{\boldsymbol{\sigma}} = \boldsymbol{H}^{-1}\boldsymbol{\sigma}$ into Eq. (3.45) and noted that $\boldsymbol{H}$ is a diagonal matrix, Eq. (3.45) becomes

$$\hat{\boldsymbol{\sigma}}^T \dot{\hat{\boldsymbol{\varepsilon}}}_{\boldsymbol{p}} = \left(\boldsymbol{H}^{-1}\boldsymbol{\sigma}\right)^T \dot{\hat{\boldsymbol{\varepsilon}}}_{\boldsymbol{p}} = \boldsymbol{\sigma}^T \boldsymbol{H}^{-T} \dot{\hat{\boldsymbol{\varepsilon}}}_{\boldsymbol{p}} = \boldsymbol{\sigma}^T \boldsymbol{H}^{-1} \dot{\hat{\boldsymbol{\varepsilon}}}_{\boldsymbol{p}} = \boldsymbol{\sigma}^T \dot{\boldsymbol{\varepsilon}}_{\boldsymbol{p}} \tag{3.48}$$

then the modified plastic strain rate is related to the conventional plastic strain rate by

$$\dot{\hat{\boldsymbol{\varepsilon}}}_{\boldsymbol{p}} = \boldsymbol{H}\dot{\boldsymbol{\varepsilon}}_{\boldsymbol{p}} \tag{3.49}$$

Substituting Eq. (3.49) into Eq. (3.47), the modified effective plastic strain rate can be expressed in terms of the conventional plastic strain rate and is given as

$$\dot{\hat{\varepsilon}}_p = \sqrt{\dot{\boldsymbol{\varepsilon}}_{\boldsymbol{p}}^T \boldsymbol{H}^T \boldsymbol{A}^{-1} \boldsymbol{H}\dot{\boldsymbol{\varepsilon}}_{\boldsymbol{p}}} \tag{3.50}$$

3.2.3 Plastic Flow

The plastic flow rate with conventional plastic strain rate, $\dot{\boldsymbol{\varepsilon}}_{\boldsymbol{p}}$, and anisotropic hardening yield function, $\hat{f}$, can be described with the associated flow theory as

$$\dot{\boldsymbol{\varepsilon}}_{\boldsymbol{p}} = \dot{\lambda}\frac{\dfrac{\partial \hat{f}}{\partial \boldsymbol{\sigma}}}{\left|\dfrac{\partial \hat{f}}{\partial \boldsymbol{\sigma}}\right|} \tag{3.51}$$

where $\dot{\lambda}$ is the flow rate coefficient and can be represented by yield state variables as follows.

Substitute Eq. (3.51) into Eq. (3.50), the modified effective plastic strain rate $\dot{\hat{\varepsilon}}_p$ becomes

$$\dot{\hat{\varepsilon}}_p = \dot{\lambda}\frac{\sqrt{\left(\dfrac{\partial \hat{f}}{\partial \boldsymbol{\sigma}}\right)^T \boldsymbol{H}^T \boldsymbol{A}^{-1} \boldsymbol{H}\left(\dfrac{\partial \hat{f}}{\partial \boldsymbol{\sigma}}\right)}}{\left|\dfrac{\partial \hat{f}}{\partial \boldsymbol{\sigma}}\right|} \tag{3.52}$$

With Eq. (3.36), the derivative of the anisotropic hardening yield function ($\hat{f} = \sqrt{\boldsymbol{\sigma}^T \boldsymbol{H}^{-T} \boldsymbol{A} \boldsymbol{H}^{-1} \boldsymbol{\sigma}} - Y_{33}^0$) with respect to stress $\boldsymbol{\sigma}$ is obtained as

$$\frac{\partial \hat{f}}{\partial \boldsymbol{\sigma}} = \frac{\boldsymbol{H}^{-T}\boldsymbol{A}\boldsymbol{H}^{-1}\boldsymbol{\sigma}}{\hat{\sigma}} \tag{3.53}$$

Noted that $\boldsymbol{H}$ is a diagonal matrix (i.e., $\boldsymbol{H}^{-T} = \boldsymbol{H}^{-1}$) and $\boldsymbol{A}$ is a symmetric matrix (i.e., $\boldsymbol{A} = \boldsymbol{A}^{T}$). Eq. (3.52) can be simplified by substituting Eq. (3.53),

$$\begin{aligned}
\dot{\hat{\varepsilon}}_p &= \dot{\lambda}\frac{\sqrt{\left(\frac{\boldsymbol{H}^{-T}\boldsymbol{A}\boldsymbol{H}^{-1}\boldsymbol{\sigma}}{\hat{\sigma}}\right)^{T}\boldsymbol{H}^{T}\boldsymbol{A}^{-1}\boldsymbol{H}\left(\frac{\boldsymbol{H}^{-T}\boldsymbol{A}\boldsymbol{H}^{-1}\boldsymbol{\sigma}}{\hat{\sigma}}\right)}}{\left|\frac{\partial \hat{f}}{\partial \boldsymbol{\sigma}}\right|} \\
&= \dot{\lambda}\frac{\sqrt{\left(\boldsymbol{\sigma}^{T}\boldsymbol{H}^{-T}\boldsymbol{A}^{T}\boldsymbol{H}^{-1}\right)\boldsymbol{H}^{T}\boldsymbol{A}^{-1}\boldsymbol{H}\left(\boldsymbol{H}^{-T}\boldsymbol{A}\boldsymbol{H}^{-1}\boldsymbol{\sigma}\right)}}{\left|\frac{\partial \hat{f}}{\partial \boldsymbol{\sigma}}\right|\hat{\sigma}} \\
&= \dot{\lambda}\frac{\sqrt{\boldsymbol{\sigma}^{T}\boldsymbol{H}^{-T}\boldsymbol{A}\boldsymbol{H}^{-1}\boldsymbol{H}\boldsymbol{A}^{-1}\boldsymbol{H}\boldsymbol{H}^{-1}\boldsymbol{A}\boldsymbol{H}^{-1}\boldsymbol{\sigma}}}{\left|\frac{\partial \hat{f}}{\partial \boldsymbol{\sigma}}\right|\hat{\sigma}} \\
&= \dot{\lambda}\frac{\sqrt{\boldsymbol{\sigma}^{T}\boldsymbol{H}^{-T}\boldsymbol{A}\boldsymbol{H}^{-1}\boldsymbol{\sigma}}}{\left|\frac{\partial \hat{f}}{\partial \boldsymbol{\sigma}}\right|\hat{\sigma}} \\
&= \frac{\dot{\lambda}}{\left|\frac{\partial \hat{f}}{\partial \boldsymbol{\sigma}}\right|}
\end{aligned} \tag{3.54}$$

The flow rate coefficient $\dot{\lambda}$ can be obtained from Eq. (3.54), and substituting $\dot{\lambda}$ into Eq. (3.51) gives the plastic strain rate as

$$\dot{\boldsymbol{\varepsilon}}_{\boldsymbol{p}} = \dot{\hat{\varepsilon}}_p \frac{\partial \hat{f}}{\partial \boldsymbol{\sigma}} \tag{3.55}$$

3.2.4 Strain Decomposition

The total strain increment, $d\boldsymbol{\varepsilon}$, can be decomposed into two parts: the elastic strain increment, $d\boldsymbol{\varepsilon}_e$, and the plastic strain increment, $d\boldsymbol{\varepsilon}_p$, as shown below.

$$d\boldsymbol{\varepsilon} = d\boldsymbol{\varepsilon}_e + d\boldsymbol{\varepsilon}_p \tag{3.56}$$

The elastic strain increment is used for stress update given by

$$d\boldsymbol{\sigma} = \boldsymbol{C} d\boldsymbol{\varepsilon}_e = \boldsymbol{C}\left(d\boldsymbol{\varepsilon} - d\boldsymbol{\varepsilon}_p\right) \tag{3.57}$$

In most finite element programs, the total strain increment, $d\boldsymbol{\varepsilon}$, is automatically calculated; therefore, the major work in Eq. (3.57) is to determine the plastic strain increment. From Eq. (3.55), the plastic strain increment $d\boldsymbol{\varepsilon}_p$ over a single timestep can be rewritten as

$$d\boldsymbol{\varepsilon}_p = d\hat{\varepsilon}_p \frac{\partial \hat{f}}{\partial \boldsymbol{\sigma}} \tag{3.58}$$

3.2.5 Consistency Condition

The consistency condition of the flow plasticity theory ($d\hat{f} = 0$) can be elaborated as

$$d\hat{f} = \frac{\partial \hat{f}}{\partial \hat{\boldsymbol{\sigma}}} : d\hat{\boldsymbol{\sigma}} = 0 \tag{3.59}$$

where $d\hat{\boldsymbol{\sigma}}$ is the modified stress increment and can be obtained from the modified stress ($\hat{\boldsymbol{\sigma}} = \boldsymbol{H}^{-1}\boldsymbol{\sigma}$) as

$$d\hat{\boldsymbol{\sigma}} = d\left(\boldsymbol{H}^{-1}\boldsymbol{\sigma}\right) = d\left(\boldsymbol{H}^{-1}\right)\boldsymbol{\sigma} + \boldsymbol{H}^{-1} d\boldsymbol{\sigma} \tag{3.60}$$

The consistency condition is then rewritten as

$$\frac{\partial \hat{f}}{\partial \hat{\boldsymbol{\sigma}}} : \left[d\left(\boldsymbol{H}^{-1}\right)\boldsymbol{\sigma} + \boldsymbol{H}^{-1} d\boldsymbol{\sigma} \right] = 0 \tag{3.61}$$

3.2.6 Evolution of Modified Effective Plastic Strain

Since the inverse of anisotropic hardening factor matrix, $\boldsymbol{H}^{-1}$, is diagonal, its increment can be written as

$$d\left(\boldsymbol{H}^{-1}\right) = -\boldsymbol{H}^{-1}\boldsymbol{H}^{-1}\frac{\partial \boldsymbol{H}}{\partial \bar{\varepsilon}_p} d\bar{\varepsilon}_p \tag{3.62}$$

Substituting the conventional plastic strain rate, $\dot{\boldsymbol{\varepsilon}}_{\boldsymbol{p}}$, from Eq. (3.55) into Eq. (3.40), the conventional effective plastic strain rate, $\dot{\bar{\varepsilon}}_p$, is obtained as

$$\dot{\bar{\varepsilon}}_p = \dot{\hat{\varepsilon}}_p \sqrt{\left(\frac{\partial \hat{f}}{\partial \boldsymbol{\sigma}}\right)^T \boldsymbol{A}^{-1} \left(\frac{\partial \hat{f}}{\partial \boldsymbol{\sigma}}\right)} \tag{3.63}$$

From Eq. (3.63), the increment of conventional effective plastic strain over a small timestep can be written as

$$d\bar{\varepsilon}_p = d\hat{\varepsilon}_p \sqrt{\left(\frac{\partial \hat{f}}{\partial \boldsymbol{\sigma}}\right)^T \boldsymbol{A}^{-1} \left(\frac{\partial \hat{f}}{\partial \boldsymbol{\sigma}}\right)} \tag{3.64}$$

By substituting $d\bar{\varepsilon}_p$ from Eq. (3.64) into Eq. (3.62) to get $d\left(\boldsymbol{H}^{-1}\right)$, substituting $d\boldsymbol{\varepsilon_p}$ from Eq. (3.58) into Eq. (3.57) to get the stress increment $d\boldsymbol{\sigma}$, and substituting both $d\left(\boldsymbol{H}^{-1}\right)$ and $d\boldsymbol{\sigma}$ into the consistency condition in Eq. (3.61), the modified effective plastic strain increment $d\hat{\varepsilon}_p$ is obtained and given as

$$d\hat{\varepsilon}_p = \frac{\dfrac{\partial \hat{f}}{\partial \hat{\boldsymbol{\sigma}}} : \boldsymbol{H}^{-1}\boldsymbol{C}d\boldsymbol{\varepsilon}}{\dfrac{\partial \hat{f}}{\partial \hat{\boldsymbol{\sigma}}} : \boldsymbol{H}^{-1}\boldsymbol{H}^{-1}\dfrac{\partial \boldsymbol{H}}{\partial \bar{\varepsilon}_p}\sqrt{\left(\dfrac{\partial \hat{f}}{\partial \boldsymbol{\sigma}}\right)^T \boldsymbol{A}^{-1}\left(\dfrac{\partial \hat{f}}{\partial \boldsymbol{\sigma}}\right)}\boldsymbol{\sigma} + \dfrac{\partial \hat{f}}{\partial \hat{\boldsymbol{\sigma}}} : \boldsymbol{H}^{-1}\boldsymbol{C}\dfrac{\partial \hat{f}}{\partial \boldsymbol{\sigma}}} \tag{3.65}$$

In Eq. (3.65), the stiffness matrix ***C***, anisotropic factor matrix ***A***, and anisotropic hardening factor matrix ***H*** can be determined using material properties from experimental data. The total strain increment $d\boldsymbol{\varepsilon}$ will be automatically calculated by the finite element program at each iteration after the initial timestep. The derivatives of the anisotropic hardening yield function $\hat{f}$ with respect to the modified stress $\hat{\boldsymbol{\sigma}}$ and to the stress $\boldsymbol{\sigma}$ are given as

$$\frac{\partial \hat{f}}{\partial \hat{\boldsymbol{\sigma}}} = \frac{\boldsymbol{A}\hat{\boldsymbol{\sigma}}}{\hat{\sigma}} \tag{3.66}$$

$$\frac{\partial \hat{f}}{\partial \boldsymbol{\sigma}} = \frac{\boldsymbol{H}^{-T}\boldsymbol{A}\boldsymbol{H}^{-1}\boldsymbol{\sigma}}{\hat{\sigma}} \tag{3.67}$$

With Eqs. (3.66) and (3.67), the modified effective plastic strain increment $d\hat{\varepsilon}_p$ in every timestep can be calculated and then substituted into Eq. (3.58) to obtain plastic strain increment $d\boldsymbol{\varepsilon_p}$. The plastic strain increment $d\boldsymbol{\varepsilon_p}$ along with total strain increment $d\boldsymbol{\varepsilon}$ are then used to calculate the stress update in Eq. (3.57).

3.4 Model Implementation

To implement the constitutive model discussed in Section 3.3 into a finite element program such as LS-Dyna, a user-defined material subroutine (UMAT) needs to be developed and linked to the main program. The explicit method was used to calculate updated stress state from the previous stress state.

In LS-Dyna, the following variables in each element are provided to the UMAT by the main program along with the current timestep *dt*:

(1) σ_1, σ_2, σ_3, σ_4, σ_5, σ_6: six stress components on local coordinates in previous timestep;

(2) $d\varepsilon_1$, $d\varepsilon_2$, $d\varepsilon_3$, $d\varepsilon_4$, $d\varepsilon_5$, $d\varepsilon_6$: the increments of six strain components on local coordinates;

(3) $\bar{\varepsilon}_p$: effective plastic strain in previous timestep;

The following variables were defined to assist in updating the stress values in the constitutive model of the UMAT:

(1) h_{11}, h_{22}, h_{33}, h_{12}, h_{23}, h_{13}: six hardening functions;

(2) $h'_{11}, h'_{22}, h'_{33}, h'_{12}, h'_{23}, h'_{13}$: the derivatives of hardening functions with respect to the effective plastic strain;

(3) A_{11}, A_{12}, A_{13}, A_{22}, A_{23}, A_{33}, A_{44}, A_{55}, A_{66}: nine constants in anisotropic factor matrix;

(4) B_{11}, B_{12}, B_{13}, B_{22}, B_{23}, B_{33}, B_{44}, B_{55}, B_{66}: non-zero entries for the upper triangle of the inverse anisotropic factor matrix;

(5) C_{11}, C_{12}, C_{13}, C_{22}, C_{23}, C_{33}, C_{44}, C_{55}, C_{66}: nine constants in the stiffness matrix;

(6) f'_1, f'_2, f'_3, f'_4, f'_5, f'_6: six derivatives of the yield function with respect to the stress;

(7) $\hat{f}'_1$, $\hat{f}'_2$, $\hat{f}'_3$, $\hat{f}'_4$, $\hat{f}'_5$, $\hat{f}'_6$: six derivatives of the yield function with respect to the modified stress;

From Eq. (3.38), the yield function $\hat{f}$ is checked at every timestep to determine if the material has plastic deformation using the modified effective stress, $\bar{\sigma}$, calculated as follows.

$$\hat{\sigma} = \sqrt{\frac{A_{11}\sigma_1^2}{h_{11}^2} + \frac{A_{22}\sigma_2^2}{h_{22}^2} + \frac{A_{33}\sigma_3^2}{h_{33}^2} + \frac{A_{44}\sigma_4^2}{h_{12}^2} + \frac{A_{55}\sigma_5^2}{h_{23}^2} + \frac{A_{66}\sigma_6^2}{h_{13}^2} + \frac{2A_{12}\sigma_1\sigma_2}{h_{11}h_{22}} + \frac{2A_{13}\sigma_1\sigma_3}{h_{11}h_{33}} + \frac{2A_{23}\sigma_2\sigma_3}{h_{22}h_{33}}} \tag{3.68}$$

If $\hat{f} < 0$, the material is still undergoing elastic deformation and the elastic strain increments used for stress update in Eq. (3.57) are exactly the total strain increments given as $d\varepsilon_1$, $d\varepsilon_2$, $d\varepsilon_3$, $d\varepsilon_4$, $d\varepsilon_5$, $d\varepsilon_6$ in the current state. The strain increments are calculated by LS-Dyna and the stress increments at the current timestep are determined by

$$\begin{aligned} d\sigma_1 &= C_{11}d\varepsilon_1 + C_{12}d\varepsilon_2 + C_{13}d\varepsilon_3 \\ d\sigma_2 &= C_{12}d\varepsilon_1 + C_{22}d\varepsilon_2 + C_{23}d\varepsilon_3 \\ d\sigma_3 &= C_{13}d\varepsilon_1 + C_{23}d\varepsilon_2 + C_{33}d\varepsilon_3 \\ d\sigma_4 &= C_{44}d\varepsilon_4 \\ d\sigma_5 &= C_{55}d\varepsilon_5 \\ d\sigma_6 &= C_{66}d\varepsilon_6 \end{aligned} \tag{3.69}$$

With Euler explicit method, the new stresses at the current timestep are updated as

$$\begin{aligned} \sigma_1 &= \sigma_1 + d\sigma_1 \\ \sigma_2 &= \sigma_2 + d\sigma_2 \\ \sigma_3 &= \sigma_3 + d\sigma_3 \\ \sigma_4 &= \sigma_4 + d\sigma_4 \\ \sigma_5 &= \sigma_5 + d\sigma_5 \\ \sigma_6 &= \sigma_6 + d\sigma_6 \end{aligned} \tag{3.70}$$

The updated stresses will be stored and used for checking yield in the next timestep. When $\hat{f} \geq 0$, the material reaches yield point and then undergoes plastic deformation. The plastic flow rates are needed to determine the evolution of plastic deformation that are given with respect to the stress as

$$
\begin{aligned}
f_1' &= \frac{1}{\hat{\sigma}}\left(\frac{A_{11}\sigma_1}{h_{11}^2}+\frac{A_{12}\sigma_2}{h_{11}h_{22}}+\frac{A_{13}\sigma_3}{h_{11}h_{33}}\right)\\
f_2' &= \frac{1}{\hat{\sigma}}\left(\frac{A_{22}\sigma_2}{h_{22}^2}+\frac{A_{12}\sigma_1}{h_{11}h_{22}}+\frac{A_{23}\sigma_3}{h_{22}h_{33}}\right)\\
f_3' &= \frac{1}{\hat{\sigma}}\left(\frac{A_{33}\sigma_3}{h_{33}^2}+\frac{A_{13}\sigma_1}{h_{11}h_{33}}+\frac{A_{23}\sigma_2}{h_{22}h_{33}}\right)\\
f_4' &= \frac{A_{44}\sigma_4}{\hat{\sigma}h_{12}^2}\\
f_5' &= \frac{A_{55}\sigma_5}{\hat{\sigma}h_{23}^2}\\
f_6' &= \frac{A_{66}\sigma_6}{\hat{\sigma}h_{13}^2}
\end{aligned}
\tag{3.71}
$$

and with respect to the modified stress as

$$
\begin{aligned}
\hat{f}_1' &= \frac{1}{\hat{\sigma}}\left(\frac{A_{11}\sigma_1}{h_{11}}+\frac{A_{12}\sigma_2}{h_{22}}+\frac{A_{13}\sigma_3}{h_{33}}\right)\\
\hat{f}_2' &= \frac{1}{\hat{\sigma}}\left(\frac{A_{12}\sigma_1}{h_{11}}+\frac{A_{22}\sigma_2}{h_{22}}+\frac{A_{23}\sigma_3}{h_{33}}\right)\\
\hat{f}_3' &= \frac{1}{\hat{\sigma}}\left(\frac{A_{13}\sigma_1}{h_{11}}+\frac{A_{23}\sigma_2}{h_{22}}+\frac{A_{33}\sigma_3}{h_{33}}\right)\\
\hat{f}_4' &= \frac{A_{44}\sigma_4}{\hat{\sigma}h_{12}}\\
\hat{f}_5' &= \frac{A_{55}\sigma_5}{\hat{\sigma}h_{23}}\\
\hat{f}_6' &= \frac{A_{66}\sigma_6}{\hat{\sigma}h_{13}}
\end{aligned}
\tag{3.72}
$$

Substituting Eqs. (3.71) and (3.72) into Eq. (3.65), the modified effective plastic strain increment $d\hat{\varepsilon}_p$ can be calculated as

$$d\hat{\varepsilon}_p = \frac{\Pi_1}{\Pi_2 + \Pi_3 \cdot \Pi_4} \tag{3.73}$$

where

$$\Pi_1 = \frac{\hat{f}_1'}{h_{11}}\left(C_{11}d\varepsilon_1 + C_{12}d\varepsilon_2 + C_{13}d\varepsilon_3\right) + \frac{\hat{f}_2'}{h_{22}}\left(C_{12}d\varepsilon_1 + C_{22}d\varepsilon_2 + C_{23}d\varepsilon_3\right)$$
$$+ \frac{\hat{f}_3'}{h_{33}}\left(C_{13}d\varepsilon_1 + C_{23}d\varepsilon_2 + C_{33}d\varepsilon_3\right) + \frac{\hat{f}_4'C_{44}d\varepsilon_4}{h_{12}} + \frac{\hat{f}_5'C_{55}d\varepsilon_5}{h_{23}} + \frac{\hat{f}_6'C_{66}d\varepsilon_6}{h_{13}}$$

$$\Pi_2 = \frac{\hat{f}_1'}{h_{11}}\left(C_{11}f_1' + C_{12}f_2' + C_{13}f_3'\right) + \frac{\hat{f}_2'}{h_{22}}\left(C_{12}f_1' + C_{22}f_2' + C_{23}f_3'\right)$$
$$+ \frac{\hat{f}_3'}{h_{33}}\left(C_{13}f_1' + C_{23}f_2' + C_{33}f_3'\right) + \frac{\hat{f}_4'f_4'C_{44}}{h_{12}} + \frac{\hat{f}_5'f_5'C_{55}}{h_{23}} + \frac{\hat{f}_6'f_6'C_{66}}{h_{13}}$$

$$\Pi_3 = \frac{\hat{f}_1'h_{11}'\sigma_1}{h_{11}^2} + \frac{\hat{f}_2'h_{22}'\sigma_2}{h_{22}^2} + \frac{\hat{f}_3'h_{33}'\sigma_3}{h_{33}^2} + \frac{\hat{f}_4'h_{12}'\sigma_4}{h_{12}^2} + \frac{\hat{f}_5'h_{23}'\sigma_5}{h_{23}^2} + \frac{\hat{f}_6'h_{13}'\sigma_6}{h_{13}^2}$$

$$\Pi_4 = \sqrt{\begin{aligned} &f_1'\left(B_{11}f_1' + B_{12}f_2' + B_{13}f_3'\right) + f_2'\left(B_{12}f_1' + B_{22}f_2' + B_{23}f_3'\right) \\ &+ f_3'\left(B_{13}f_1' + B_{23}f_2' + B_{33}f_3'\right) + B_{44}f_4'^2 + B_{55}f_5'^2 + B_{66}f_6'^2 \end{aligned}}$$

Finally, the plastic strain increment at the current timestep can be determined by substituting $d\hat{\varepsilon}_p$ from Eq. (3.73) into Eq. (3.58). The stress increments are then substituted into Eq. (3.70) to update the current stresses due to plastic hardening.

The above procedures and calculations were implemented in Fortran and integrated into LS-Dyna through the "usermat" package, an interface package for users-defined material subroutines. The UMAT for the anisotropic hardening constitutive model was written into the Fortran file "dyn21umats.f" file that was compiled and linked to the LS-Dyna program. Certain modifications were made in the original Makefile from the "usermat" package:

(1) Three additional libraries need to be loaded: libscalapack.a, liblapack.a, and libblas.a;

(2) The local path of math kernel library needs to be identified.

Using the modified Makefile, the modules of mpp-dyna/12.0.0, and Intel Fortran complier 2020, a massively parallel processing version of LS-Dyna R12.0.0 with the UMAT was created for high-performance computing clusters. Detailed instructions of compiling the UMAT and linking to the LS-Dyna program are provided in Appendix A.

3.5 Material Characterization

To obtain the parameters of the anisotropic hardening constitutive model, material characterization was conducted using available experimental data of the horn under loading along the principal axes (Huang et al. 2017 and Tombolato et al. 2010).

3.5.1 Mechanical Response in the Radial Direction under Quasi-static Loading

The stress-strain curve under quasi-static compression was retrieved from the study of Huang et al. (2017). In their test, an air-dried horn was cut into 4×4×4 mm^3 cubic sample. The uniaxial compression test was conducted using Instron 3367 testing system with a strain rate of 10^{-3}/s. More than three samples were tested in the radial direction and the average values were reported. The engineering strains and engineering stresses from the original data were converted to true strains and true stresses using the following equations.

$$\varepsilon_{true} = \ln\left(1+\varepsilon_{eng}\right) \tag{3.74}$$

$$\sigma_{true} = \sigma_{eng}\left(1+\varepsilon_{eng}\right) \tag{3.75}$$

The true stress-strain curve under quasi-static uniaxial compression test in the radial direction (direction-1) was plotted in Figure 3.4.

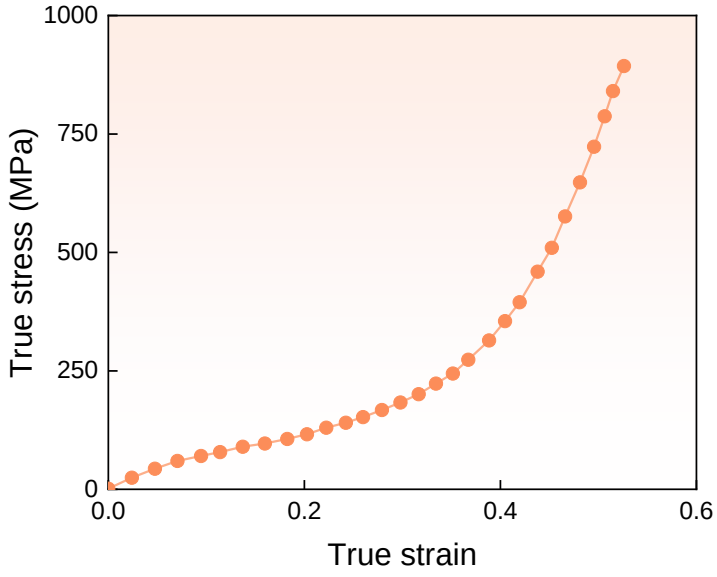

Figure 3.4: Stress-strain curve of the horn material from the quasi-static compression test in the radial direction.

Figure 3.4 shows that the horn material deforms elastically until it yields at a strain of 0.06, then undergoes plastic hardening. An intersection method using tangent lines was applied on the true stress-strain curve to obtain the mathematical expression of its stress response and to determine the Young's modulus, initial yield strength, and hardening function of horn material in the radial direction (Pouriayevali et al. 2013). As shown in Figure 3.5, two tangent lines were drawn on the stress-strain curve. For the elastic region, a tangent line was drawn by connecting the origin and the first data point with a strain of 0.024 and a stress of 24.2 MPa, giving the Young's modulus for the radial direction as $E_{11}^{(q)} = 1.007$ GPa. The second tangent line, which was taken at the point with a strain of 0.160 and a stress of 96.6 MPa, gave the modulus of the plateau region of plastic deformation. The intersection point of these two tangent lines was chosen as the initial

yield point with a yield strength of $Y_{11}^{0(q)} = 60.3$ MPa. The shaded area in Figure 3.5 gives the region of plastic deformation with hardening, starting from the initial yield point.

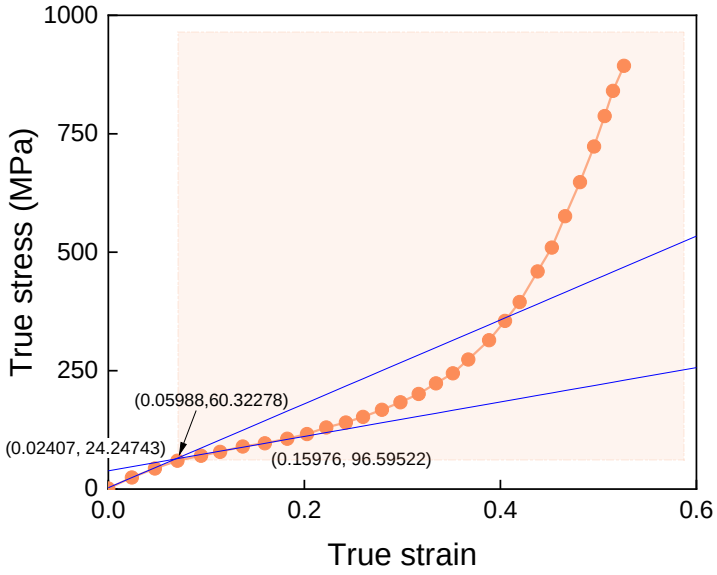

Figure 3.5: Material characterization of the horn material under quasi-static compression in the radial direction.

The hardening factor h_{11} in radial direction was calculated based on Eq. (3.33) with respect to the effective plastic strain. The relationship between h_{11} and the effective plastic strain was shown in Figure 3.6.

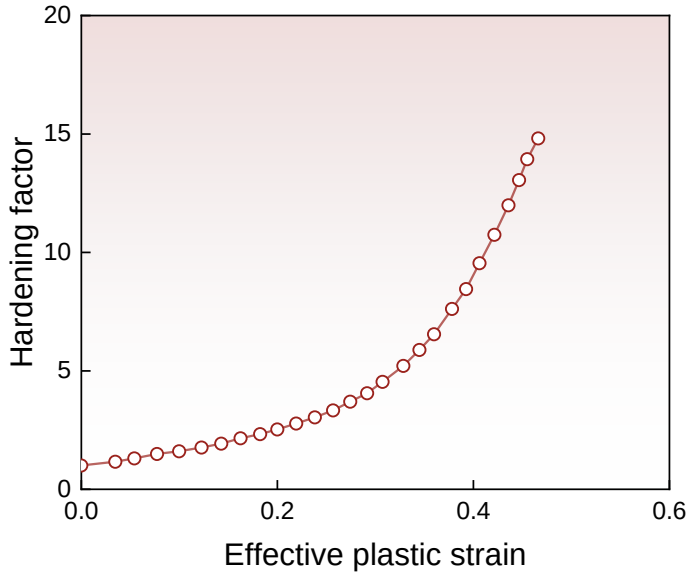

Figure 3.6: Hardening factor in the radial direction under quasi-static compression.

A fourth-order polynomial was used to fit the hardening factor data in Figure 3.6. The polynomial function is given in Eq. (3.76) and it has an adjusted coefficient of multiple determination (R^2_{adj}) of 0.99967. The derivative of the polynomial function is provided in Eq. (3.77) that was used in the mathematical calculations in the UMAT.

$$h_{11} = 1 + 5.13783\bar{\varepsilon}_p + 21.18819\bar{\varepsilon}_p^2 - 138.29079\bar{\varepsilon}_p^3 + 446.14202\bar{\varepsilon}_p^4 \tag{3.76}$$

$$h'_{11} = 5.13783 + 42.37638\bar{\varepsilon}_p - 414.87237\bar{\varepsilon}_p^2 + 1787.56808\bar{\varepsilon}_p^3 \tag{3.77}$$

As previously discussed, the horn material can be considered as transversely isotropic material, i.e., the mechanical properties in the radial direction (direction-1) and circumferential direction (direction-2) are similar. Therefore, the material properties in the circumferential direction were taken from those in the radial direction in the UMAT.

3.5.2 Mechanical Response in the Longitudinal Direction under Quasi-static Loading

Figure 3.7 shows the true stress-strain curve of the horn material under quasi-static uniaxial compression in the longitudinal direction (direction-3) with a strain rate of 10^{-3}/s. The true stress-strain curve was converted from the engineering stress-strain curve obtained from the test.

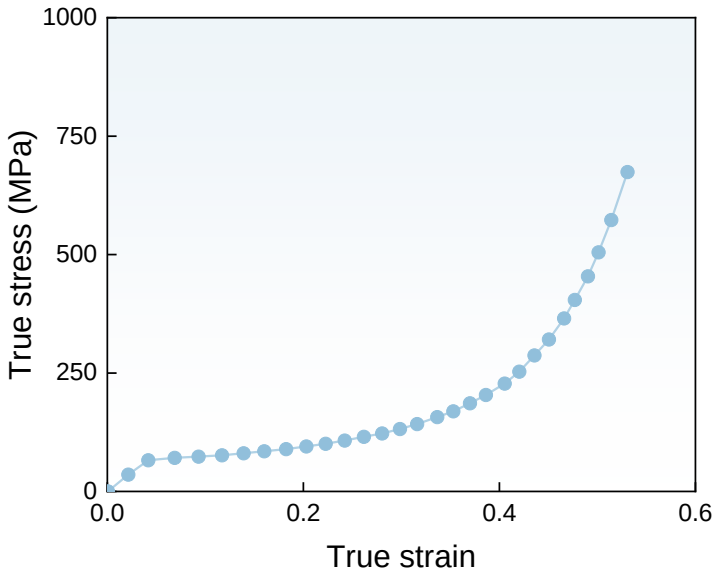

Figure 3.7: True stress-strain curve of the horn material under quasi-static compression in the longitudinal direction.

It can be seen from Figure 3.7 that a clear linear elastic region exists with the initial yielding stress of 70 MPa occurred at 4% of strain. After the initial yielding point, the material undergoes densification without significant hardening, as shown by the plateau

region between 4% and 20% of strain. After 20% of strain, the material deforms with significant plastic hardening as the increase of plastic strains.

Figure 3.8 shows material characterization of the horn under quasi-static compression in the longitudinal direction. The tangent line in the elastic region was drawn by connecting the origin and the first data point with a strain of 0.021 and a stress of 35.3 MPa, giving the Young's modulus for the longitudinal direction as $E_{33}^{(q)} = 1.643$ GPa. The second tangent line gave the modulus of the plateau region of plastic deformation, and it was taken at the point with a strain of 0.093 and a stress of 73.4 MPa. The intersection point of these two tangent lines was chosen as the initial yield point for the longitudinal direction with a yield strength of $Y_{33}^{0(d)} = 67.8$ MPa. The region of plastic deformation with hardening starting from initial yield point was shown by the shaded area in Figure 3.8.

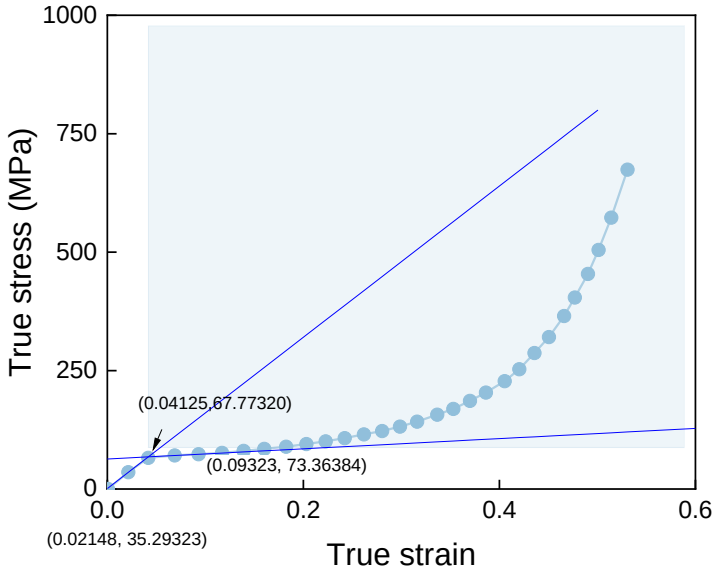

Figure 3.8: Material characterization of the horn in longitudinal direction under quasi-static compression.

The hardening factor h_{33} for quasi-static compression in the longitudinal direction is calculated and shown in Figure 3.9. Using a fifth-order polynomial, the hardening factor function h_{33} was obtained, as given in Eq. (3.78), and has an adjusted coefficient of multiple determination (R_{adj}^2) of 0.99996. The derivative of the polynomial function is given in Eq. (3.79).

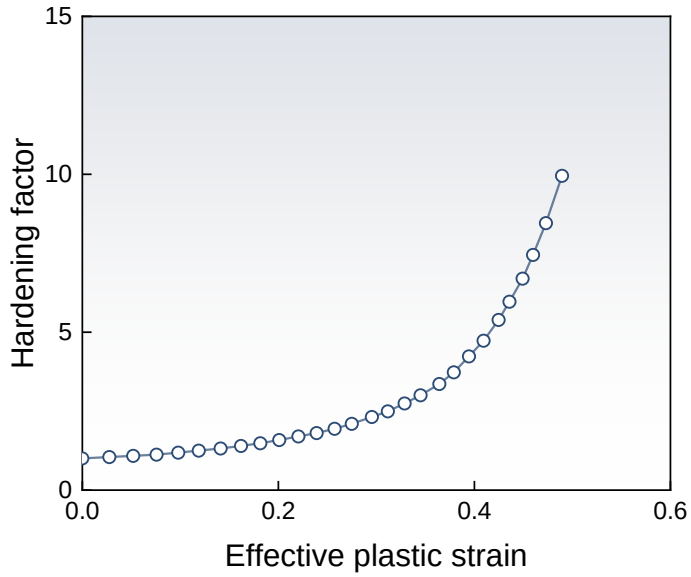

Figure 3.9: Hardening factor in the longitudinal direction under quasi-static compression.

$$h_{33} = 1 + 2.83387\bar{\varepsilon}_p - 34.98844\bar{\varepsilon}_p^2 + 345.88854\bar{\varepsilon}_p^3 - 1134.65913\bar{\varepsilon}_p^4 + 1441.30631\bar{\varepsilon}_p^5 \quad (3.78)$$

$$h'_{33} = 2.83387 - 69.97688\bar{\varepsilon}_p + 1037.66562\bar{\varepsilon}_p^2 - 4538.63652\bar{\varepsilon}_p^3 + 7206.53155\bar{\varepsilon}_p^4 \quad (3.79)$$

3.5.3 Shear Responses under Quasi-static Loading

The shear stress-strain curve of the horn material was obtained from the study of Tombolato et al. (2010), as shown in Figure 3.10. The shear stresses were much lower than the normal stresses from the compression tests in the radial and longitudinal directions. Due to extremely limited experimental data of horn materials under shear loading, the shear stress-strain curve shown in Figure 3.10 were adopted as the material properties for all three planes formed by the principal axes.

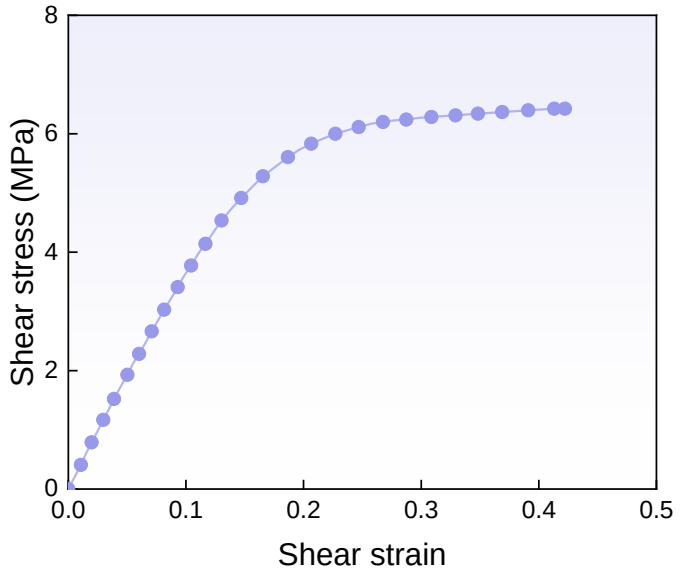

Figure 3.10: Stress strain curve from the quasi-static shear loading of the horn material.

Figure 3.11 shows material characterization of the horn material under quasi-static shear loading. A tangent line was drawn by connecting the origin and the data point with a strain of 0.050 and a shear stress of 1.9 MPa. This gives a shear modulus of 0.037 GPa in the elastic region. The initial yield point was determined and the yield strength was 3.4

MPa. The plastic deformation phase was marked by the shaded area in Figure 3.11 for calculating the associated hardening factor.

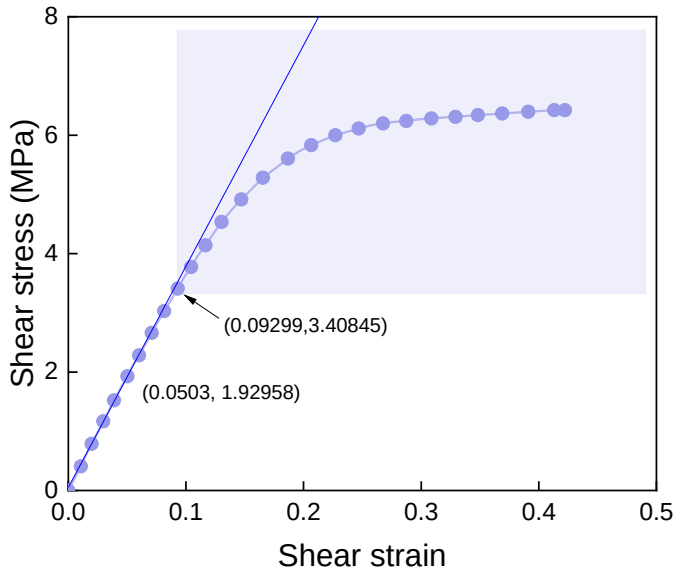

Figure 3.11: Material characterization of the horn sheath under quasi-static shear loading.

A fourth-order polynomial was used to fit the hardening factor data as shown in Figure 3.12. The polynomial function is given in Eq. (3.80) and it has an adjusted coefficient of multiple determination (R_{adj}^2) of 0.9998. The derivative of the polynomial function is given in Eq. (3.81).

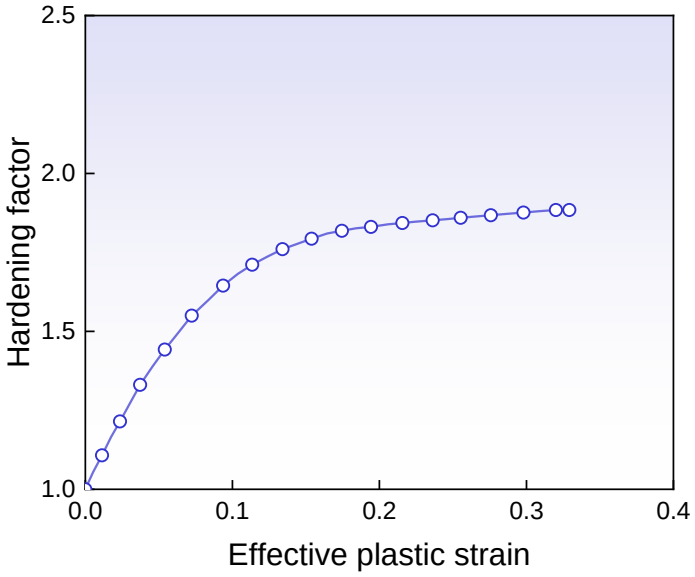

Figure 3.12: Hardening factor under quasi-static shear loading.

$$h_s = 1 + 10.48626\bar{\varepsilon}_p - 46.71161\bar{\varepsilon}_p^2 + 85.93777\bar{\varepsilon}_p^3 - 48.05504\bar{\varepsilon}_p^4 \quad (3.80)$$

$$h_s' = 10.48626 - 93.42322\bar{\varepsilon}_p + 257.81331\bar{\varepsilon}_p^2 - 192.22016\bar{\varepsilon}_p^3 \quad (3.81)$$

3.6 Model Validation

The user-defined material model was first validated before it was adopted in the simulation of the horn under dynamic impact loading. The validation was conducted by comparing the stresses from simulation results to the experimental data from the quasi-static compression test. In the experiment, a 4×4×4 mm^3 sample was compressed at a strain rate of 10^{-3}/s by two rigid plates in an Instron 3367 system. An FE model of the horn sample, as shown in Figure 3.13, was developed to simulate the experiment of quasi-static compression in the radial direction.

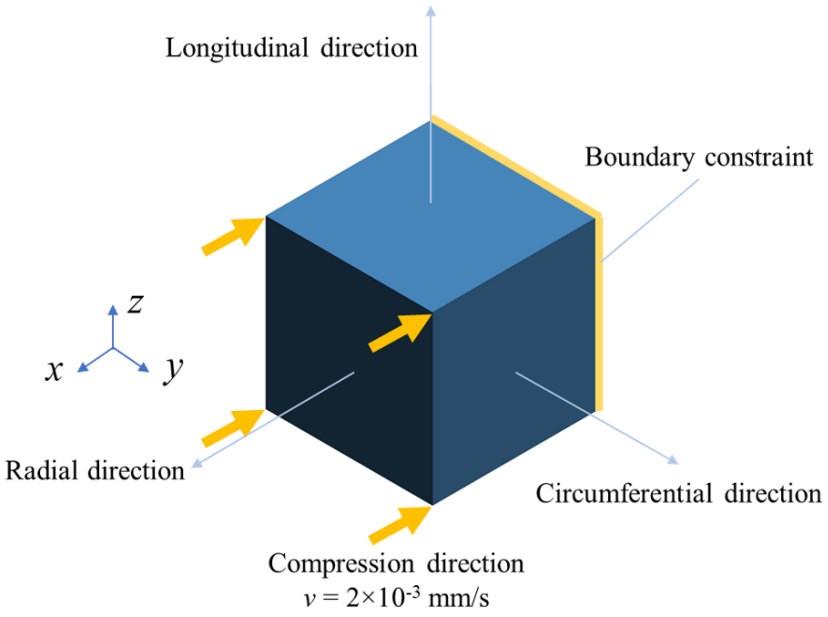

Figure 3.13: FE model of the horn sample for validation under quasi-static compression in the radial direction.

The FE model consisted of a single constant stress hexahedron element with the same size as the cubic horn sample. The element's local principal directions were defined by material axes, i.e., radial, circumferential, and longitudinal directions that were also aligned with the global coordinate system (i.e., the global *x*, *y*, and *z* directions). The four nodes on the front surface were assigned a prescribed velocity of 2×10^{-3} mm/s pointing to the negative axis of the radial direction. This prescribed velocity was to compress the element at a strain rate 10^{-3}/s that was later confirmed by the simulation results. The total simulation time was 1,500 seconds, which resulted in 52% of true strain on the element. To prevent numerical instability and reduce noises at the beginning of the compression when the velocity was applied, the prescribed velocity was introduced by a ramp signal as

shown in Figure 3.14 within the first 0.1 mm of compression distance giving a t_{ramp} of 100 s.

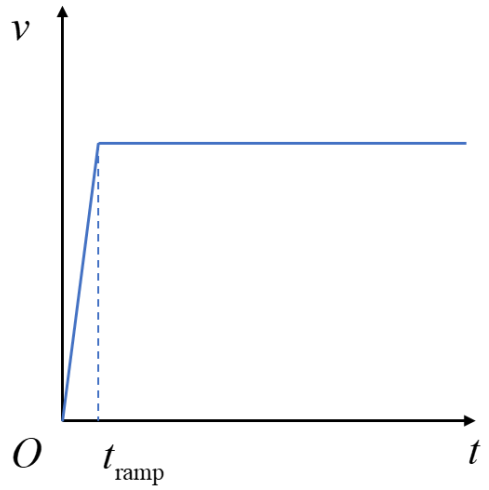

Figure 3.14: Ramp signal for prescribed velocity.

The four nodes on the back surface of the element as highlighted in gold color in Figure 3.13 were fixed by constraining all three degrees of freedom (translational displacements in *x*, *y*, and *z* directions). The transversely isotropic constitutive model with anisotropic hardening was applied to the material definition in the FE model through keyword MAT-USER-DEFINED-MATERIAL-MODELS. No mass scaling was used in the validation model for higher simulation fidelity; this resulted in an averaged timestep of 10^{-6} s.

Figure 3.15 shows the comparison of stress-strain curves from simulation results and the quasi-static compression test in the radial direction. The simulation results predicted a linear elastic deformation until the material reached 6% strain and then entered the plastic hardening phase. It can be seen that the simulation results agreed well with the experimental data. Three instants of the deformed element from the FE simulation were

also shown in Figure 3.15. It can be concluded that the numerical model of the horn material, specifically the constitutive model, can accurately predict the stress responses for both elastic and plastic deformations under quasi-static compression in the radial direction.

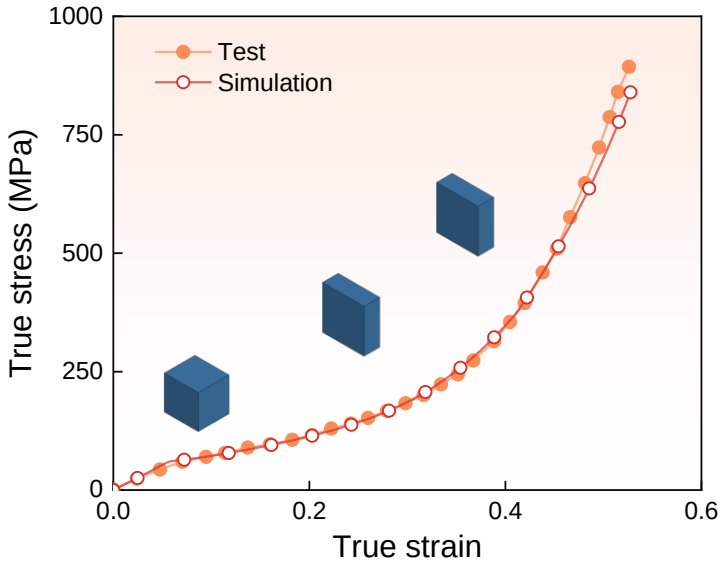

Figure 3.15: Comparison of stress-strain curves from simulation results and test data for the quasi-static compression of the horn material in the radial direction.

Another FE model of the horn sample was developed to simulate the experiment of quasi-static compression in the longitudinal direction as shown in Figure 3.16. The same type of constant-strain hexahedron element was used for the cubic horn sample. Its local principal directions were aligned with the global coordinate system as well. The four nodes on the top surface were assigned a prescribed velocity of 2×10^{-3} mm/s pointing to the negative axis of the longitudinal direction, compressing the element at a strain rate 10^{-3}/s confirmed by simulation results. The same as in FE model for compression in the radial direction, the total simulation time of compression in the longitudinal direction was 1,500

seconds resulting in 52% of true strain on the element. The same ramp signal for prescribed velocity was used to prevent numerical instability and reduce noises. All three degrees of freedom of the four nodes on the bottom surface of the element as highlighted in gold color in Figure 3.16 were completely constrained.

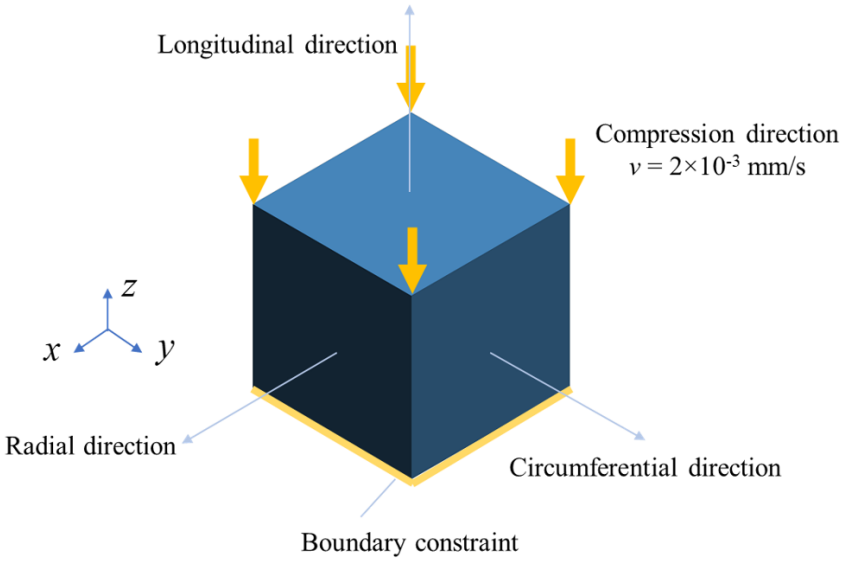

Figure 3.16: FE model of horn sample for validation under quasi-static compression in the longitudinal direction.

Figure 3.17 shows the comparisons of stress-strain curves from simulation results and the quasi-static compression test in the longitudinal direction. The simulation results also predicted a linear elastic deformation in the longitudinal direction until the material reached 4% of strain and then entered plateau between 4% and 20% of strain for densification but without significant hardening. With further increase of the strain, the material exhibited significant plastic hardening as shown on the stress strain curve. It can be seen that the simulation results agreed well with the experimental data. Three instants of the deformed element from the FE simulation were also shown in Figure 3.17. It can be

concluded that the numerical model of the horn material, specifically the constitutive model, can accurately predict the stress responses for both elastic and plastic deformations under quasi-static compression in the longitudinal direction.

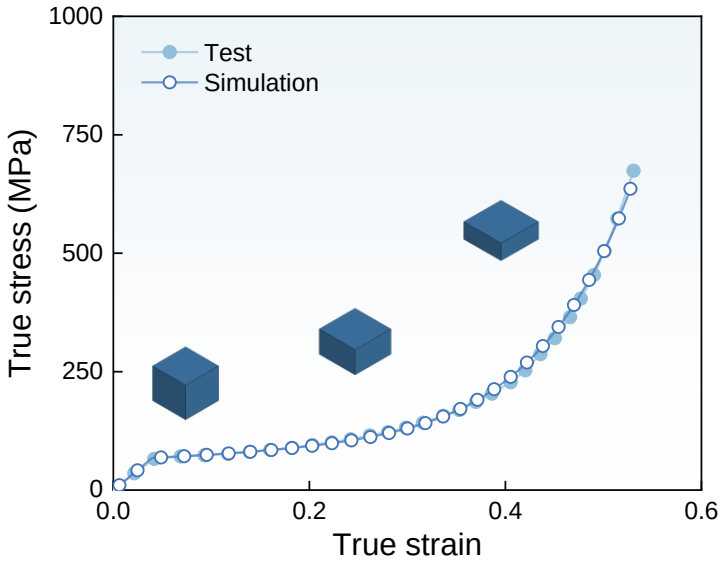

Figure 3.17: Comparison of stress-strain curves from simulation results and test data for the quasi-static compression of the horn material in the longitudinal direction.

The above comparisons indicated that the constitutive model could accurately predict the stress responses of the horn sheath material under quasi-static compressions in both radial and longitudinal directions. In the situation of two bighorn sheep ramming, the maximum impact velocity could reach 5.5 m/s that may cause a strain rate as high as 10^3/s. In the next chapter, the strain-rate effect of the horn material will be discussed using dynamic compression tests. A refined constitutive model that was coupled with strain-rate effect will be developed and implemented into LS-Dyna as a user-defined material.

CHAPTER 4: STRAIN-RATE EFFECT OF THE HORN MATERIAL

It is estimated that the impact speed between two bighorn sheep during ramming can reach 5.5 m/s, which may cause the horn to have a strain rate of 10^3/s. To accurately simulate the dynamic impact between two horns, strain-rate effects of the horn material should be considered in the constitutive models. In this chapter, the stress-strain responses of the horn material under dynamic tests were analyzed for coupling the strain-rate effect with the anisotropic hardening constitutive model that was initially designed for quasi-static loading conditions. The constitutive model with strain-rate effect was then validated against the dynamic test data. The coupled constitutive model could be used to predict the mechanical behaviors of the horn material under dynamic loading with strain rates ranging from 10^{-3}/s to 10^3/s.

4.1 Dynamic Tests

The dynamic test data of the horn material were obtained from the work by Huang et al. (2017). The dynamic impact tests were conducted on a Hopkinson bar system with modifications to the original setting to accommodate the lower impedance of the horn material. Instead of using metal material that may affect the constancy of strain rate and uniformity of stresses over the test sample, rods made of woven glass/epoxy composites were used as the striking bar, incident bar and transmission bar. A total of three samples were tested for each loading condition and the averaged results were reported.

Figure 4.1 shows the stress-strain curves of dynamic impact test of the horn samples in the radial direction at a strain-rate level of 10^3/s, along with that of the quasi-static comparison test with a strain rate of 10^{-3}/s. Figure 4.1 clearly shows the strain-rate effect from the increased stress values of the dynamic test compared to those of the quasi-static test at the same strain levels. It is also shown in Figure 4.1 that the Young's modulus in radial direction from the dynamic test is estimated to be three times larger than that from the quasi-static test, along with the increased initial yield strength.

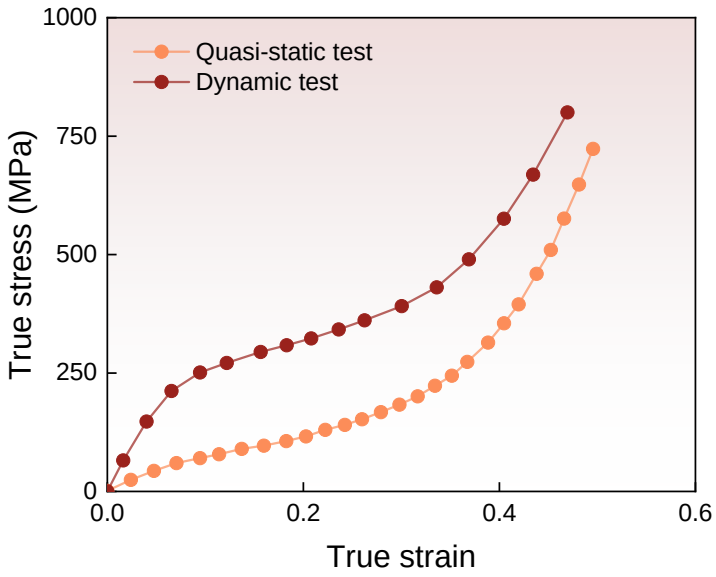

Figure 4.1: Stress-strain curves of the horn material from the dynamic impact test and quasi-static compression test in the radial direction.

Figure 4.2 shows the material characterization of the horn material under dynamic impact loading in the radial direction with a strain rate of 10^3/s. For the elastic region, a tangent line was drawn by connecting the origin and the first data point with a strain of 0.016 and a stress of 65.5 MPa, giving the Young's modulus for the radial direction as

$E_{11}^{(d)} = 3.740$ GPa. The second tangent line, which was taken at the point with a strain of 0.208 and a stress of 322.7 MPa, gave the modulus of the plateau region of plastic deformation. The intersection point of these two tangent lines was chosen as the initial yield point with a yield strength of $Y_{11}^{0(d)} = 230.2$ MPa. The shaded area in Figure 4.2 gives the region of plastic deformation with hardening, starting from initial yield point.

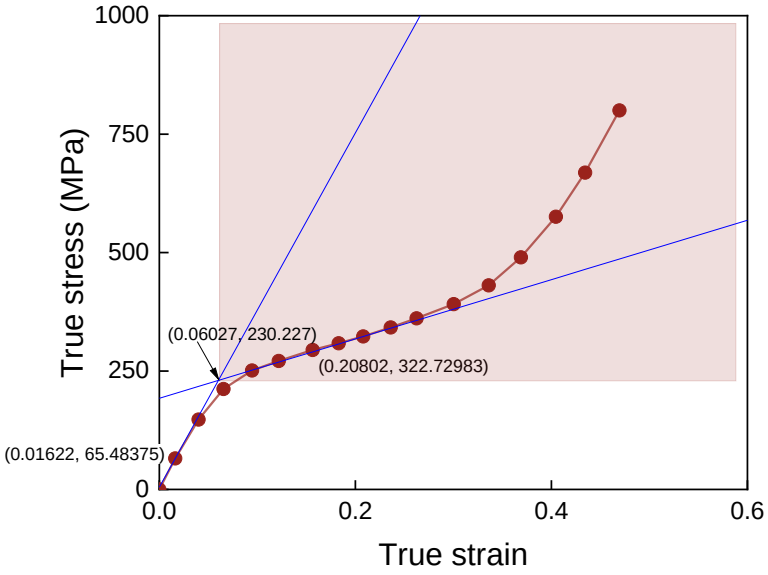

Figure 4.2: Determination of material properties of the horn under dynamic impact loading in the radial direction.

The hardening factor for the dynamic compression test in the radial direction was calculated and shown in Figure 4.3. It was observed that the hardening factor in the dynamic test was lower than that in the quasi-static test. A fourth-order polynomial was used to fit the hardening factor data. The polynomial function is given in Eq. (4.1) and it

has an adjusted coefficient of multiple determination (R^2_{adj}) of 0.99995. The derivative of the polynomial function is given in Eq. (4.2) and will be used in the constitutive model.

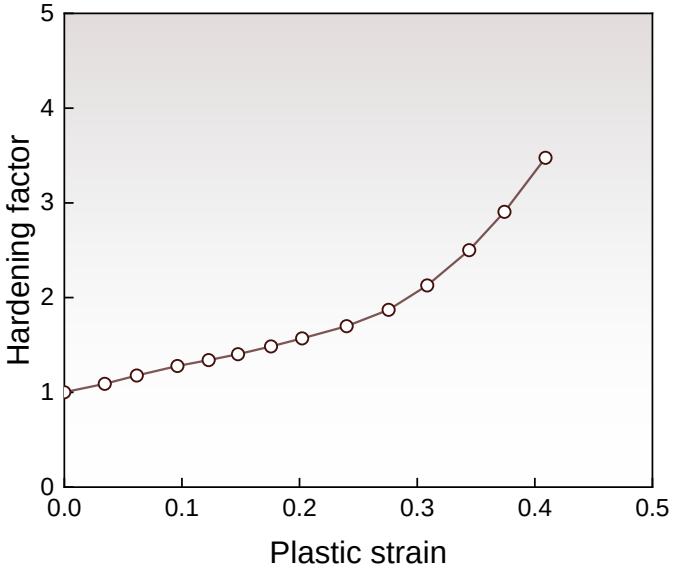

Figure 4.3: Hardening factor in the radial direction under dynamic impact loading.

$$h_{11}^{(d)} = 1 + 3.18877\bar{\varepsilon}_p - 3.30006\bar{\varepsilon}_p^2 - 13.46988\bar{\varepsilon}_p^3 + 94.80184\bar{\varepsilon}_p^4 \tag{4.1}$$

$$h_{11}'^{(d)} = 3.18877 - 6.60012\bar{\varepsilon}_p - 40.40964\bar{\varepsilon}_p^2 + 379.20736\bar{\varepsilon}_p^3 \tag{4.2}$$

The dynamic compression test of the horn material in the circumferential direction showed similar responses as the radial direction, an indication of transversely isotropic material property. For the longitudinal direction, the stress-strain curve from the dynamic compression test is shown in Figure 4.4, along with that from the quasi-static test. It can be seen from Figure 4.4 that the yield strength of the horn sheath in the longitudinal direction under dynamic loads was approximately three times of that under quasi-static loads. The scaling factor of the yield strength from quasi-static (10^{-3}/s) to high strain rate (10^{3}/s) was

similar as in dynamic test in radial direction. It was also observed from the dynamic test that there was a clear plateau region in plastic deformation with almost no hardening that extended to 40% strain, as shown in Figure 4.4.

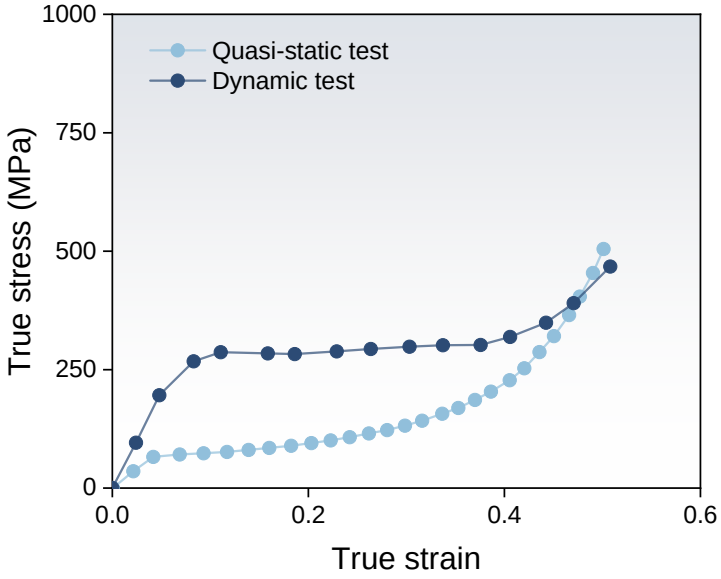

Figure 4.4: Stress strain curves from the dynamic and quasi-static compression tests of the horn material in the longitudinal direction.

Material characterization of the horn under dynamic impact loading in the longitudinal direction with a strain rate of 10^3/s was shown in Figure 4.5. For the elastic region, a tangent line was drawn by connecting the origin and the first data point with a strain of 0.024 and a stress of 95.6 MPa, giving the Young's modulus for the longitudinal direction as $E_{33}^{(d)} = 4.084$ GPa. The second tangent line, which was taken at the point with a strain of 0.186 and a stress of 282.6 MPa, gave the modulus of the plateau region of plastic deformation. The intersection point of these two tangent lines was chosen as the initial yield point for longitudinal direction with a yield strength of $Y_{33}^{0(d)} = 277.6$ MPa.

The region of plastic deformation with hardening starting from initial yield point was highlighted as shaded area in Figure 4.5.

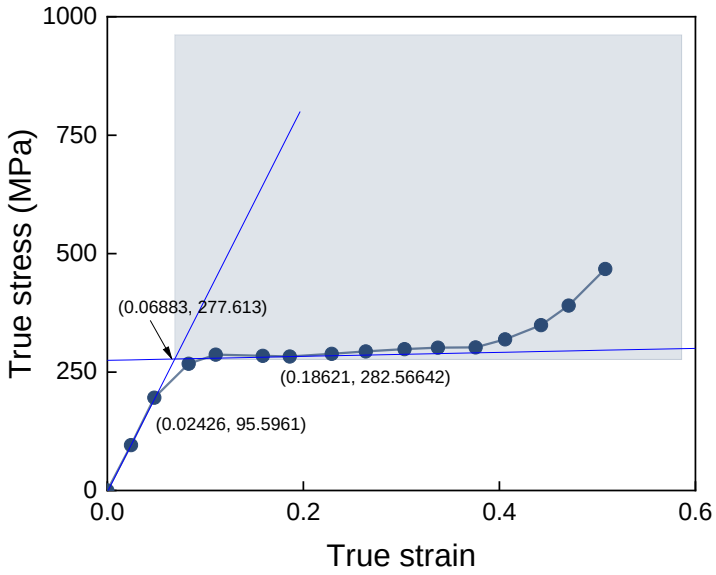

Figure 4.5: Material characterization of the horn under dynamic compression in longitudinal direction.

The hardening factor for the dynamic compression test in the longitudinal direction was calculated and shown in Figure 4.6. A fifth-order polynomial was used to fit the hardening factor data. The polynomial function is given in Eq. (4.3) and it has an adjusted coefficient of multiple determination (R^2_{adj}) of 0.99988. The derivative of the polynomial function is given in Eq. (4.4).

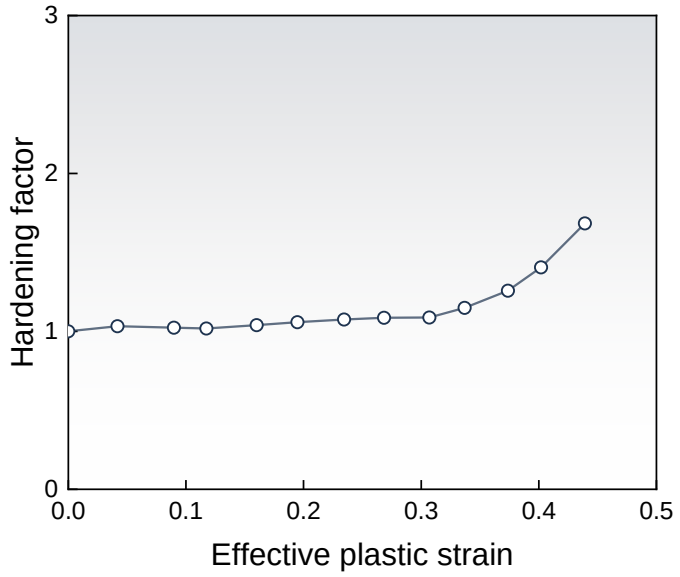

Figure 4.6: Hardening factor in longitudinal direction under dynamic compression.

$$h_{33}^{(d)} = 1 + 0.68528\bar{\varepsilon}_p - 8.65678\bar{\varepsilon}_p^2 + 66.11459\bar{\varepsilon}_p^3 - 227.47015\bar{\varepsilon}_p^4 + 301.1215\bar{\varepsilon}_p^5 \quad (4.3)$$

$$h_{33}'^{(d)} = 0.68528 - 17.31356\bar{\varepsilon}_p + 198.34377\bar{\varepsilon}_p^2 - 909.8806\bar{\varepsilon}_p^3 + 1505.6075\bar{\varepsilon}_p^4 \quad (4.4)$$

4.2 Coupling of Strain-rate Effect in the Constitutive Model

To couple strain-rate effects into the existing constitutive model, a direct interpolation from quasi-static state to dynamic state based on strain rate levels was applied for variables such as Young's moduli, yield strengths, and hardening factors. Due to very limited dynamic test data of horn materials with strain rates between 10^{-3}/s and 10^{3}/s, a linear interpolation was adopted to determine the variables for strain rates between these extrema. The loading case with the highest strain rate (10^{3}/s) was used for model validation.

4.2.1 Young's Modulus in the Radial Direction

Under quasi-static state with a strain rate of 10^{-3}/s, the Young's modulus of the horn material in the radial direction was determined to be 1.007 GPa. For the dynamic test with a strain rate of 10^{3}/s, the Young's modulus was determined to be 3.740 GPa. To obtain the Young's modulus at any strain rate between 10^{-3} /s and 10^{3}/s, the following interpolation function was adopted:

$$E_{11}(\dot{\varepsilon}) = \left(1 + 2.71225 \cdot \frac{\dot{\varepsilon}}{10^{3}}\right) E_{11}^{(q)} \tag{4.5}$$

where $E_{11}^{(q)}$ is the Young's modulus in radial direction under quasi-static loading and $E_{11}(\dot{\varepsilon})$ is the interpolated Young's modulus in radial direction at a strain rate $\dot{\varepsilon}$.

4.2.2 Young's Modulus in the Longitudinal Direction

Under quasi-static state with strain rate of 10^{-3}/s, the Young's modulus of the horn material in the longitudinal direction was determined to be 1.643 GPa. For the dynamic test with strain rate of 10^{3}/s, the Young's modulus was determined to be 4.084 GPa. To obtain the Young's modulus at any strain rate between 10^{-3}/s and 10^{3}/s, the following interpolation function was adopted:

$$E_{33}(\dot{\varepsilon}) = \left(1 + 1.48589 \cdot \frac{\dot{\varepsilon}}{10^{3}}\right) E_{33}^{(q)} \tag{4.6}$$

where $E_{33}^{(q)}$ is the Young's modulus in longitudinal direction under quasi-static loading and $E_{33}(\dot{\varepsilon})$ is the interpolated Young's modulus in longitudinal direction at a strain rate $\dot{\varepsilon}$.

4.2.3 Yield Strength in the Radial Direction

Under quasi-static state with a strain rate of 10^{-3}/s, the initial yield strength of the horn material in the radial direction was determined to be 60.3 MPa. For the dynamic test with a strain rate of 10^{3}/s, the initial yield strength was determined to be 230.2 MPa. To obtain the yield strength at any strain rate between 10^{-3}/s and 10^{3}/s, the following interpolation function was adopted:

$$Y_{11}^{0}(\dot{\varepsilon}) = \left(1 + 2.81657 \cdot \frac{\dot{\varepsilon}}{10^{3}}\right) Y_{11}^{0(q)} \tag{4.7}$$

where $Y_{11}^{0(q)}$ is the initial yield strength in the radial direction under quasi-static loading and $Y_{11}^{0}(\dot{\varepsilon})$ is the interpolated yield strength in the radial direction at a strain rate $\dot{\varepsilon}$.

4.2.4 Yield Strength in the Longitudinal Direction

Under quasi-static state with a strain rate of 10^{-3}/s, the initial yield strength of the horn material in the longitudinal direction was determined to be 67.8 MPa. For the dynamic test with a strain rate of 10^{3}/s, the initial yield strength was determined to be 277.6 MPa. To obtain the yield strength at any strain rate between 10^{-3}/s and 10^{3}/s, the following interpolation function was adopted:

$$Y_{33}^{0}(\dot{\varepsilon}) = \left(1 + 3.09622 \cdot \frac{\dot{\varepsilon}}{10^{3}}\right) Y_{33}^{0(q)} \tag{4.8}$$

where $Y_{33}^{0(q)}$ is the initial yield strength in the longitudinal direction under quasi-static loading and $Y_{33}^{0}(\dot{\varepsilon})$ is the interpolated yield strength in the longitudinal direction at a strain rate $\dot{\varepsilon}$.

4.2.5 Hardening Factor in the Radial Direction

The hardening factor was also interpolated using the quasi-static and dynamic test data for any strain rate between 10^{-3}/s and 10^{3}/s. It should be noted that the hardening factor is always equal to 1 when effective plastic strain is zero at the initial yield state regardless of strain rate level. With plastic hardening, the hardening factor increases from 1 with the increase of effective plastic strain. The interpolation function $h_{11}(\dot{\varepsilon})$ of the hardening factor in the radial direction is given as

$$h_{11}(\dot{\varepsilon}) = 1 + \left[1 + (\varphi_r - 1)\frac{\dot{\varepsilon}}{10^3}\right] \cdot \left(h_{11}^{(q)} - 1\right) \tag{4.9}$$

where $h_{11}^{(q)}$ is the hardening factor of the horn material in the radial direction under quasi-static loading condition, and φ_r is a scaling factor determined by the strain rates of the quasi-static and dynamic tests.

Figure 4.7 shows the scaling factor φ_r that was determined by comparing the hardening functions for the quasi-static and dynamic loading conditions.

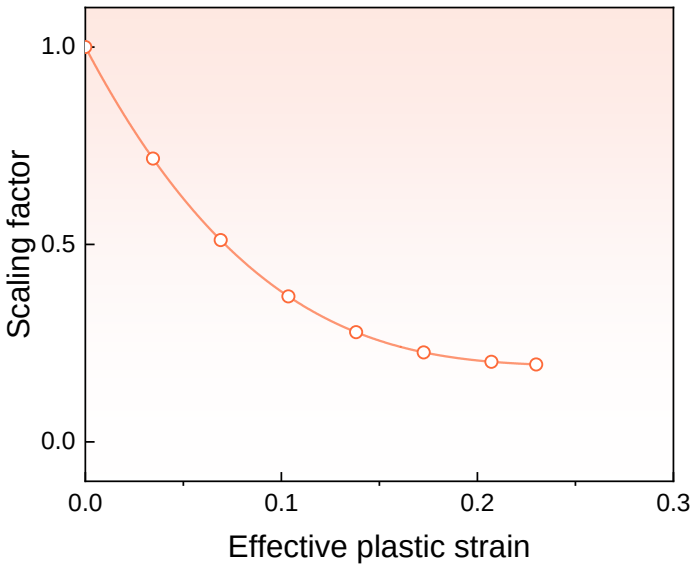

Figure 4.7: The scaling factor for the hardening function from quasi-static to dynamic loading conditions in the radial direction.

A third order polynomial was adopted to calculate the scaling factor using the effective plastic strain. The polynomial model had an adjusted coefficient of multiple determination (R_{adj}^2) of 0.99912 and is given as

$$\varphi_r = 1 - 9.41017\bar{\varepsilon}_p + 37.10269\bar{\varepsilon}_p^2 - 49.52212\bar{\varepsilon}_p^3 \tag{4.10}$$

4.2.6 Hardening Factor in the Longitudinal Direction

The interpolation function $h_{33}(\dot{\varepsilon})$ of the hardening factor in the longitudinal direction is given as

$$h_{33}(\dot{\varepsilon}) = 1 + \left[1 + (\varphi_l - 1)\frac{\dot{\varepsilon}}{10^3}\right] \cdot \left(h_{33}^{(q)} - 1\right) \tag{4.11}$$

where $h_{33}^{(q)}$ is the hardening factor of the horn material in the longitudinal direction under quasi-static loading condition, and φ_l is a scaling factor determined by the strain rates of the quasi-static and dynamic tests.

Figure 4.8 shows the scaling factor φ_l that was determined by comparing the hardening functions for the quasi-static and dynamic loading conditions.

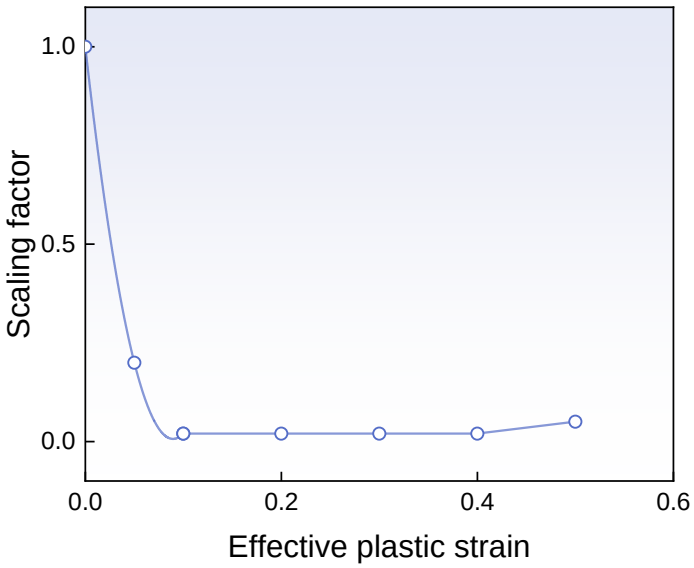

Figure 4.8: Scaling factor from quasi-static loading to dynamic loading in longitudinal direction for hardening factor.

A piecewise mathematical model was adopted to calculate the scaling factor using the effective plastic strain as given in Eq. (4.12).

$$\varphi_l = \begin{cases} 1 - 22.2\bar{\varepsilon}_p + 124\bar{\varepsilon}_p^2 & \bar{\varepsilon}_p \le 0.1 \\ 0.02 & 0.1 < \bar{\varepsilon}_p \le 0.4 \\ 0.3\bar{\varepsilon}_p - 0.1 & \bar{\varepsilon}_p > 0.4 \end{cases} \tag{4.12}$$

4.3 Model Validation

After coupling strain-rate effects into the preciously developed user-defined material model, a new executable LS-Dyna program was re-compiled. To validate the new user-defined material model that was implemented in LS-Dyna, a single-element FE model for the horn material was developed for dynamic loading with a strain rate of 10^3/s. The validation model for dynamic loading was similar to the one used in the quasi-static loading case. Figure 4.9 shows the FE model under dynamic compression in the radial direction.

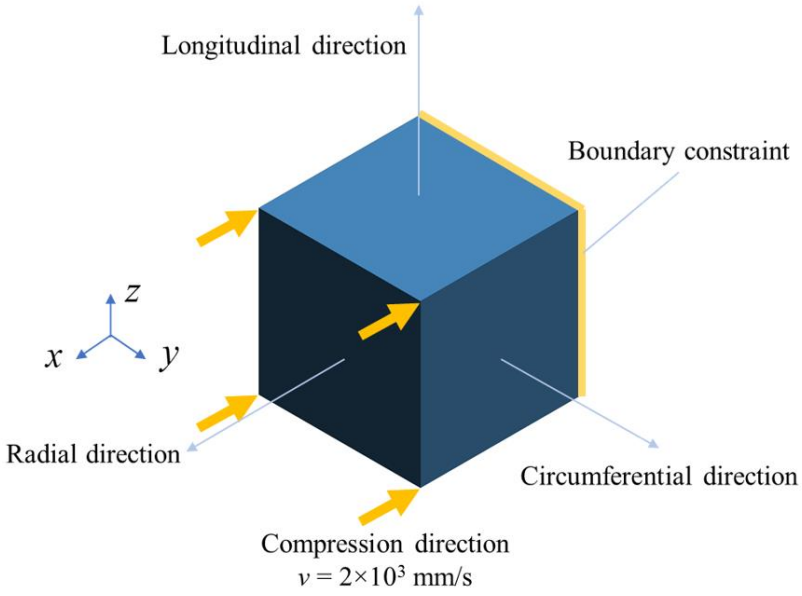

Figure 4.9: FE model of the horn sample for validation under dynamic compression in the radial direction.

This model was created by the same single hexahedron element as that in the quasi-static validation model. The element had a size of 4 mm in each dimension, same as the cubic horn sample used in the test. The local principal directions of the element were

aligned with the axes of global coordinate system (*x*, *y*, and *z* directions) and were parallel to the material axes (radial, circumferential, and longitudinal directions). The boundary conditions were the same as those in the quasi-static case, with four nodes on the back surface completely fixed for all three degrees of freedom, as highlighted in gold color in Figure 4.9. The four nodes on the front surface were assigned a prescribed velocity of 2×10^3 mm/s pointing to the negative axis of the radial direction. This prescribed velocity was to compress the element at a strain rate 10^3/s that was later confirmed by the simulation results. The total simulation time was 1.5 ms, which resulted in 52% of true strain on the element. The prescribed velocity was introduced by the ramp signal with a t_{ramp} of 0.1 ms.

Figure 4.10 shows the comparison of stress-strain curves from simulation results and the compression test in the radial direction. The simulation results matched well with test data except for the distinct transition at initial yield point of the curve from simulation, which was due to the simplification in model characterization as discussed in Section 4.1. The smooth transition seen from test results was replaced by the intersection of two tangent lines that were used to determine the initial yield strength. Nevertheless, the constitutive model captured extremely well the plastic hardening of the horn material that was the main focus of this research. The simulation results showed the successful implementation of strain-rate effect in the constitutive model, which was capable of predicting the material responses in both elastic and plastic regions.

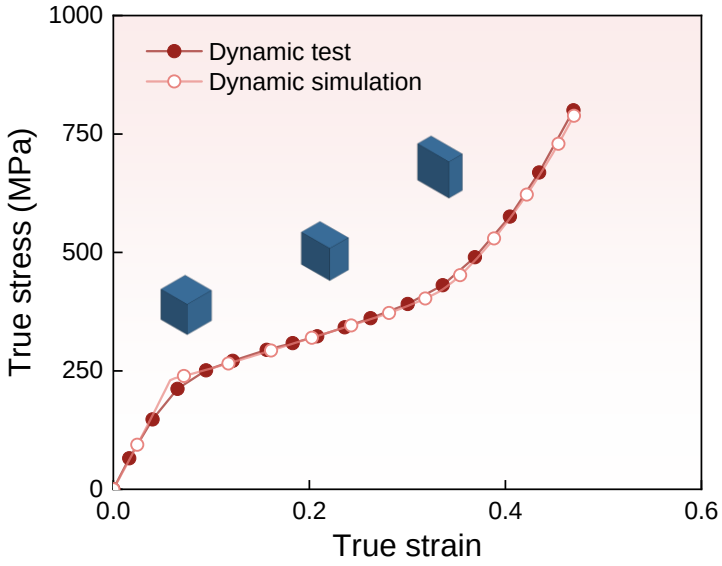

Figure 4.10: Comparison of stress-strain curves from simulation results and test data for the dynamic compression of the horn material in the radial direction.

For the longitudinal direction, Figure 4.11 shows the corresponding validation model for dynamic loading conditions. The prescribed velocity of 2×10^{3} mm/s was applied to the top four nodes with the bottom four nodes completely fixed.

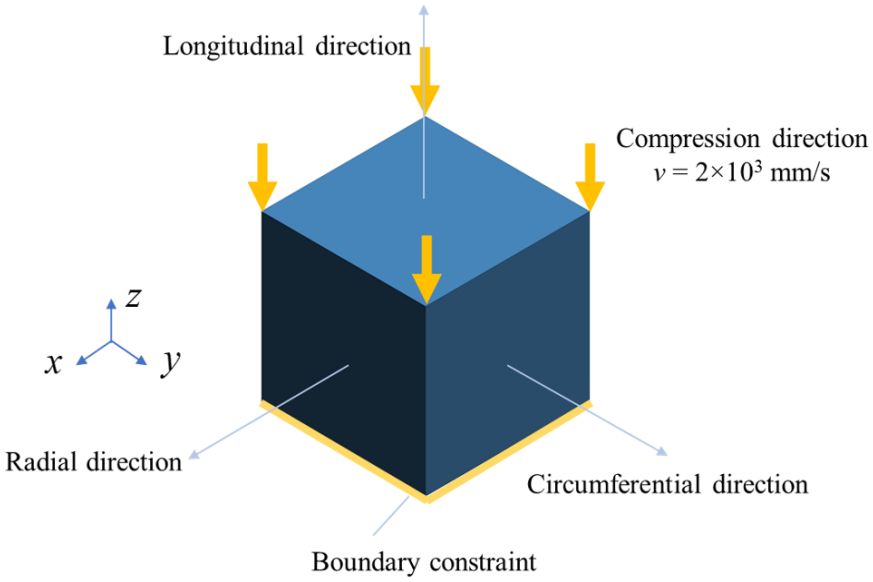

Figure 4.11: FE model of the horn sample for validation in longitudinal compression under dynamic loading.

The stress-strain curve from simulation results was compared to that from test data at a strain rate of 10^3/s, as shown in Figure 4.12. For the same reason as in the case of dynamic compression in the radial direction, two tangent lines were used to determine the initial yield point where a distinct transition was formed from elastic to plastic region in the simulation results. Following the initial elastic region, a plateau region is formed from the initial yield point at approximately 6% strain until approximately 40% strain before a clear plastic hardening started. Figure 4.10 indicated that the plastic hardening behaviors of the horn material under dynamic loading in longitudinal direction were captured very well by the FE simulation. The strain-rate effect in the longitudinal direction was also successfully implemented and validated into the constitutive model that was capable of predicting elastic and plastic deformations at different strain rates.

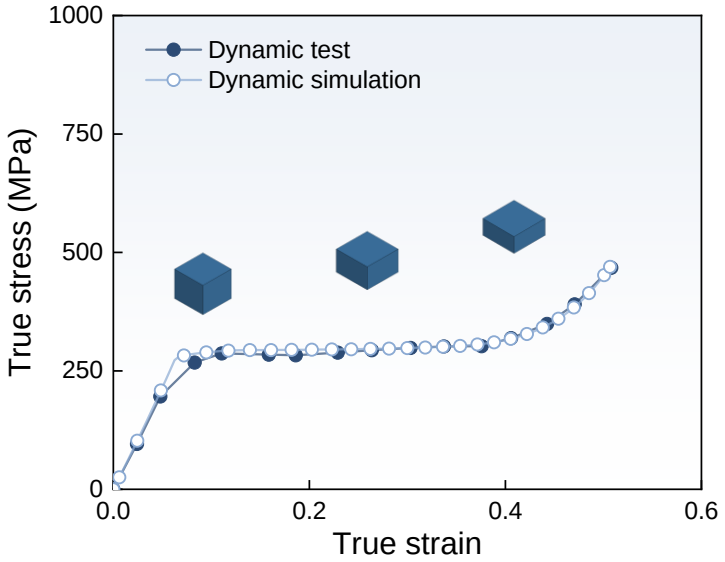

Figure 4.12: Comparison of stress-strain curves from simulation results and test data for the dynamic compression of the horn material in the longitudinal direction.

In the next chapter, the constitutive model with anisotropic hardening and strain-rate effect will be employed in the simulation of dynamic impacts of the horn of bighorn sheep to study the mechanisms of energy dissipation and stress distributions of the horn during impacts.

CHAPTER 5: DYNAMIC IMPACT ANALYSIS OF HORNS

In this chapter, the mechanical behaviors of horns from the bighorn sheep under dynamic impact are analyzed. The validated constitutive model coupled with strain-rate effect was adopted in FE model of the horn and used in the simulations. The direct dynamic impact against the horn was simulated and the stress distributions, displacement wave propagations, and energy conversions were investigated to understand the mechanical behaviors of horns under dynamic impact loading.

5.1 Modeling of the Horn

To study the mechanical behaviors of horns under impact loading with numerical simulations, the geometry of the horn needs to be accurately represented in the finite element model. To this end, the geometry of the horn was obtained from a high accuracy CAD model and was meshed in Hypermesh (Altair Engineering 2021) to obtain the finite element model for this study.

5.1.1 Geometry Modeling

An adult bighorn sheep has a shoulder height of 81 to 101 cm (32 to 40 inches) and is 127 to 157 cm (50 to 62 inches) long (Bighorn Institute 2002). The horn is a typical physical characteristic to distinguish the species' sexual dimorphism. The male sheep's

horn has a more massive shape and diverging curl than the smaller and thinner horn of the female sheep. The horn of an adult male bighorn sheep has a full curl that may extend to 84 cm (33 inches) long, nearly half of the total length of the sheep. The curling angle of female sheep horn is limited below just half a circle.

In nature, most ramming activities between bighorn sheep are among the male sheep. The average weight of a male bighorn sheep was reported to be 79 kg (175 lb) with a range of 68-90 kg (150-200 lb). In this research, the CAD model of an adult male bighorn sheep was obtained and used to develop the horn model. In order to obtain a numerical model that can represent the average geometric characteristics of male bighorn sheep such as shoulder height of 91 cm (36 inches) and weight 79 kg (175 lb), a specific model was then created by scaling from original model to the averaged dimensions. This model was referred as “averaged model” in the following sections. Figure 5.1 showed the overall appearance of the average model of male bighorn sheep.

Figure 5.1: The average model of adult male bighorn sheep.

To simplify the modeling work, the bighorn sheep was assumed symmetric in the average model and only the left-side horn was used for creating the finite element model.

5.1.2 Finite element Modeling

The CAD model of the left-side horn was extracted from the modified bighorn sheep model and the finite element meshes were created using Hypermesh, a commercial pre-processing tool for finite element analysis (Altair Engineering 2021). The geometry of the horn was first screened and adjusted in Hypermesh by applying a geometry cleanup, which merged extremely close vertices to ensure high quality meshes as well as a geometrically continuous model.

In order to assign the transversely isotropic material properties to the horn model, the local principal directions of each element should match with the principal material directions, i.e., radial direction, longitudinal direction, and circumferential direction. To achieve this, the so-called “mapped” style homogenous solid elements were first created to assist assigning the transversely isotropic properties.

Figure 5.2 gave an example of a portion of the “mapped” style solid elements. These uniformly distributed elements were created by mapping solid elements between the front surface (marked as source surface in Figure 5.2) and the back surface (marked as destination surface in Figure 5.2) along the stacking direction. As shown in Figure 5.2, the stacked elements formed “threads” in the stacking direction and elements in the same thread were connected by node sharing with adjacent elements.

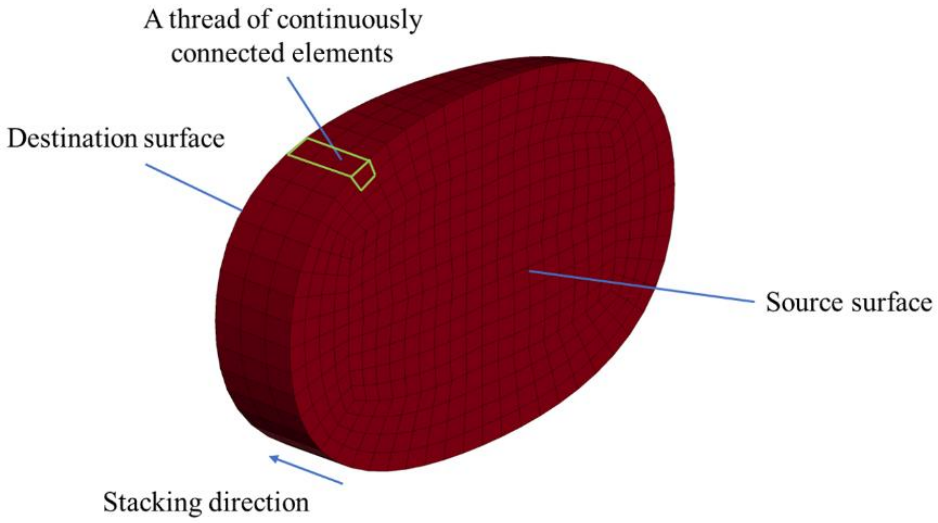

Figure 5.2: An example for mapped style solid elements.

These “mapped” style elements had the following characteristics:

(1) They were created by dragging the elements in between the source and destination surfaces;

(2) Each solid element was similar to an ideal regular hexahedron in order to maintain the perpendicularity among the three principal directions;

(3) The elements were stacked in layers between the source and destination surfaces such that the stacking direction was aligned with the normal directions of the source and destination surfaces;

(4) The number stacked elements in each layer were the same as all other layers to maintain the mapping feature along the stacking direction.

With the technique of creating “mapped” style elements, the curved horn was “cut” into a number of segments by the cross-sectional surfaces at a series of locations along the horn’s growth direction to generate elements suitable for assigning transversely isotropic material properties. The meshing process was completed by applying solid mapping

function with source and destination surfaces in Hypermesh and duplicated nodes were checked and eliminated by merging nodes from both sides of each cutting surface. Figure 5.3 shows the finite element model of a single horn meshed with “mapped” style elements.

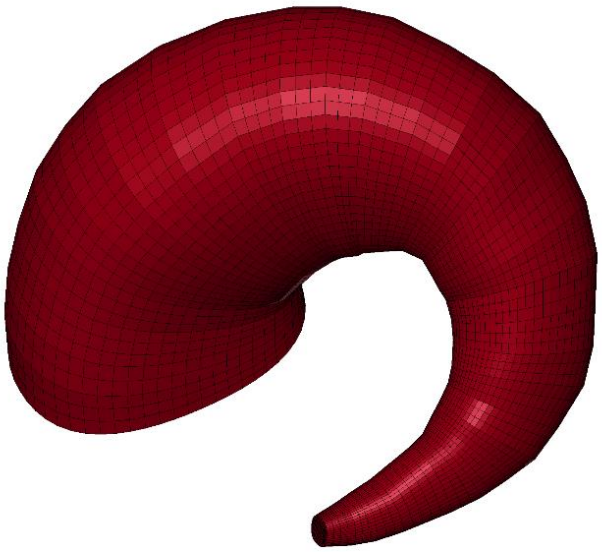

Figure 5.3: The FE model of a single horn meshed with mapped style elements.

Table 5.1: Specifications of FE model of the single horn.

Element Type	Element Number	Node Number.	Average Element Size
Solid constant stress	37,976	41,135	7 mm

The specifications of the FE model of the single horn were summarized in Table 5.1. It had a total of 37,976 hexahedron solid elements and 41,135 nodes. The averaged element size was 7 mm with size gradients, as shown in Figure 5.3, due to the mapping characteristics from a wide proximal base to a very narrow distal end as well as a curled geometry. Constant strain solid elements were assigned to the model, same as that of the

single element validating model discussed in Chapter 3 and Chapter 4. After assigning the orthogonal transversely isotropic material properties to the elements, the local principal directions of the elements were checked in LS-PrePost (Livermore Software Technology 2019) for agreement with the designated material directions as illustrated by the example shown in Figure 5.4.

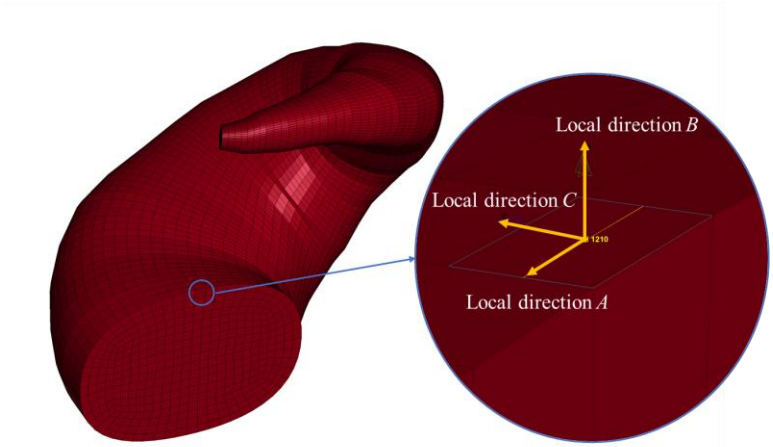

Figure 5.4: Local principal directions of one solid element assigned with orthogonal transversely isotropic material properties.

In Figure 5.4, solid element No.1210 on the exterior edge of the proximal base was selected with the local principal directions shown on the element, highlighted as Local direction *A*, Local direction *B*, and Local direction *C*. Local direction *A* matched with the circumferential direction at the exterior edge, Local direction *B* matched with the radial direction of the selected element, and Local direction *C* matched with the longitudinal direction of the layer that included the selected element. This indicated that the assigned orthogonal material model was correctly recognized by the finite element code. With a density of 1.237 g/cm^3, the total mass of a single horn was determined to be 8.16 kg.

5.2 Dynamic Simulation of the Horn

To study the dynamic impact behavior of the horn, a simplified scenario was developed for the numerical simulation: a single horn was hit by a rigid plate at a velocity of 5.5 m/s along the normal direction of the plate. As discussed in Chapter 1, 5.5 m/s is the maximum impact speed during ramming of bighorn sheep.

The finite element model of the horn developed in Section 5.1 was combined with that of a rigid-plate impactor to create the numerical simulation model, as shown in Figure 5.5. The specifications of the horn-impactor FE model were summarized in Table 5.2. It has two parts composed by a total number of 42,816 nodes that were discretized to 37,976 solid elements for the horn, 1,600 rigid shell elements for the impactor, and 1,681 mass elements for adding extra payload on the impactor.

Table 5.2: Specifications of FE model of the horn-impactor.

Part Number	Node Number	Solid Element Number	Shell Element Number	Mass Element Number
2	42,816	37,976	1,600	1,681

A 13-kg of payload was added to the rigid plate to provide adequate initial impact energy; this added mass represent approximately one sixth of the total mass of a male bighorn sheep. In real situation when two male bighorn sheep ramming against each other, they raised their head and upper body to clash the other one but keep rear foot firmly on the ground for support. The mass that withstands the impact was not the full amount of its

own weight, instead, the part of the weight till the rear leg. In this study, one third of its full weight was chosen the weight for sustain impact, giving one six of total weight to be added on a single horn. Kitchener et al. (1988) determined that the clashing angle of bighorn sheep was approximately 43° measured from the axis normal to the symmetric plane of sheep's skull. In Figure 5.5, the impact direction was determined as the normal direction of the initial contact point on the horn based on a 43° impact angle measured from the proximal base.

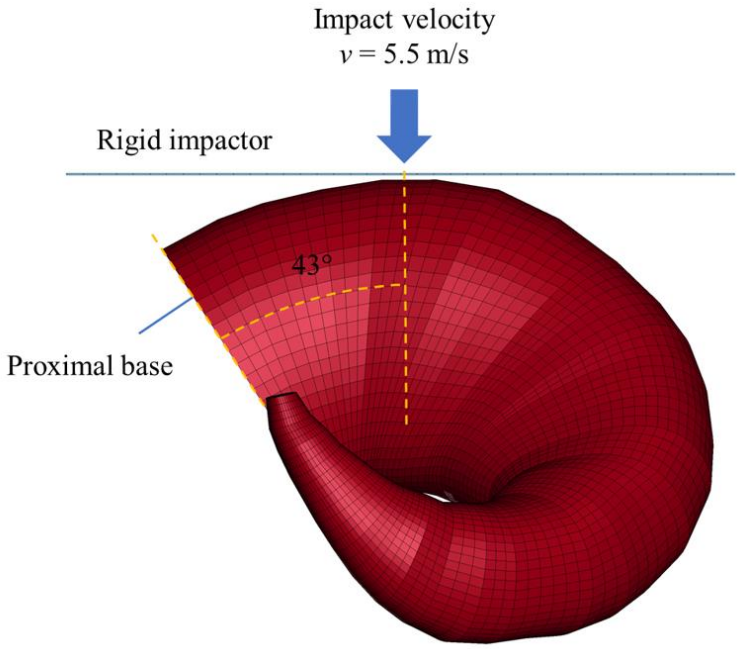

Figure 5.5: Finite element model of the horn-impactor system.

The boundary conditions were assigned to the proximal base of the horn with all three degrees of freedom of the nodes constrained. The automatic-single-surface contact with the segment-based soft option was applied to the rigid impactor and the horn with a coefficient of 0.2 for the dynamic friction. Initial penetrations were cleared by contact checking before running the finite element simulations. To prevent hourglass modes due

to the use of reduced-integration solid elements, a stiffness-based Type 4 hourglass control for solid elements was utilized with a coefficient of 0.03. The hourglass energy and sliding interface energy were calculated and included in the total energy. Mass scaling was not used in the FE analysis for dynamic impact to improve accuracy of simulation results. The termination time for impact was 20 ms and the average time step size during simulation was 10^{-7} s.

5.3 Analysis of Simulation Results

The simulation results of dynamic impact against the horn were analyzed on distributions of stresses and displacements to understand the mechanism of the horn deformations and displacement wave propagations. The time history of energy balance was also examined to learn about the energy absorption of the horn during impacts as well as energy conversions among different forms.

5.3.1 Stress Distributions

The first principal stress and the third principal stress were studied on their distribution patterns in the horn during the dynamic impact. Simulation results showed that the rigid impactor impacted the exterior surface of the horn at a speed of 5.5 m/s and at a 43° angle measured from the proximal base and continuously compressed the horn until the impactor reached zero velocity. The rigid impactor then rebounded from the horn when the deformed horn resumed its shape from elastic deformation. It was observed from the

simulation results that the impact process lasted for 2 ms, after which the rigid impactor lost contact with the horn and the horn underwent self-oscillation with distal end swinging back and forth.

Figure 5.6 shows the distribution of the first principal stresses on the horn at 1.3 ms during the impact process, with the maximum stress value reached 33.3 MPa at the proximal base where the horn was fixed. This indicated that the fixed proximal base was in tension due to the impact load.

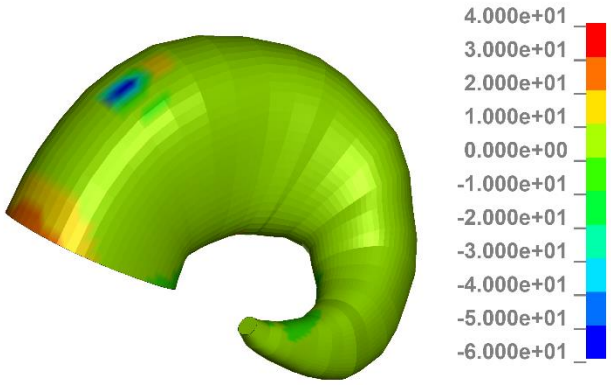

Figure 5.6: Distribution of the first principal stresses (unit: MPa) of the horn at 1.3 ms.

The maximum magnitude of the third principal stress was 174.9 MPa that happened at 1.2 ms and was located at the initial impact point as shown in Figure 5.7. By comparing the distributions of the first and third principal stresses, it was observed that most of the horn was in compression state under the impact loads. Figure 5.8 shows the von Mises stresses with a maximum value of 112.9 MPa near the impact location, exceeding the yield strength of 103.2 MPa that was interpolated based on the average strain rate around the impact location. The permanent deformation was also confirmed by the residual effective

strain at the impact location, which was 3% after the rigid impactor was bounced back and lost contact with the horn. It was observed that the stress distributions of the horn during dynamic impact was localized; the high stresses were limited to the small area around the impact point without spreading to the surrounding areas. This could be beneficial for bighorn sheep to switch to different impact locations on the horn during ramming to allow the localized damaged area to heal.

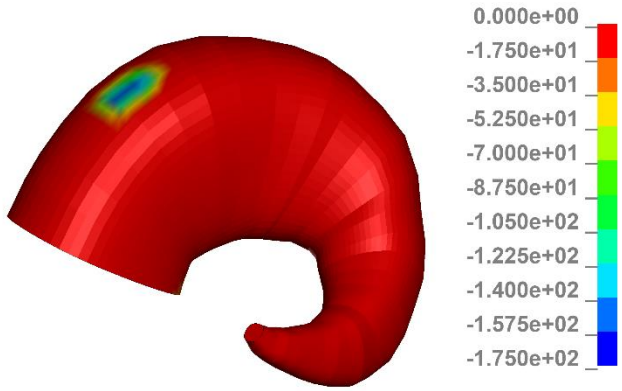

Figure 5.7: Distribution of the third principal stresses (unit: MPa) of the horn at 1.2 ms.

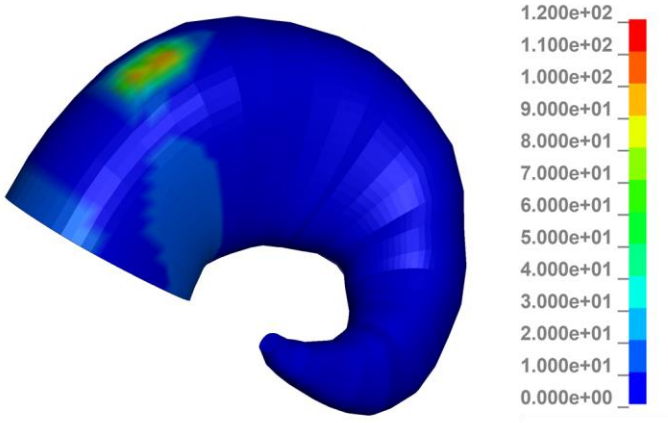

Figure 5.8: Distribution of von Mises stresses (unit: MPa) of the horn at 1.2 ms.

After 2 ms, a cyclic pattern of stress distributions was observed from the evolution of stress waves. Figure 5.9 showed the first principal stress distributions at 8.7 and 9.8 ms. It can be seen that the peak values of the first principal stresses moved spirally from the inner side of the horn to the outer side while traveling towards the distal end. The tip of the horn at the distal end was found to swing inward (i.e., towards the proximal base) when the peak stresses propagated toward the outer side of the horn.

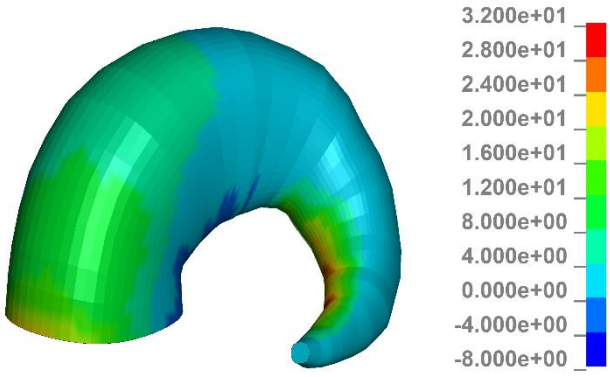

(a)

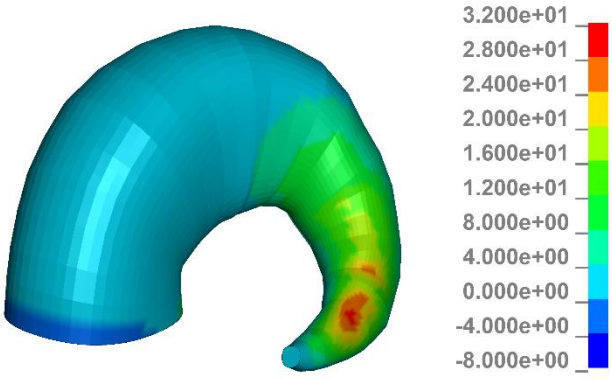

(b)

Figure 5.9: Distribution of the first principal stresses (unit: MPa) of the horn at (a) 8.7 ms; and (b) 9.8 ms.

This spiral pattern of stress propagation was also observed in the third principal stresses, as shown in Figure 5.10 at 9.4 and 11.1 ms. It should be noted that to clearly show the stress contour outside the impact area, the minimum value of the stresses in the legend of Figure 5.10 was set to the minimum stress excluding the impact area. The peak compressive stresses propagated spirally from the inner side of the horn to the outer side while moving towards the distal end. It was observed that the tip of the distal end swung outwards along with the propagation of the peak values of the third principal stresses.

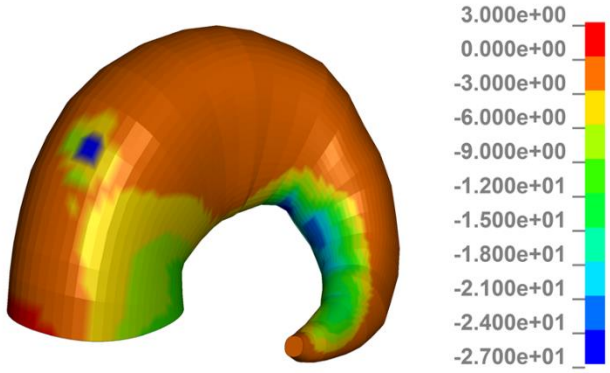

(a)

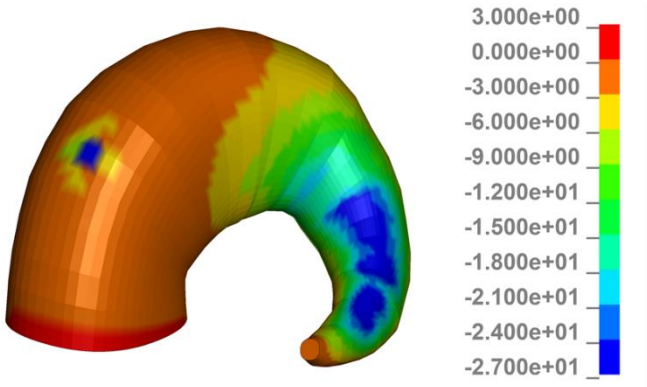

(b)

Figure 5.10: Distribution of the third principal stresses (unit: MPa) of the horn at time of (a) 9.4 ms; and (b) 11.1 ms.

A repetitive impact study was also conducted on the horn to assist in understanding its impact behaviors. The same rigid impactor was used to hit the horn for a total of three times with the same impact speed of 5.5 m/s. At the first impact, the maximum von Mises stress was consistent to the single-impact simulation, with the same value of 113 MPa at 4.6% effective strain. For the second impact, the maximum von Mises stress was 116 MPa with an effective strain of 5.2%. For the third impact, the maximum von Mises stress was increased to 157 MPa with an effective strain of 5.3%. The discrepancy between the maximum von Mises stress values between the second and third impact with relatively similar effective strain was due to the strain-rate effect. After the first impact, the horn gained a portion of the kinetic energy from the impactor and oscillated along the impact direction (i.e., the z-direction). Upon the third impact, the velocity of the horn near the impact location was over ten times higher than the second impact due to the horn's oscillation while the horn's velocity at the second impact was similar to that in the first impact. This was also confirmed by comparing the strain rates of the second and third impacts; the average strain rate at the time of maximum von Mises stress in the third impact was approximately 1.5 times of that in the second impact.

The isotropic material model was also introduced to compared with the constitutive model in this study. An elastic-plastic isotropic material model was used and the uniaxial material preparties from the radial direction (i.e., the impact direction) were assigned to all principal directions. The maximum von Mises stress was found to be 132 MPa with a final effective plastic strain of 4.5% after the impactor left the horn. Both the maximum von Mises stress and effective plastic strain were higher than the results from the anisotropic material model, 113 MPa and 3%, respectively. The comparison showed that the isotropic

material model represented a horn with less stiffness than the anisotropic material model and thus would underestimate the impact resistance and overestimate the damage of the horn.

5.3.2 Propagation of Displacement Waves

To understand the propagation characteristics of displacement waves on the horn under dynamic impact, a thread of elements (a total of 94 elements), which extended from the proximal base to the distal end along the exterior edge of the horn, were selected to extract the displacements of the horn from simulation results for studying the displacement waves (see Figure 5.11). For simplicity, these elements were called “source elements” hereafter; they were uniformly distributed along the longitudinal direction of the horn.

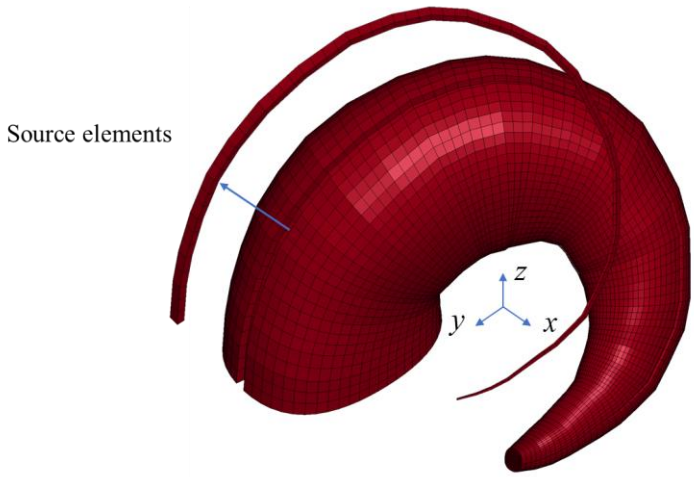

Figure 5.11: A thread of elements (source elements) extending from the proximal base to the distal end.

The time histories of displacement waves of the source elements were obtained from simulation results in all three directions: *x*-, *y*-, and *z*-direction as shown in Figure 5.12, Figure 5.13, and Figure 5.14, respectively. The *z*-direction was aligned with the initial impact direction and the *x*-direction was normal to the midplane of the sheep. In Figures 5.12 to 5.14, the navy-blue color represented the distal end, red color represented the proximal base, and the colors for locations in between were interpolated. As seen from Figures 5.12 to 5.14, the displacement waves in all three directions exhibited a cyclic sinusoid pattern for most of the locations between the proximal base and the distal end, especially for the displacements in the *z*-direction. The displacements at the locations near the distal end are shown clearly to have dominant amplitudes in all three dimensions. For the displacement waves in the *x*-direction, the wave at the distal end had a half-cycle lag to that near the proximal base. This half-cycle lag was also found at certain locations in the displacement waves in the *z*-direction. This lag is beneficial for the horn to cancel out a portion of forces that were generated by the movement of the horns at the locations near the distal end and the proximal base, preventing a severe concussion to the head brain However, there was no obvious lag in the displacement waves in the *y*-direction; the displacement waves at most of locations synced with each other but with different amplitudes.

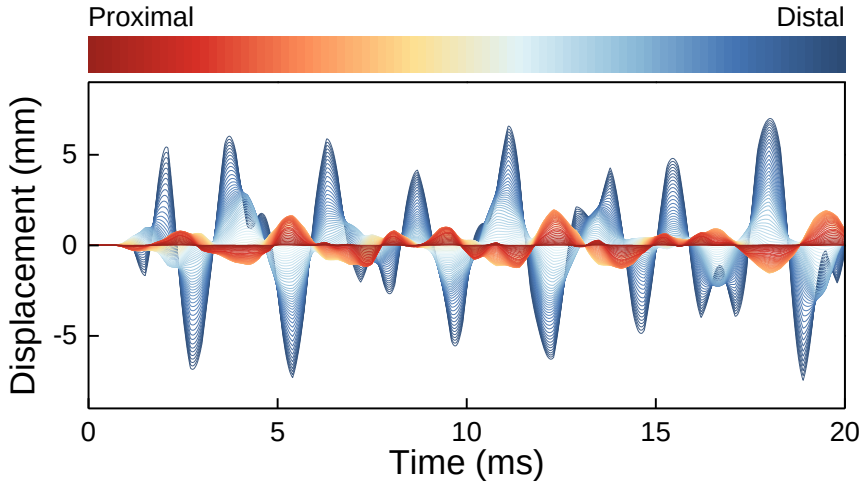

Figure 5.12: Time history of displacement waves in the *x*-direction for locations extending from the proximal base to the distal end of the horn.

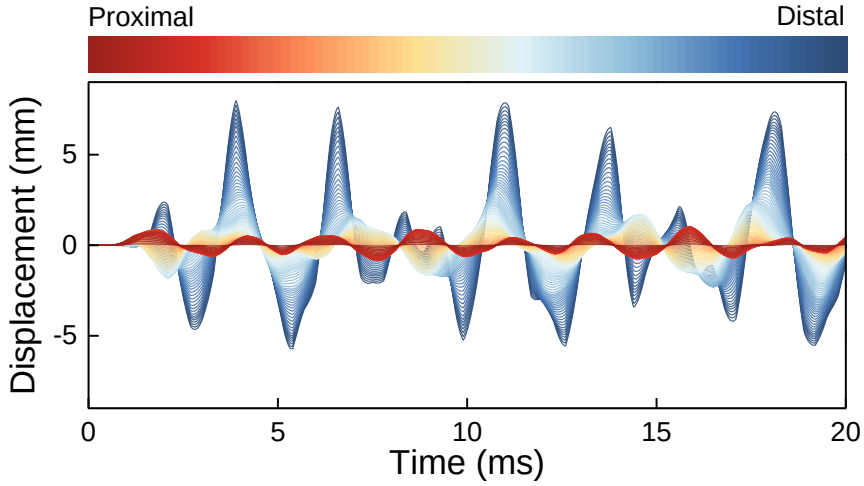

Figure 5.13: Time history of displacement waves in the *y*-direction for locations extending from the proximal base to the distal end of the horn.

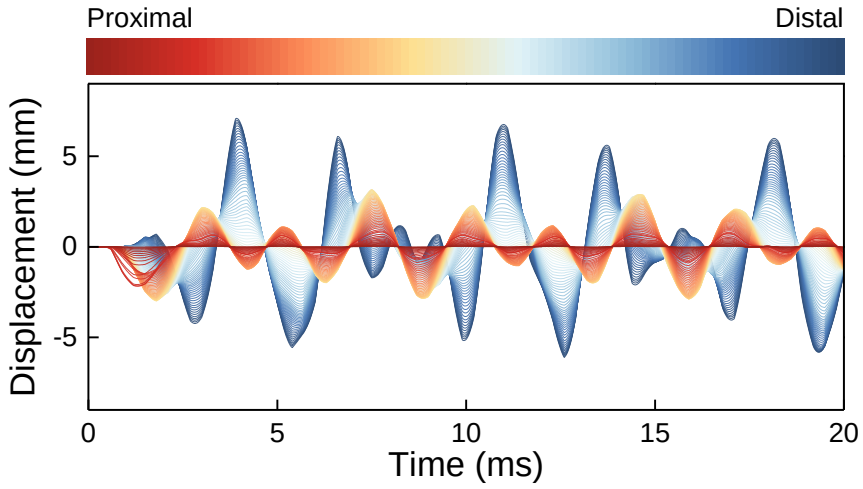

Figure 5.14: Time history of displacement waves in the *z*-direction for locations extending from the proximal base to the distal end of the horn.

Figures 5.15, 5.16, and 5.17 shows the propagations of displacement waves from 1.1 to 1.7 ms in the *x*-, *y*-, and *z*-direction, respectively. These figures showed how the displacement waves propagated between the proximal base and the distal end after the impact was initiated at 0.5 ms near the proximal base. In the *x*-direction, the displacement waves gradually and smoothly propagated towards the distal end, with consistent wavelengths and increased amplitudes as indicated by the increasing depth of color. This is beneficial to smoothly dissipate the impact pulse as to the distal end using the spiral structure with *x*-direction as its central axis. The wavefront with high amplitude was moving to the distal end, causing the oscillation of horn material concentrated mainly on the distal end which was far from the proximal end that was connected with skull. In the *y*-direction, the displacement waves also propagated towards the distal end, but had a sharp transition between 1.3 to 1.4 ms. In the *z*-direction, the propagation of displacement waves

was accompanied by expanded wavelengths as indicated by the widths of blue bands in Figure 5.17. The expanded wavelengths can be explained by the accumulated deformation in the impact direction. After initial impact, the permanent deformation at the impact location started to affect the movement of surrounding areas. The wave incited by initial impact radiated from the impact location to the distal end, which is considered as an approach of inducing more horn material to absorb impact energy. The expanding of wavelength also consumed the impact force in *z*-direction, helping to reduce the forces applied on the sheep skull. The displacement waves in the *z*-direction also had the largest amplitudes among the three directions.

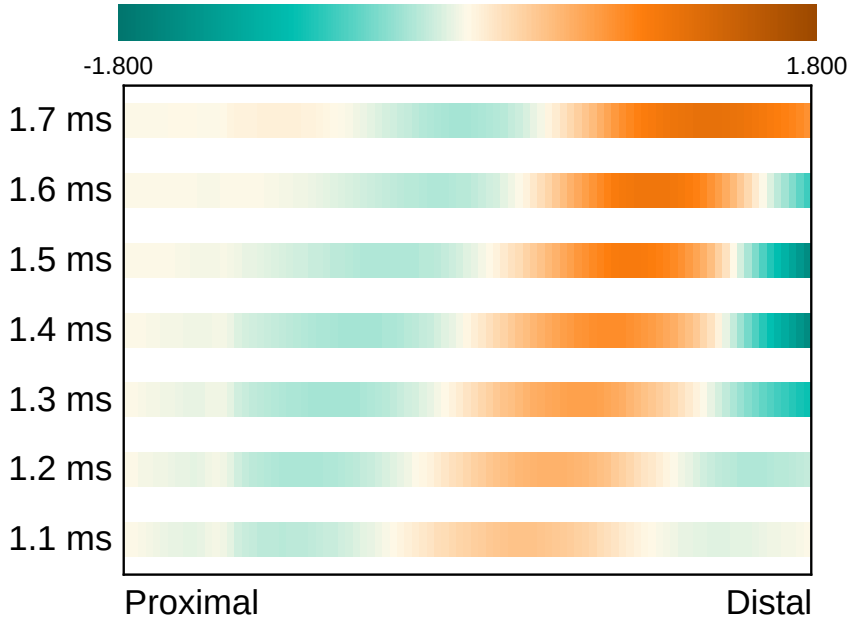

Figure 5.15: Displacement wave propagation in the *x*-direction from the proximal base to the distal end of the horn (unit: mm).

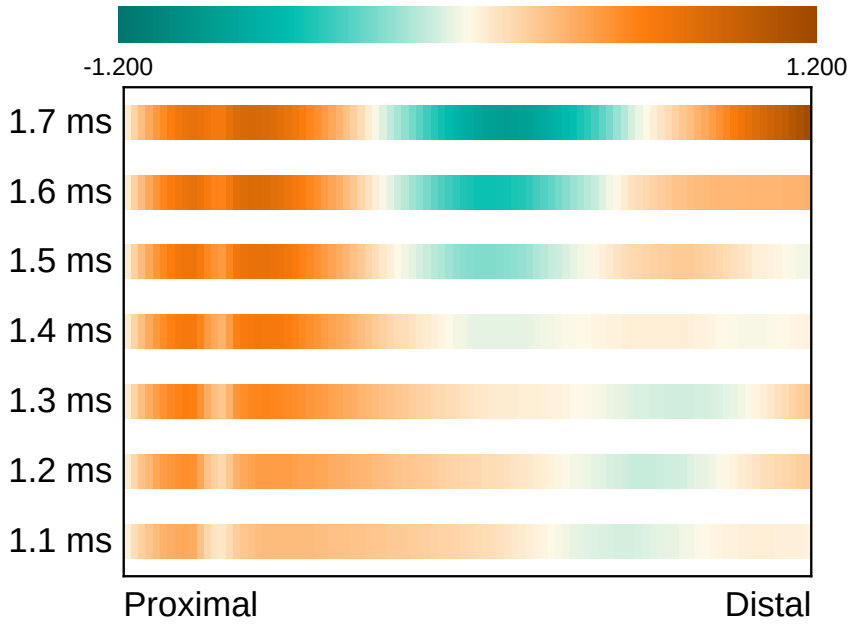

Figure 5.16: Displacement wave propagation in the *y*-direction from the proximal base to the distal end of the horn (unit: mm).

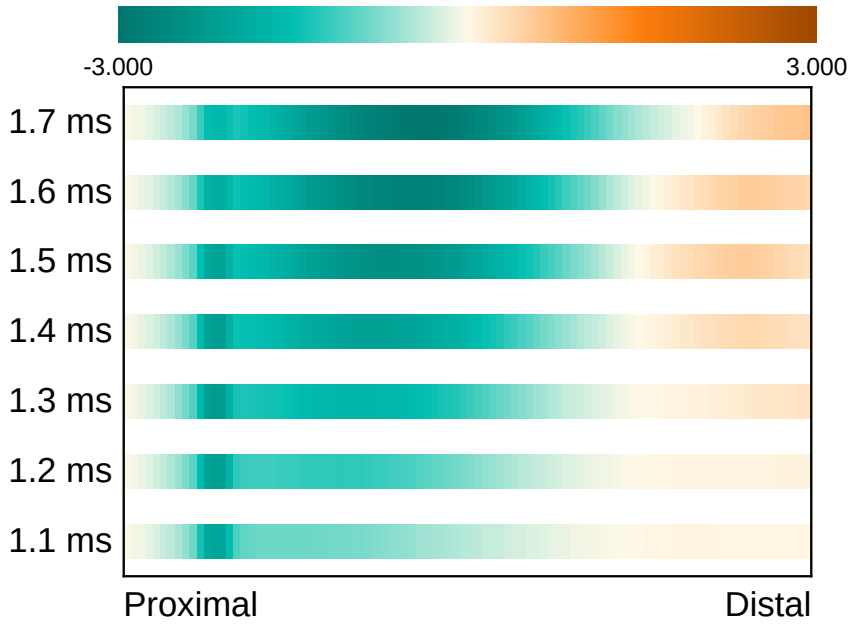

Figure 5.17: Displacement wave propagation in the *z*-direction from the proximal base to the distal end of the horn (unit: mm).

5.3.3 Energy Transmission and Conversions

In the horn-impactor simulation, the total impact energy came from the kinetic energy of the impactor, which was 197 J with an initial velocity of 5.5 m/s and a 13-kg payload. The time history of energy balance for the first 15 ms of the impact was extracted from the simulation results, as shown in Figure 5.18. Four different types of energy were reported: kinetic energy, internal energy (or strain energy), hourglass energy, and sliding interface energy. The hourglass energy is a non-physical energy associated with the hourglass control that should be less than 10% of peak internal energy in numerical simulations to be considered acceptable. In the horn-impactor system, hourglass energy

was calculated to be 1.8% of the peak internal energy. The sliding interface energy is also known as contact energy, caused by the frictional force on the contact interface.

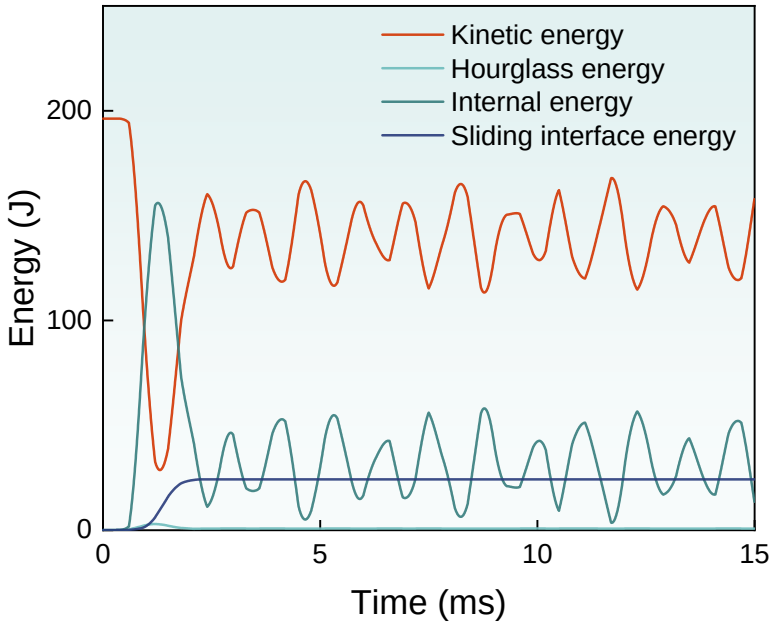

Figure 5.18: Time history of energy balance of the horn-impactor simulation.

When the impact was initiated at 0.5 ms, the impactor started compressing the horn and the kinetic energy of the impactor was transformed into the internal energy of the horn until it became zero. Figure 5.19 shows the time history of the impactor's kinetic energy in which the kinetic energy reached zero at 1.3 ms. At 1.3 ms, the internal energy of the horn reached maximum as shown in Figure 5.18. The internal energy of the horn consisted of two parts: internal energy from elastic deformation and internal energy from plastic deformation. When the horn started resuming from elastic deformation, the impactor was pushed back by the horn and regained some kinetic energy transformed from the horn's internal energy. The impactor completely lost contact with the horn at 2 ms and kept

moving outward at a constant speed while its kinetic energy remained constant. Due to impact pulse, the horn also gained a small portion of kinetic energy that caused its vibration as shown in Figure 5.20. In Figure 5.18, the total kinetic energy at 1.3 ms was from the horn's kinetic energy, because the kinetic energy of the impactor reached zero at 1.3 ms. After 2 ms, the energy remained in the horn interchanged cyclically between its kinetic energy and internal energy as seen from the oscillations in Figure 5.20.

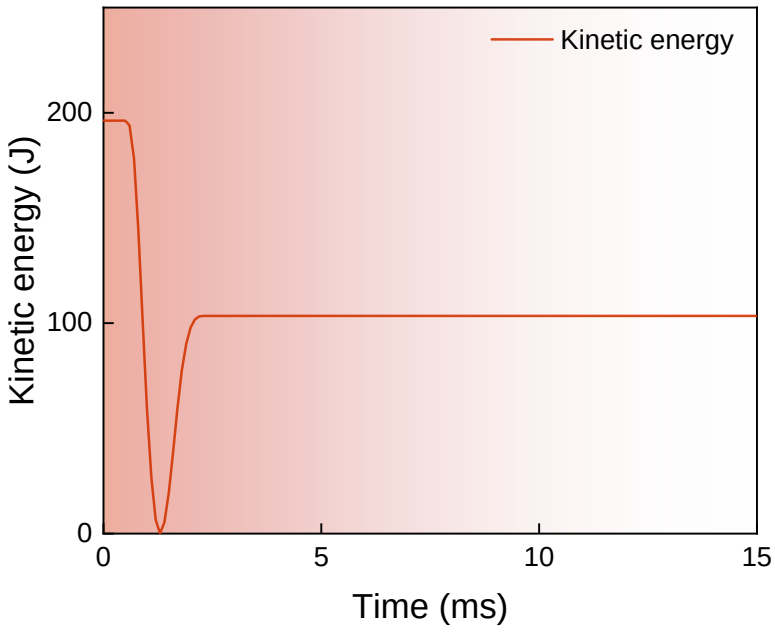

Figure 5.19: Time history of the impactor's kinetic energy during dynamic impact.

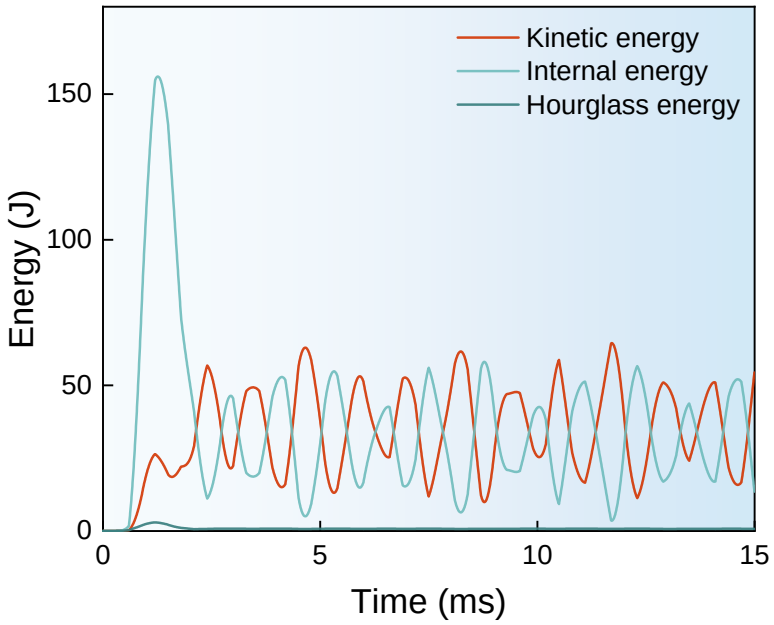

Figure 5.20: Time history of the horn's energy during dynamic impact.

The percentage contributions of different types of energy to the total system energy were calculated for several time instants, as shown in Figure 5.21, to demonstrate the evolution of energy compositions. Before the impactor had its first contact with the horn at 0.5 ms, the total energy was 100% from the impactor in the form of kinetic energy. From 0.5 to 1.3 ms, the internal energy of the horn increased from zero to its maximum due to elastic and plastic deformations and accounted for 81% of the total energy. It should be noted that the impactor had no internal energy due to the use of rigid material. At 1.3 ms, 4.7% of the initial kinetic energy was converted to sliding energy due to friction, 1.4% was converted to hourglass energy, and 12.9% was converted to the horn's kinetic energy. Figure 5.22 shows an energy conversion diagram for the horn from the starting time when the impactor firstly contacted with the horn at 0.5 ms to the time with maximum internal

energy (at 1.3 ms). It can be seen that the horn is capable of temporally storing a large amount of energy converted from the impact energy.

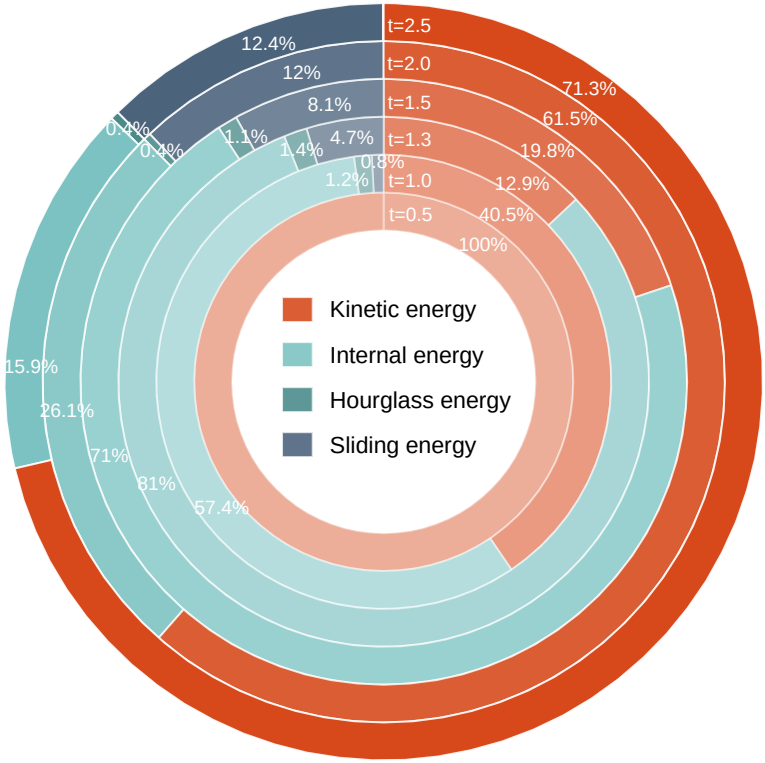

Figure 5.21: Evolution of energy compositions in the horn-impactor system during dynamic impact.

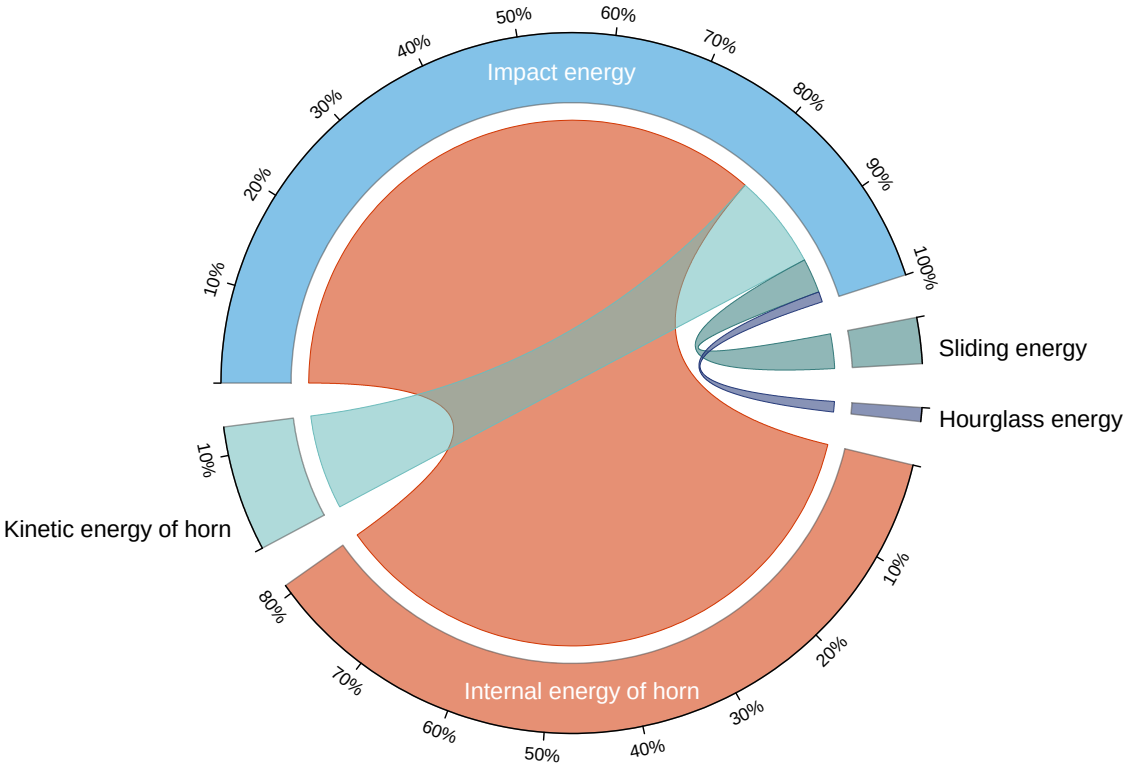

Figure 5.22: Energy conversion in the horn-impactor system from the time at initial impact to the time with maximum internal energy.

For energy that could be dissipated, such as sliding interface energy, it could not be recycled back and participate in energy conversions. After 1.3 ms, part of the horn's internal energy was released upon resuming from elastic deformation and converted to the impactor's kinetic energy, which reached 61.5% of the total initial energy in 0.7 ms as the impactor being bounced back. The system energy reached a state of dynamic equilibrium at 2 ms when the impactor completely lost contact with the horn.

Figure 5.23 showed the energy conversion flow diagram from the time when the horn had maximum internal energy (at 1.3 ms) to the initial state of dynamic equilibrium

(at 2.0 ms). Additional energy was further dissipated into the sliding energy when the impactor was leaving from the horn, leading to a total of 12.4% of total impact energy lost caused by frictional forces. The 52.7% of initial impact energy was converted back to the impactor as its kinetic energy from the bouncing-back released speed. The remaining 34.9% of initial impact energy was retained inside the horn that can be discretized into 18.7% of initial impact energy as its kinetic energy and 16.2% of initial impact energy as its internal energy.

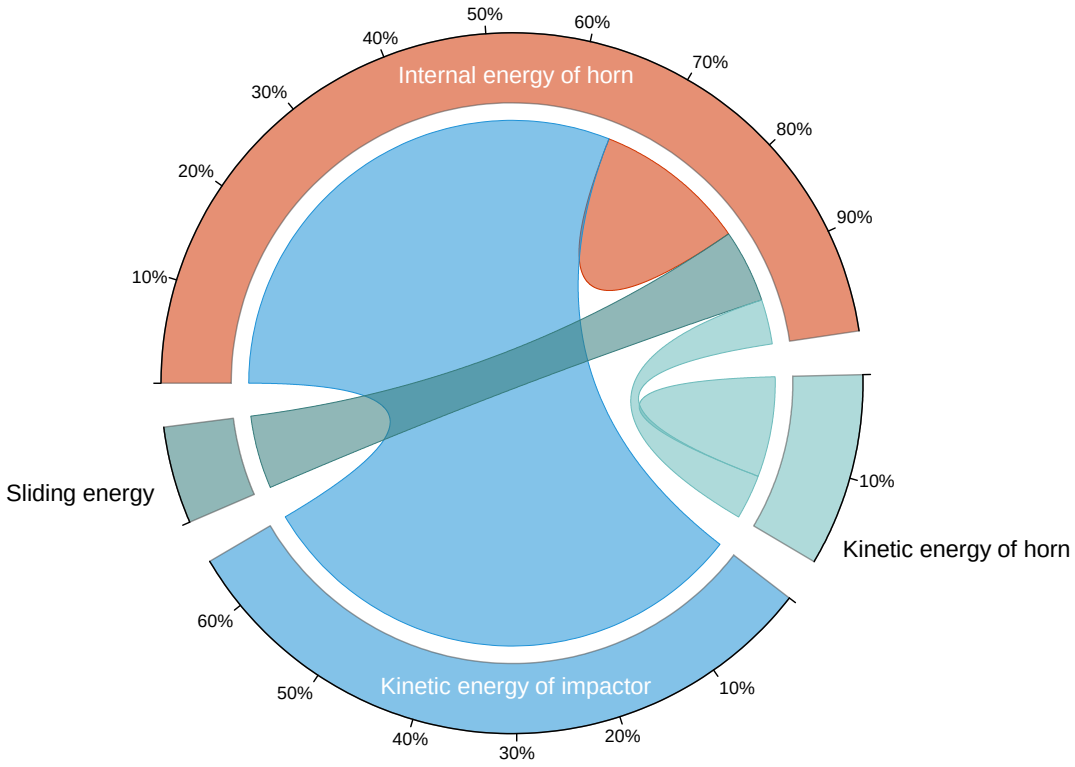

Figure 5.23: Energy conversions in the horn-impactor system after dynamic impact.

From the study of stress distributions, displacement wave propagations, and the energy conversions, the mechanisms of bighorn sheep horn to withstand dynamic impact was learnt from the following three perspectives:

The permanent damage of the horn from impacts during ramming was predominantly due to compression and localized around the impact location. This was shown by the effective plastic strain from the dynamic impact simulation. The stress wave propagated through the horn following a spiral pattern from the inner side to the outer side while moving along the growing direction of the horn. At the same time, the distal tip vibrated back and forth as a result of the stress wave propagations.

The study on displacement wave propagations showed that the energy stored in the horn was mainly due to the displacement waves in the impact direction and the spiral extending direction where the distal tip swung about the central axis. This observation coud be verified through the time history of energy balance at the state of dynamic equilibrium after impact. The kinetic energy stored in the horn by the displacement wave propagations was found to be higher than the horn's internal energy caused by plastic deformation.

The study on energy conversions indicated that the horn had a high capacity of absorbing the impact energy with a maximum conversion ratio of 81%. After reaching the maximum internal energy, the horn then released part of the stored energy to the impactor as kinetic energy and also maintained a dynamic equilibrium itself with oscillating internal and kinetic energy. This study indicated that the bighorn sheep horn could sustain the large impact loads without severe damage to the horn from ramming at a speed up to 5.5 m/s.

CHAPTER 6: CONCLUSIONS

In this dissertation research, a transversely isotropic constitutive model with anisotropic hardening coupled with strain-rate effect was developed for the horn material of bighorn sheep, and implemented into the commercial finite element code, LS-Dyna, as a user-defined material subroutine (UMAT) for simulations of horns under dynamic impact loadings. The horn of bighorn sheep was made of a keratin-based bio-composite material with tubule-lamella structure. In the constitutive model, three orthogonal principal directions were defined at the element level: the first principal direction in the extending direction of hollow tubules that is parallel to the longitudinal direction of the horn, the second principal direction in the stacking direction of the lamella that is the radial direction on a cross-section of the horn, and the third principal direction in the circumferential direction on a cross-section of the horn. The special stacking structure of the horn, i.e., the tubules surrounded by layered lamellas, causes the horn to have different mechanical responses under uniaxial compressions in the three principal directions and therefore is referred as an anisotropic material. The anisotropy of the horn material was confirmed by extensive experimental studies, particularly on its anisotropic hardening rules. From the uniaxial compression tests of the horn, it was observed that the horn material had similar mechanical responses and materials properties in the radial and circumferential directions and thus was simplified to a transversely isotropic material. It was also confirmed from experimental data that strain-rate effects existed in the horn material under dynamic impact loading. To model the mechanical behaviors of the horn material with fidelity, the transversely isotropic constitutive model, which was initially developed for quasi-static

loading conditions based on the modified stress theory of Li. et al. (2018), was improved by including the strain-rate effect for simulating dynamic impacts with strain rates up to 10^3/s.

In the transversely isotropic constitutive model, anisotropic hardening was achieved by introducing a hardening factor tensor to scale a nonuniform expanding yield surface back to its initial state. To determine the parameters for material properties used in the constitutive model, experimental data from quasi-static uniaxial compression tests were used to characterize the anisotropic hardening behaviors of the horn material in the three principal directions. The strain-rate effect was later coupled into the model by interpolating material parameters between the quasi-static test data (with a strain rate of 10^{-3}/s) and dynamic impact test data (with a strain rate of 10^3/s). The constitutive model was implemented into LS-Dyna as a UMAT and validated using a single-element FE model of 4×4×4 mm^3 horn sample, which had the same dimensions as those used in the uniaxial compression tests under quasi-static and dynamic loading. The simulation results showed that the constitutive model could accurately predict the mechanical responses of the horn material under both quasi-static and dynamic loading conditions.

The validated constitutive model was then used in FE simulation of an entire horn under dynamic impact loading to investigate the mechanisms of its energy absorption and conversion, stress distributions, and displacement wave propagations. A rigid impactor with a payload of 13 kg was included to initiate a direct impact against a single horn with an impact angle of 43° and a speed of 5.5 m/s. The horn absorbed 81% of the total kinetic energy of the impactor (referred as “total impact energy” hereafter) within 1.3 ms and stored it as its internal energy from both elastic and plastic deformations. The distributions

of the first principal stresses and the third principal stresses showed that the stress waves propagated from the inner side to the exterior edge of the horn, following a spiral pattern with its distal end oscillating back and forth. The energy remaining inside the horn after impact was interchangeably converted between its internal energy and kinetic energy to reach a dynamic equilibrium. Except for the lost energy in the form of sliding energy and hourglass energy, 34.9% of the total impact energy was stored in the horn and 52.7% of the total impact energy was retained by the impactor after leaving the horn.

In summary, the constitutive model of the horn material developed in this study could accurately capture the mechanical responses of the horn under both quasi-static and dynamic loading conditions. The successful implementation of the constitutive model into LS-Dyna facilitated its validation and more importantly, its use in the dynamic impact simulation of the entire horn to understand the mechanism of sustaining impact loading from the perspectives of energy absorption/conversion, stress distributions, and displacement wave propagations. Such understanding is essential and beneficial to developing bioinspired materials that can be used in applications for impact resistance and dissipations.

This dissertation research provides a pathway to model biological materials using finite element analysis. In biomechanics, coupon-level testing of a variety of biological materials such as cortical bone, ligament, and tendon, has been widely conducted under uniaxial loading conditions. With the original test data for these biological materials, the corresponding constitutive models can be developed and integrated into commercial finite element analysis tools using the method developed in this research. These models can then be used to investigate the mechanical behaviors of these biological materials under

complex loading conditions. Such investigations can be very difficult and challenging using the method of data collection from live human bodies or cadavers.

It should be noted that the horn model of this study was simplified such that it did not distinguish the trabecular bone inside the horn and the horn ridges on the exterior surface. In a bighorn sheep horn, the horn material transitioned from trabecular bone at inner core to cortical bone surrounded by exterior horn sheath (Fuller et al., 2021). This type of trabecular-cortical-sheath combination extended in the longitudinal direction until the cross-section that formed approximately 90° with the proximal base (Drake et al., 2016). The horn was also connected to the skull at its proximal base through cortical bone. In future investigations, the inner bone can be modeled with functionally gradient materials to simulate the transition from the trabecular bone to the cortical bone and the surrounding horn sheath. The membrane interface between the cortical bone and horns sheath can also be considered in the studies of stress propagation and impact pulse dissipation. A more comprehensive exterior shape, i.e., with horn ridges, can be considered in developing future horn models to study the benefits of these ridges in stress propagation and energy dissipations.

Other future work may be conducted on coupon-level testing under compression and shear loads with a wide range of strain rates. These experimental data are necessary to further improve the fidelity of the constitutive models under dynamic impacts. With respect to hydration levels, future horn models could include hydration effect since high hydration levels decrease the stiffness, strength, and anisotropy of the horn material. Horn models with the highest possible hydration level and lowest hydration level may be developed to understand its mechanical behaviors at these two extreme conditions. Finally, a skull model

may be developed and combined with the horn model to form to a head complex, which can used to investigate the effect on the brain and potential head damage under dynamic impacts on the horns. Stress distributions and impact pulse propagations inside the head can also be studied to understand the mechanism of how head concussions are prevented by the bighorn sheep during ramming.

REFERENCES

Altair Engineering (2021). *HyperMesh User Guide*. Altair Engineering, Troy, Michigan.

Drake, A., Donahue, T. L. H., Stansloski, M., Fox, K., Wheatley, B. B., & Donahue, S. W. (2016). Horn and horn core trabecular bone of bighorn sheep rams absorbs impact energy and reduces brain cavity accelerations during high impact ramming of the skull. *Acta Biomaterialia*, *44*, 41-50.

Fuller, L. H., & Donahue, S. W. (2021). Material properties of bighorn sheep (Ovis canadensis) horncore bone with implications for energy absorption during impacts. *Journal of the Mechanical Behavior of Biomedical Materials*, *114*, 104224.

Hill, R. (1948). A theory of the yielding and plastic flow of anisotropic metals. *Proceedings of the Royal Society of London. Series A. Mathematical and Physical Sciences*, *193*(1033), 281-297.

Huang, W., Zaheri, A., Jung, J. Y., Espinosa, H. D., & Mckittrick, J. (2017). Hierarchical structure and compressive deformation mechanisms of bighorn sheep (Ovis canadensis) horn. *Acta Biomaterialia*, *64*, 1-14.

Huang, W., Zaheri, A., Yang, W., Kisailus, D., Ritchie, R. O., Espinosa, H., & McKittrick, J. (2019). How water can affect keratin: hydration-driven recovery of bighorn sheep (Ovis canadensis) horns. *Advanced Functional Materials*, *29*(27), 1901077.

Johnson, K. L., Trim, M. W., Horstemeyer, M. F., Lee, N., Williams, L. N., Liao, J., Rhee, H. & Prabhu, R. (2014). Geometric effects on stress wave propagation. *Journal of Biomechanical Engineering*, *136*(2), 021023.

Johnson, K. L., Trim, M. W., Francis, D. K., Whittington, W. R., Miller, J. A., Bennett, C. E., & Horstemeyer, M. F. (2017). Moisture, anisotropy, stress state, and strain rate effects on bighorn sheep horn keratin mechanical properties. *Acta Biomaterialia*, *48*, 300-308.

Johnson, K. L., Trim, M. W., Mao, Y., Rhee, H., Williams, L. N., Liao, J., Griggs, J., Horstemeyer, M. F., & Duan, Y. (2021). Finite element analysis of a ram brain during impact under wet and dry horn conditions. *Journal of the Mechanical Behavior of Biomedical Materials*, *119*, 104400.

Kitchener, A. (1988). An analysis of the forces of fighting of the blackbuck (Antilope cervicapra) and the bighorn sheep (Ovis canadensis) and the mechanical design of the horn of bovids. *Journal of Zoology*, *214*(1), 1-20.

Lee, N., Liu, Z., Mun, S., Johnson, K., & Horstemeyer, M. F. (2019). The function of horn ridges for impact damping. *Available at SSRN 3322822*.

Li, P., Guo, Y. B., & Shim, V. P. W. (2018). A constitutive model for transversely isotropic material with anisotropic hardening. *International Journal of Solids and Structures*, *138*, 40-49.

LSTC (2019). *LS-DYNA Theory Manual*. Livermore Software Technology Corporation, Livermore, CA.

Lubliner, J. (2008). *Plasticity Theory*. Courier Corporation.

Maity, P., & Tekalur, S. A. (2011). Finite element analysis of ramming in Ovis canadensis. *Journal of Biomechanical Engineering*, *133*(2).

McKittrick, J., Chen, P. Y., Tombolato, L., Novitskaya, E. E., Trim, M. W., Hirata, G. A., Olevsky, E.A., Horstemeyer, M.F., & Meyers, M. A. (2010). Energy absorbent natural materials and bioinspired design strategies: a review. *Materials Science and Engineering: C*, *30*(3), 331-342

North American Nature. Two ramming bighorn sheep [Online image]. Where do bighorn sheep live. https://northamericannature.com/where-do-bighorn-sheep-live/

Pouriayevali, H. (2013). Describing large deformation of polymers at quasi-static and high strain rates. [Doctoral dissertation, National University of Singapore].

Tagarielli, V. L., Deshpande, V. S., Fleck, N. A., & Chen, C. (2005). A constitutive model for transversely isotropic foams, and its application to the indentation of balsa wood. *International Journal of Mechanical Sciences*, *47*(4-5), 666-686.

Tombolato, L., Novitskaya, E. E., Chen, P. Y., Sheppard, F. A., & McKittrick, J. (2010). Microstructure, elastic properties and deformation mechanisms of horn keratin. *Acta Biomaterialia*, *6*(2), 319-330.

Trim, M. W., Horstemeyer, M. F., Rhee, H., El Kadiri, H., Williams, L. N., Liao, J., Walters, K. B., McKittrick, J. & Park, S. J. (2011). The effects of water and microstructure on the mechanical properties of bighorn sheep (Ovis canadensis) horn keratin. *Acta Biomaterialia*, *7*(3), 1228-1240.

Wegst, U. G. K., & Ashby, M. F. (2004). The mechanical efficiency of natural materials. *Philosophical Magazine*, *84*(21), 2167-2186.

Zhang, Y., Huang, W., Hayashi, C., Gatesy, J., & McKittrick, J. (2018). Microstructure and mechanical properties of different keratinous horns. *Journal of the Royal Society Interface*, *15*(143), 20180093.

Zhu, B., Zhang, M., & Zhao, J. (2016). Microstructure and mechanical properties of sheep horn. *Microscopy Research and Technique*, *79*(7), 664-674.

APPENDIX A: COMPILING USER-DEFINED MATERIAL SUBROUTINE FOR LS-DYNA

This appendix provides instructions on compiling a user-defined material subroutine (UMAT) for the MPP version of LS-Dyna R12.0.0 in the Linux environment. This compiling method is also compatible to previous versions of LS-Dyna since R11.2.0.

A.1 The Original UMAT Package

The original UMAT package of LS-Dyna was provided by LSTC as a template for users to develop their own material subroutines. It can be obtained from the FTP site of LSTC associated with the organization that purchased LS-Dyna licenses or by requesting LSTC customer service to provide the package.

In this study, the UMAT was compiled for the MPP version of LS-Dyna R12.0.0 x64 with double precision, which had the corresponding UMAT package named as

```
ls-dyna_mpp_d_R12_0_0_x64_centos65_ifort160_sse2_openmpi4.0.0.usermat.tar.gz
```

Save this package in the working directory where the UMAT is to be compiled and then unzip it using the following command in a Linux terminal under the same working directory

```
tar -xzf <name of the UMAT package>
```

The package contains two vital files, `dyn21umats.f` and `Makefile`. The file `dyn21umats.f` contains the source code provided by LSTC for developing user-defined

subroutines and `Makefile` is the command script for compiling `dyn21umats.f` using a Fortran compiler.

A.2 Modifying the UMAT Package

The available templates in `dyn21umats.f` are `subroutine umat41` to `umat50` from which a user may choose for user-defined material subroutines. In this study, `subroutine umat41` was chosen for the anisotropic hardening constitutive model. Replace the contents of `subroutine umat41` with the Fortran code for the user-defined material model and the UMAT is ready for compiling.

The calculations in the UMAT of this study need a series of subroutines provided by the Math Kernel Library (MKL), whose local directory and library files need to be specified in `Makefile`. The following directory and library files are what were used in this study on the Linux system.

```
LIBS_LOCAL=${MKLROOT}/lib/intel64/libmkl_blas95_ilp64.a
${MKLROOT}/lib/intel64/libmkl_lapack95_ilp64.a
${MKLROOT}/lib/intel64/libmkl_scalapack_ilp64.a -Wl,--start-group
${MKLROOT}/lib/intel64/libmkl_intel_ilp64.a
${MKLROOT}/lib/intel64/libmkl_sequential.a ${MKLROOT}/lib/intel64/libmkl_core.a
${MKLROOT}/lib/intel64/libmkl_blacs_openmpi_ilp64.a -Wl,--end-group -lpthread -
lm -ldl
```

The following is the complete `Makefile` for compiling the UMAT and create the LS-Dyna executable file.

```
#
# Makefile for building mppdyna
# on 'Open-MPI 4.0.0 Xeon64'
# for 'Linux CentOS 6.5'
# using 'Intel Fortran Compiler 2020'
#
LMATH=/opt/intel/compilers_and_libraries_2016/linux/mkl/lib/intel64/libmkl_scal
apack_ilp64.a /opt/intel/compilers_and_libraries_2016/linux/mkl/lib/intel64/lib
mkl_intel_ilp64.a /opt/intel/compilers_and_libraries_2016/linux/mkl/lib/intel64
/libmkl_sequential.a /opt/intel/compilers_and_libraries_2016/linux/mkl/lib/inte
l64/libmkl_core.a /opt/intel/compilers_and_libraries_2016/linux/mkl/lib/intel64
/libmkl_blacs_intelmpi_ilp64.a /opt/intel/compilers_and_libraries_2016/linux/mk
```

```
l/lib/intel64/libmkl_scalapack_ilp64.a /opt/intel/compilers_and_libraries_2016/
linux/mkl/lib/intel64/libmkl_intel_ilp64.a /opt/intel/compilers_and_libraries_2
016/linux/mkl/lib/intel64/libmkl_sequential.a /opt/intel/compilers_and_librarie
s_2016/linux/mkl/lib/intel64/libmkl_core.a /opt/intel/compilers_and_libraries_2
016/linux/mkl/lib/intel64/libmkl_blacs_intelmpi_ilp64.a /opt/intel/compilers_an
d_libraries_2016/linux/mkl/lib/intel64/libmkl_scalapack_ilp64.a /opt/intel/comp
ilers_and_libraries_2016/linux/mkl/lib/intel64/libmkl_intel_ilp64.a /opt/intel/
compilers_and_libraries_2016/linux/mkl/lib/intel64/libmkl_sequential.a /opt/int
el/compilers_and_libraries_2016/linux/mkl/lib/intel64/libmkl_core.a /opt/intel/
compilers_and_libraries_2016/linux/mkl/lib/intel64/libmkl_blacs_intelmpi_ilp64.
a
#
FC=mpif90
#
FF=-safe_cray_ptr -assume byterecl,buffered_io,protect_parens -warn nousage -
zero -ftz -fp-model precise -mP2OPT_hpo_dist_factor=21 -
diagdisable 10212,10010 -fimf-arch-consistency=true -qno-opt-dynamic-align -
xSSE2 -align array16byte -traceback -pad -DLINUX -DIFORT -DNET_SECURITY -
DADDR64 -DINTEL -DXEON64 -DFCC80 -DTIMER=cycle_time -DSSE2 -DOVERRIDE -DMPP  -
DAUTODOUBLE -DNEWIO -DHAVE_BLAS_LAPACK -DHAVE_I8R8_LIBRARY -DMF3_SYM -
DNEW_UNITS -DEXTENDED -DBATTERY -DDUALCESE -DUSE_R123 -DLSTCODE -DBIGID -
DENABLE_HASH3 -DFFTW -DROTORDYN -DMUMPS -DLSGPART -DMF3_SYM -DMCMS -DUSES_CXX -
DPFEM -DMUMPSVER=stable -DUSES_CPP -DPTHREADS -i8 -r8 -fPIC -O2
#
LD=mpif90 -sox -static-intel
#
LF= -safe_cray_ptr -assume byterecl,buffered_io,protect_parens -warn nousage -
zero -ftz -fp-model precise -mP2OPT_hpo_dist_factor=21 -diag-
disable 10212,10010 -fimf-arch-consistency=true -qno-opt-dynamic-align -xSSE2 -
align array16byte -traceback -pad -DLINUX -DIFORT -DNET_SECURITY -DADDR64 -
DINTEL -DXEON64 -DFCC80 -DTIMER=cycle_time -DSSE2 -DOVERRIDE -DMPP -
DAUTODOUBLE -DNEWIO -DHAVE_BLAS_LAPACK -DHAVE_I8R8_LIBRARY -DMF3_SYM -
DNEW_UNITS -DEXTENDED -DBATTERY -DDUALCESE -DUSE_R123 -DLSTCODE -DBIGID -
DENABLE_HASH3 -DFFTW -DROTORDYN -DMUMPS -DLSGPART -DMF3_SYM -DMCMS -DUSES_CXX -
DPFEM -DMUMPSVER=stable -DUSES_CPP  -DPTHREADS -i8 -r8 -lpmpi -lrt -lstdc++ -
lpthread -lstdc++ -lpthread
#
LMATH=libscalapack.a liblapack.a libblas.a
#
OBJS=init_once.o init_dyn21.o dynm.o banner.o sec.o dyn21.o dyn21umat.o dyn21um
ats.o dyn21umatv.o dyn21umatc.o dyn21tumat.o dyn21utan.o dyn21ueos.o dyn21cnt.o
 dyn21ushl.o dyn21usld.o  couple2other_user.o dynrfn_user.o adummy_graph.o orde
rByMetis.o mod_impl_matrices.o
#
LIBS=libdyna.a liblsmpp.a libmpp_lanczos.a libbcsext4.a liblsda.a liblsdb.a lib
lssecurity.a liblcpack.a libspooles.a libcparse.a libmf2.a liblsm.a liblscrypt.
a libresurf.a liblsmppdes.a libdsa.a libbalance.a libsfg.a libzmumps.a libdmump
s.a libmumps_common.a libmetis.a libim_rotor_dynamics.a libmcms.a liblsmpp.a li
blso.a libunits.a libem.a libfemster_wrap.a libfemster_wrap2d.a libfemster_wrap
1d.a libfemster.a libfemster2d.a libfemster1d.a libpfem.a libcese.a libchemistr
y.a libparticles.a libeosfl2.a libpfem.a libmoving.a libdualcese.a libbattery.a
 liblsmpp.a libmetis.a libfftw3.a libansysl.a libdyna.a libmetis.a libspooles.a
#
LIBS_LOCAL=${MKLROOT}/lib/intel64_lin/libmkl_blas95_ilp64.a ${MKLROOT}/lib/inte
l64_lin/libmkl_lapack95_ilp64.a ${MKLROOT}/lib/intel64_lin/libmkl_scalapack_ilp
64.a -Wl,--start- group ${MKLROOT}/lib/intel64_lin/libmkl_intel_ilp64.a
${MKLROOT}/lib/intel64_lin/libmkl_sequential.a ${MKLROOT}/lib/intel64_lin/libmk
l_core.a ${MKLROOT}/lib/intel64_lin/libmkl_blacs_openmpi_ilp64.a -Wl,--end-
group -lpthread -lm -ldl
#
mppdyna: $(OBJS)
   set PATH=.:$(PATH)
   $(LD) -o mppdyna $(OBJS) $(LIBS) $(LMATH) $(LF) $(LIBS_LOCAL)
```

```
#
init_dyn21.o: init_dyn21.f nhisparm.inc
   $(FC) -c $(FF) -I. init_dyn21.f
userinterface.o: userinterface.f90
   $(FC) -c $(FF) -I. userinterface.f90
dyn21.o: dyn21.f nhisparm.inc userinterface.o
   $(FC) -c $(FF) -I. dyn21.f
dyn21umat.o: dyn21umat.f nhisparm.inc userinterface.o
   $(FC) -c $(FF) -I. dyn21umat.f
dyn21umats.o: dyn21umats.f nhisparm.inc userinterface.o
   $(FC) -c $(FF) -I. dyn21umats.f
dyn21umatv.o: dyn21umatv.f nhisparm.inc userinterface.o
   $(FC) -c $(FF) -I. dyn21umatv.f
dyn21umatc.o: dyn21umatc.f nhisparm.inc userinterface.o
   $(FC) -c $(FF) -I. dyn21umatc.f
dyn21tumat.o: dyn21tumat.f nhisparm.inc userinterface.o
   $(FC) -c $(FF) -I. dyn21tumat.f
dyn21utan.o: dyn21utan.f nhisparm.inc userinterface.o
   $(FC) -c $(FF) -I. dyn21utan.f
dyn21ueos.o: dyn21ueos.f nhisparm.inc userinterface.o
   $(FC) -c $(FF) -I. dyn21ueos.f
dyn21cnt.o: dyn21cnt.f nhisparm.inc userinterface.o
   $(FC) -c $(FF) -I. dyn21cnt.f
dyn21ushl.o: dyn21ushl.f nhisparm.inc userinterface.o
   $(FC) -c $(FF) -I. dyn21ushl.f
dyn21usld.o: dyn21usld.f nhisparm.inc userinterface.o
   $(FC) -c $(FF) -I. dyn21usld.f
couple2other_user.o: couple2other_user.f
   $(FC) -c $(FF) -I. couple2other_user.f
dynrfn_user.o: dynrfn_user.f
   $(FC) -c $(FF) -I. dynrfn_user.f
```

A.3 Compiling the UMAT

In the same working directory as the UMAT, use the following command to load the regular MPP LS-Dyna program and intel compliers.

```
module load mpp-dyna/12.0.0 intel/2020
```

The corresponding requirement modules will be automatically loaded at the same time:

```
Loading mpp-dyna/12.0.0
  Loading requirement: intel-rtl/2020 openmpi/4.0.3-intel
```

Then use the `make` command to compile the UMAT and create a new LS-Dyna executable file that contains the user-defined material subroutine. The following message indicates that the UMAT has been successfully complied and linked to LS-Dyna.

```
mpif90 -c -safe_cray_ptr -assume byterecl,buffered_io,protect_parens -
warn nousage -zero -ftz -fp-model precise -mP2OPT_hpo_dist_factor=21 -diag-
disable 10212,10010 -fimf-arch-consistency=true -qno-opt-dynamic-align -xSSE2 -
align array16byte -traceback -pad -DLINUX -DIFORT -DNET_SECURITY -DADDR64 -
DINTEL -DXEON64 -DFCC80 -DTIMER=cycle_time -DSSE2 -DOVERRIDE -DMPP  -
DAUTODOUBLE -DNEWIO -DHAVE_BLAS_LAPACK -DHAVE_I8R8_LIBRARY -DMF3_SYM -
DNEW_UNITS -DEXTENDED -DBATTERY -DDUALCESE -DUSE_R123 -DLSTCODE  -DBIGID -
DENABLE_HASH3 -DFFTW -DROTORDYN -DMUMPS -DLSGPART -DMF3_SYM  -DMCMS -
DUSES_CXX -DPFEM -DMUMPSVER=stable -DUSES_CPP  -DPTHREADS -i8 -r8 -fPIC -O2 -
I. dyn21umats.f …
```

The new LS-Dyna executable file, named `mppdyna` is generated along with a new object file named `dyn21umats.o` and is ready for running simulations.